SCUOLA DI DOTTORATO
UNIVERSITÀ DEGLI STUDI DI MILANO-BICOCCA

Dipartimento di / Department of

Materials Science

Dottorato di Ricerca in / PhD program Materials Science and Nanotechnology Ciclo / Cycle XXXII

Curriculum in (se presente / if it is) Nanosciences - 79R - 3

Functionalized Concave Cube Gold Nanoparticles as Dual probe for Magnetic Resonance Imaging and Surface Enhanced Raman Scattering

Cognome / Surname Fatehbasharzad Nome / Name Parisa

Matricola / Registration number 823754

Tutore / Tutor: Dr. Miriam Colombo

Cotutore / Co-tutor: Dr. Daniela Delli Castelli

(se presente / if there is one)

Coordinatore / Coordinator: Prof. Marco Bernasconi

ANNO ACCADEMICO / ACADEMIC YEAR 2018-2019

Table of Contents

List of Figures and Tables 4

List of Abbreviation 6

List of Symbols 9

Abstract 11

Chapter 1 Introduction 14

1.1 Cancer 15

1.2 Magnetic Resonance Imaging 16

1.3 Contrast Agent 18

1.4 Gadolinium 20

1.5 Raman Spectroscopy 27

1.6 Surface-Enhanced Raman Spectroscopy(SERS) 27

1.7 Enhancement Factor 31

1.8 SERS Tag 33

1.9 The Main Components of a SERS Tag 35

1.9.1 Nanoparticle 35

1.9.2 Raman Reporter 36

1.10 Direct vs. Indirect Detection 38

1.11 Nanoparticles 39

1.12 Gold Nanoparticles 42

1.13 Size of Nanoparticles 43

1.14 Shape of Nanoparticles 44

1.15 Concave Cube Gold Nanoparticles 54
1.16 Functionalization (Coating) 56
1.16.1 Polyethylene glycol (PEG) 58
1.17 Tumor Targeting 59
1.17.1 Trastuzumab 62
1.17.2 Biotin 63
1.18 Toxicity 64
1.18.1 MTT 65
Chapter 2 68
2.1 Materials and Instruments: 69
2.2 Synthesis of Gadolinium Complex 69
2.2.1 Characterization of Gadolinium Complex 72
2.3 Synthesis of Concave Cube Gold Nanoparticles 75
2.4 Functionalization of Concave Cube Gold Nanoparticles 78
2.5 Synthesis of Spherical Gold Nanoparticles 82
2.5.1 Characterization of Nanoparticles 83
Chapter 3 95
3.1 Aim 96
3.2 Instruments and Methods 96
3.2.1 ^{17}O NMR Measurements 97
3.2.2 Cytotoxicity assays 97
3.3 Result 99
3.3.1 Determination of water exchange rate 99

3.3.2 NMRD Profiles of free Gadolinium complex 100
3.3.3 NMRD Analysis of PEG_Gd@CCGNPs and PEG-Gd@SphNPs 103
3.3.4 Cytotoxicity assays of nanoparticles 105
3.4 Discussion 106
3.4.1 Relaxometric Characterization of the Gd Complexes 106
3.5 Conclusion 110
Chapter 4 112
4.1 Aim: 113
4.2 Instruments and Methods: 113
4.2.1 Culturing cells for Raman experiment 114
4.2.2 Raman imaging 115
4.3 Result 115
4.3.1 Assessment of Raman activity of concave cube gold nanoparticles 115
4.3.2 *In Vitro* experiment 117
4.4 Discussion 119
4.5 Conclusion 119
Expected achievement 121
Bibliography 122

List of Figures and Tables

FIGURE 1 PLACING A PATIENT IN A MAGNETIC FIELD (B_0) POLARIZES THE PATIENT AND CAUSES EACH PROTON DIPOLE TO PRESSES RANDOMLY. 18

FIGURE 2 PICTORIAL DESCRIPTION OF THE PARAMETERS THAT INFLUENCE THE RELAXIVITY OF A MRI CONTRAST AGENT 25

FIGURE 3 SCHEMATIC REPRESENTATION OF THE RAMAN MICROSCOPE 27

FIGURE 4 MODEL OF A TWIN PLANE IN A FACE-CENTERED CUBIC METAL. 46

FIGURE 5 (A) MODELS OF THE LOW-INDEX SURFACE FACETS OF FCC METALS, SUCH AS AU. (B) MODELS (LEFT) AND SCANNING ELECTRON MICROSCOPY (SEM) IMAGES (RIGHT) OF REPRESENTATIVE POLYHEDRAL NANOPARTICLE SHAPES BOUND BY EACH OF THE LOW-INDEX FACETS 47

FIGURE 6 IN A SEED-MEDIATED SYNTHESIS OF GOLD NANOPARTICLES 53

FIGURE 7 BRUSH AND MUSHROOM CONFIGURATIONS FOR POLYETHYLENE GLYCOL MOLECULES ATTACHED ON THE GOLD SURFACE. 59

FIGURE 8 A. PASSIVE TARGETING OF NANOCARRIERS. B. ACTIVE TARGETING STRATEGIES. 62

FIGURE 9 CHEMICAL SYNTHESIS OF GD (III) COMPLEX 6. 72

FIGURE 10 CHROMATOGRAM UPLC-UV OF COMPOUND 4. 73

FIGURE 11 ESI (+) MASS SPECTRUM OF PEAK AT 3.77 MIN (COMPOUND 4). 73

FIGURE 12 ESI (+) MASS SPECTRUM OF COMPOUND 5. 74

FIGURE 13 ESI-MASS SPECTRUM OF GD(III) COMPLEX 6. 74

FIGURE 14 UPLC CHROMATOGRAM OF GD (III) COMPLEX 6. 75

FIGURE 15 PREPARATION OF PEG-GD/MGITC @CCGNPS 79

FIGURE 16 SCHEMATIC REACTION OF LABALLING THE ANTIBODIES 81

FIGURE 17 SCHEMATIC REACTION OF 1) INTERNAL MANNOSE OXIDATION 2) CONJUGATION BETWEEN NANOPARTICLES AND ANTIBODY.....81
FIGURE 18 TEM IMAGES OF CONCAVE CUBE GOLD NANOPARTICLES.....84
FIGURE 19 SEM IMAGES OF SPHERICAL GOLD NANOPARTICLES 85
FIGURE 20 PARTICLES SIZE DISTRIBUTION FOR CONCAVE CUBE GOLD NANOPARTICLES BEFORE AND AFTER AU GROWING LAYER 87
FIGURE 21 PARTICLES SIZE DISTRIBUTION (BACKWARD) FOR CONCAVE CUBE GOLD NANOPARTICLES BEFORE AND AFTER PEGYLATION.....87
FIGURE 22 PARTICLES SIZE DISTRIBUTION (FORWARD) FOR CONCAVE CUBE GOLD NANOPARTICLES AFTER PEGYLATION. 88
FIGURE 23 PARTICLES SIZE DISTRIBUTION OF SPHGNPS BEFORE AND AFTER PEGYLATION ..88
FIGURE 24 DIAGRAM SHOWING THE IONIC CONCENTRATION AND POTENTIAL DIFFERENCE AS A FUNCTION OF DISTANCE FROM THE CHARGED SURFACE OF A PARTICLE SUSPENDED IN A DISPERSION MEDIUM.....89
FIGURE 25 ZETA POTENTIAL OF THE 1) CONCAVE CUBE 2)SPHERICAL GOLD NANOPARTICLES BEFORE AND AFTER PEGYLATION......90
FIGURE 26 UV-VIS SPECTRA OF CONCAVE CUBE GOLD NANOPARTICLES BEFORE AND AFTER AU GROWING LAYER. 90
FIGURE 27 UV-VIS SPECTRA OF 46-NM SPHERICAL NANOPARTICLES.....91
FIGURE 28 REPRESENTATIVE GRAPHS OF NANOSIGHT™ PARTICLE TRACKING ANALYSIS OF CONCAVE CUBE GOLD NANOPARTICLES. 93
FIGURE 29 REPRESENTATIVE GRAPHS OF NANOSIGHT™ PARTICLE TRACKING ANALYSIS OF SPHERICAL GOLD NANOPARTICLES. 93
FIGURE 30 ^{17}O NMR MEASUREMENT OF THE GD COMPLEX 6. 100
FIGURE 31 NMRD PROFILE OF GADOLINIUM COMPLEX 6 AT 25˚C AND 37˚C.....102

FIGURE 32 NMRD PROFILE OF CONCAVE CUBE AND SPHERICAL GOLD NANOPARTICLES AT 25 °C AND 37°C. 104
FIGURE 33 MOLAR RELAXIVITY OF GD COMPLEX, PEG-GD@SPHNPS AND PEG-GD@CCGNPS. 105
FIGURE 34 MTT ASSAY RESULTS FOR SHORT INCUBATION TIME (3H). 106
FIGURE 35 SCHEMATIZATION OF A PARAMAGNETIC COMPLEX WITH ONE INNERSPHERE MOLECULE, ONE SECOND-SPHERE MOLECULE AND SEVERAL OUTERSPHERE WATER MOLECULES. 108
FIGURE 36 NANO-OBJECTS WITH VARYING CURVATURES. 110
FIGURE 37 (1) UV-VIS SPECTRA AND (2) RAMAN SPECTRA OF SERS CONCAVE CUBE GOLD NANOPARTICLES. 117
FIGURE 38 INTERNALIZATION OF CCGNPS IN D2F2/E2 CELLS 118

TABLE 1 ULTRA PERFORMANCE LIQUID CHROMATOGRAPHY (UPLC) CONDITIONS OF GD (III) COMPLEX 6 WITH ELUENTS: A:WATER+0.05% TFA, B:ACN+0.05% TFA 75
TABLE 2 NMRD BEST FIT PARAMETERS GD COMPLEX 6 AT 298K AND 310K. 104
TABLE 3 NMRD BEST FIT PARAMETERS FOR PEG-GD@CCGNPS AND PEG-GD@SPHNPS AT 25˚C AND 37˚C. 105

List of Abbreviations

AA Ascorbic acid

Ab Antibody

AuNRs Gold nanorods

CA Contrast agent

CARS Coherent anti-stokes scattering

CCGNPs Concave cube gold nanoparticles

CE Chemical enhancement

CT Computed tomography

CTAB Cetrimonium bromide

CTAC Cetrimonium chloride

CV Cyclic voltammetry

DIPEA N,N-Diisopropylethylamine

DLS Dynamic light scattering

DNA Deoxyribonucleic acid

DOTA dodecane tetraacetic acid

DTPA diethylenetriaminepentaacetic acid

EDTA Ethylenediaminetetraacetic acid

EF Enhancement factor

EGFR Epidermal growth factor receptor

EM Electromagnetic

EMEM Eagle's Minimum Essential Medium

EPR Enhanced permeability and retention

FBS Fetal bovine serum

FCC Face-centered cubic

HBTU Hexafluorophosphate Benzotriazole Tetramethyl Uronium

HEPES (4-(2-hydroxyethyl)-1-piperazineethanesulfonic acid)

HER2 Human epidermal growth factor receptor 2

HOBt.H_2O 1-Hydroxybenzotriazole hydrate

ICPMS Inductively coupled plasma mass spectrometry

LSPR localized surface plasmon resonance

MGITC Malachite green iso thiocyanate

MRI Magnetic resonance imaging

MTS 3-(4,5-dimethylthiazol-2-yl)-5-(3-carboxymethoxyphenyl)-2-(4-sulfophenyl)-2H-tetrazolium

MTT 3-(4,5-cimethylthiazol-2-yl)-2,5-diphenyl tetrazolium bromide

NIBS incorporating non-invasive backscatter

NIR Near infrared

NMR Nuclear magnetic resonance

NMRD Nuclear Magnetic Relaxation Dispersion

NTA Nanoparticle tracking analysis

OD Optical density

PBS Phosphate-buffered saline

PCS Photon correlation spectroscopy

PEG Polyethylene glycol

PET Positron emission tomography

QDs Quantum dots

RES Reticuloendothelial system

RF Radio frequency

RRS resonance Raman scattering

SALDI-TOF MS Surface Assisted Laser Desorption-Time of Flight Mass Spectroscopy

SATA N-succinimidyl S-acetylthioacetate

SBB Sodium borate buffer

SBM Solomon Bloembergen Morgan

ScVF single-chain variable fragment

SdAbs Single-domain antibodies

SERS Surface-enhanced Raman spectroscopy

SPECT Single-photon emission computed tomography

SPhNPs Spherical nanoparticles

spSERS single-particle Surface-enhanced Raman spectroscopy

SRS stimulated Raman scattering

TERS Tip-enhanced raman scattering

TEM Transmission electron microscopy

TFA Trifluoroacetic acid

TFP Tetrafluorophenyl

THH Tetrahexahedral

TIS Triisopropyl silane

UPD Underpotential deposition

UPLC Ultra performance liquid chromatography

List of symbols

Abs_{cot} Absorbance of control untreated cells

Abs_T Absorbance of treated cells

B_0 magnetic fied

C Molar concentration of a paramagnetic compound

C_{SERS} /C_{NR} Raman scattere concentration in the SERS and normal raman spectra

$E_{out}(\lambda)$ / $E_{out'}(\lambda)$ Quantities of the field enhancement at the NP surface for the incident and Raman-shift wavelengths

I_{sers} / I_{NR} Inthensities of the SERS and normal Raman spectra

K_{ex} Water exchange kinetics

n Number of repetition in the polymer chain

n_1 Larmor frequency

pK_a Acidity constant

q Number of bound water molecules

r_1/r_2 relaxation rate local values of water protons

r_{1p}/r_{2p} Paramagnetic relaxation rate of free water protons

R_F Flory radius

r_{MH} metal-water hydrogen distance

S Spin quantum number

T_1/T_2 relaxation time local values of water protons

T_{1e}/T_{2e} Electronic relaxation times

T_{1m}/T_{2m} the longitudinal relaxation time for the bound water proton

T_{2r} Relaxation time for the paramagnetic transverse ^{17}O

α Unit length of the monomer

τ_c Overal correlation time

τ_m Average residence time in the coordination sites

τ_r Rotational correlation time

Abstract

An innovative class of MRI CAs is represented by Gd-loaded gold nanoparticles. Differently from other nano-sized systems, the size, shape and chemical functionalization appear to affect the observed relaxation enhancement of water protons in their suspensions. The herein reported results shed more light on the determinants of the relaxation enhancement brought by Gd-loaded concave cube gold nanoparticles. It has been found that the role of the concave surface of these nanoparticles in the relaxivity is remarkable and it provides high contribution of second sphere water molecules. The specific shape of concave cube nanoparticles increases the relaxivity from 20.9 $mM^{-1}S^{-1}$ for spherical nanoparticles to 34 $mM^{-1}S^{-1}$.

On the other hand, our studies prove that this special shape gold nanoparticles show high efficiency as a SERS probe. In the single-particle surface-enhanced Raman spectroscopy, the use of tunable plasmonic nanoparticles, having tipped surface structures, as being substrates revealed a highly feasible and promising approach to optimize SERS-based imaging and sensing applications. The concave cubic morphology has shown a remarkable plasmonic response, representing high sensitivity to the concavity degree. hence they can provide strong Raman signal which can be use in Raman imaging.

Magnetic resonance and optical imaging are complementary techniques. By applying same nanoparticles as a contrast agent for both methods simultaniusly, screening total body with very clear identification become possible. This progress in imaging technologies associated with the advance of nanotechnology makes feasible the cancer detection and localization in its early stage.

Chapter 1

Introduction

1.1 Cancer

Cancer had been recognized as the second deadliest disease throughout the world by the end of the last centennial. Based on the reports, about 7.4 million deaths occurred by cancer in 2004, with the most abundance in developing countries. This would approach 12 million deaths by 2030 as estimated. Earlier detection of cancer could survive 30% of people who died of cancer (World Health Organization, www.who.int/, 2010). So, early diagnosis and therapy of cancer increase the probability of being cured. However, difficult diagnosis and treatment of cancer would be due to its growth generally from the midst of organs which cannot be identified by the immune system as a foreign body. Cancer is defined as the uncontrollable cell division and spread of abnormal cells which often invade surrounding tissues bringing any body parts into effect through metastases [1]. The positive outcomes of early diagnosis through different types of treatment provide many motivating factors to develop technologies for cancer diagnosis at the earliest stages. Most often, early-stage cancer detection is associated with a 5-year relative survival rate of more than 90%, due to the availability of curative treatment. There are various medical tests currently used to detect cancer, including blood and urine tests, or imaging techniques with biopsy. Cancer detection is typically possible through conventional anatomic imaging techniques for dimensions of about few millimeters (e.g., MRI) or centimeters (e.g., PET), which may already contain more than one million cells. Newly emerged molecular imaging rectifies this disadvantage purposefully. The progress in imaging technologies associated with the advance of nanotechnology and molecular and cell biology make this new imaging modality possible to be developed. As molecular imaging can be applied to a variety of imaging techniques such as computed tomography, Positron Emission Tomography, or ultrasound. The magnetic resonance imaging (MRI) is of particular interest because of providing the best spatial resolution in comparison with other techniques. In this regard,

some innovative diagnosis and therapy manners are enabled through unique capabilities provided by nanotechnology coupled with other fields, like molecular biology and imaging technology [2].

1.2 Magnetic Resonance Imaging

In vivo visualization of gene expression, biomarkers, and biochemical processes applied technique can cause the improvement of molecular imaging. The widely-adopted magnetic resonance imaging is an essential imaging modality in clinics having some advantages, including capacity of producing excellent quality, images with high spatial resolution, and accurate anatomical information with soft tissue contrast [3]. As well, this kind of imaging allows long term longitudinal studies by acquiring the images with no radiotracer (PET and SPECT) or lack of using ionizing radiation (CT and X-ray). Hence, small cell populations can be efficiently tracked because of spatial resolution which is increased by stronger magnetic fields [4]. Radio communication has been developed within the last 19^{th} century by engineers and physicists. Radio emission is created as a result of electron oscillation in the conductor, which requires a type of construction for the electronic circuit, namely oscillator. The oscillator is the basis for radio electronics which produces electromagnetic radiation as the radiofrequency emission. This radiation can be identified according to the oscillation frequency by physicists. It is also impressive to use the RF region in the electromagnetic spectrum for imaging that can be carried out through an analytical procedure known as nuclear magnetic resonance. Visible images of a body are produced by the reflection of radiation. However, stimulation is needed for MR images supposing the emission of electromagnetic radiation from the body. Finally, an image is produced by detecting, interpreting and using the emitted signal. The human body comprises of almost 80% hydrogen atoms. The hydrogen nuclei pointed out as the

proton, in the body of patients behaves similarly to tiny bar magnet making this atom acutely useful for MRI. Single-charged hydrogen has a spinning nucleon with the magnetic moment and angular momentum exhibits magnetism. The magnetic moment of the nuclei is randomly oriented before exposing the patient to the B_0 magnetic field. This cause the net magnetic field of a patient to be zero as a consequence of cancelation of all individual magnetic dipole moments. North and south magnetic poles can be created in a patient when is exposed to a strong external magnetic field through the alignment of several individual nuclear magnetic moments with the external magnetic field. In the MRI experiment, a pulsed RF energy is emitted to the patient from an RF coil, as an inductor at the Larmor frequency (Fig. 1). Now, magnetizing the field in the Z direction (parallel to the direction of B_0) makes magnetic dipoles of the proton to be aligned and each individual proton proceeds at the Larmor frequency. The resonating pulsed RF signal can change the energy state of the most protons in the patient. In this case, all protons “flip” toward the negative Z-direction after net magnetization and they still precess around the Z-axis. In the presence of pulsed RF, protons continue to precess in addition to filp individually and transfer their energy to a patient. The normal state of the net magnetization is then achieved gradually in the positive Z direction. In the normal state, there is an equilibrium between protons in the B_0 magnetic field, which can be regarded as the equilibrium magnetization state. Returning individual protons to equilibrium makes the net magnetization to precess around the Z-axis, as well as to return (relax) back slowly toward equilibrium. During the experiment, the patient is surrounded by the RF coil which receives an oscillating signal. Dephasing the proton spins, i.e. losing phase coherence, may decrease this signal with the time. There are two time constants in MRI, known as the relaxation time so that T_2 relaxation time which is specifically named the transverse relaxation time and describe mentioned process and T_1 represents the magnetization rate

back to equilibrium. The spin system energy decreases by growing the longitudinal component toward B_0 direction. Since most spins favor the orientation with lower energy statistically (to be parallel and spined-up), the energy should be released from the spin system for T_1 relaxation. Thus, this unrecoverable energy loss, represents the heat transfer, suggesting the term "thermal relaxation" for the T_1. This released energy is ideally transferred into nearby nuclei, atoms and molecules through electromagnetic interactions, rotations or collisions. Simply put, T_1 relaxation time is a spin-environment energy flow. The nuclei energy transfer is very small in amount as compared with normal molecular kinetic energies, that can quickly disappear in the temperature of a body. Initial solid-state NMR studies represented the external environment by a crystalline lattice of atoms that points the term "spin-lattice relaxation" as another synonym for T_1. Generally, T_1 and T_2 can be regarded to be independent of one another as representing two different processes taken place at the same time but often at different rates [5-7].

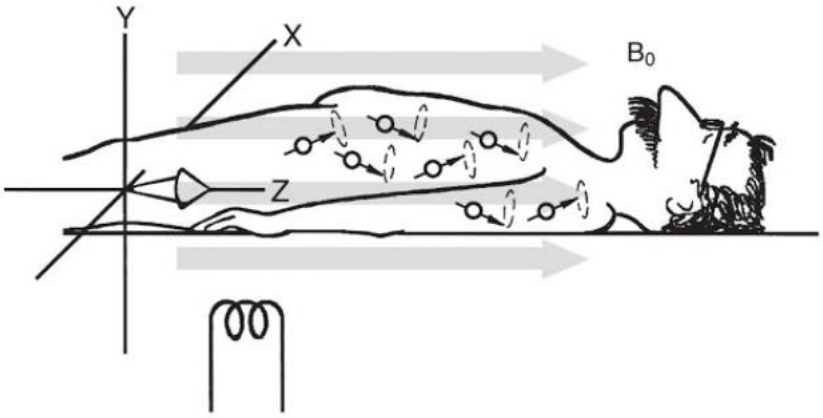

Figure 1 placing a patient in a magnetic field (B_0) polarizes the patient and causes each proton dipole to presses randomly [6].

1.3 Contrast Agent

In magnetic resonance images the contrast is made by varied water contents in living bodies that have caused diverse relaxivity rates of water protons in the presence of a magnetic field. Most tissues are then illustrated and identified as a result of

heterogeneous water distribution in organisms [7]. Sometimes a remarkable contrast can not be detected in MR images using T_1/T_2 relaxation time; because there is no significant difference in these times value for biological tissues, or between pathologic and normal tissues. Pathological tissues can be differentiated from normal surrounding tissues just in cases with adequate contrast. Moreover, different T_1/T_2 relaxation times for two tissues can enhance the contrast between them [8]. Magnetically similar cells and tissues with histological distinction can be differentiated visually by utilization of MRI contrast agents [4]. Contrast agents are used in order to increase the sensitivity of MRI wherein there is insufficient MR contrast, providing positive or negative image contrast. In 1988, the first MR contrast agent (CA) was introduced for imaging abnormalities in a blood-brain barrier. Thereafter, diagnostic medicine has significantly developed using contrast-enhanced of MRI. These agents have effect on bulk water molecules that cause them detectable indirectly. A paramagnetic complex or particle is able to generate a fluctuating magnetic field considering Brownian motion to induct relaxation in the surrounding water molecules. The relaxation effect is transmitted to the bulk through a fast exchange (>106 s^{-1}) of the water interacting with the metal ion and the bulk. Chemical properties of a contrast agents influence the magnitude of the stated effect strongly that can be potentially modulated to produce a stronger signal in certain environments. Selective reduction of T_1 (and T_2) relaxation times of water in tissues is the basic mechanism of MR contrast agents to act through interaction between electron spins of the metal-containing contrast agent and water protons in tissues [8,9]. The type of imaging is chosen regarding the ratio between r_2 and r_1 whether to use a contrast agent for T_1-weighted imaging or for contrast-enhanced T_2- and T_2-weighted imaging. T_1 agents have lower r_2 to r_1 ratios (with the amounts of between 1.1 and 2) which generate positive contrast (in the form of bright/hot spots in T_1-weighted MRI), whilst T_2 agents with larger r_2 generate negative contrast (in the form of

dark/cold spots in T_2- and T_2-weighted MRI) [10]. T_2 contrast agents have various disadvantages that can cause limitation of their application in clinical fields. Reduction of MRI signals is one of disutilities making it illusory. These agents may disturb accurate tumor imaging by inducing perturbations in the magnetic field on the neighboring protons in normal tissue. High relaxivity rate of iron oxide particles, i.e. magnetite/maghemite, makes single-cell tracking easier; But *in vivo* cell distribution of the brain, the definitive interpreted is more complicated for T_2-weighted magnetic resonance images; due to the potential blooming artifacts caused by slight hemorrhage and air bubbles, as well as potential nanotoxicity for neurons. T_1 contrast agents oppositely increase the sensitivity and specificity of the MR image. Mn(II) and Gd(III), as a T_1 agents are able to produce an unequivocal signal. Substitution of Mn(II) agents with Ca^{2+} ions in the cell, makes them easier to take-up and provide T_1 disclosure of specifically labeled cells. But, this unchelated manganese exerting cytotoxic effects [11,12]. Gd-CAs are a proper alternative e.g. for superparamagnetic iron oxide nanoparticles with extra advantages of easier functionalization as well as better control over a molecular size [13]. The scanning of the tumor vascularity and perfusion can be achieve by following of contrast agent first when it passes through the arteries or then dynamically monitoring accumulation and clearance from the tumor [9].

1.4 Gadolinium

Engineered contrast agents are suitable to investigate biologically significant events, including enzyme activity, ion fluctuation, temperature variation, and peroxide evolution, which are fabricated in a wide variety of bioactivatable materials through recently advanced strategies in the design and amplification method [4]. In 1987, a review has examined paramagnetic metal complexes to be used in NMR imaging which motivate the

coordination chemist for the sake of developing novel gadolinium complexes used as a contrast agent in MR imaging. At the moment, the number of the researchers who are interested in using contrast agents increasing daily [14]. The amount of using gadolinium(III)-based contrast agents in all magnetic resonance imaging and neuro MRI exams are about 40% and 60%, respectively which shows near 40 million GBCAs administrations all over the world [9].

T_1 relaxation is induced paramagnetically which depends directly on the spin quantum number [as a function of S (S +1)]. Paramagnetic complexes of gadolinium [Gd(III)] are excessively used as contrast agents. They reduce the longitudinal relaxation time (T_1) for local water protons because of high symmetric *S*-state and magnetic moment of Gd(III). This feature provides this agent with a fairly lagging electronic relaxation rate as being necessary for promoting gadolinium seven unpaired electrons in the inner 4f orbitals and to further strong nuclear relaxation. The presence of Gd(III) demonstrates more intensified signals and bright sections in T_1-weighted images [4].

In the application of GBCAs an essential factor is the kinetic and thermodynamic stability of a chelated Gd(III) complex, and if Gd(III) is contained within the chelate, the cytotoxicity can be deferred or even avoided. Thermodynamically stable macrocyclic ligands based on 1,4,7,10-tetraazacyclododecane- 1,4,7,10-teraacetic acid (DOTA) are similar to diethylene triamine (DTPA) based ligands that are linear. But macrocyclic ligands are more kinetically stable and thus, more desirable for chelating Gd(III)-based contrast agents [12]. GdDTPA and GdDOTA are extracellular agents as the first generation contrast agents used for clinical purposes currently. These so-called perfusion agents are distributed throughout interstitial spaces and plasma non-specifically which are rapidly excreted via the kidneys, or the liver, albeit in contrast agents with more lipophilic

hepatobiliary. Their next generation is also geared towards directed functional imaging or more specific exams [14].

The longitudinal relaxation rate of local water proton is the most prominent factor in to arise the intensity of MRI signals.

The effect of longitudinal relaxation rate on the intensity of MRI signals is confirmed so that the intensity is largely associated with relaxation local values of water protons.

$r_1=1/T_1$ (s^{-1}) (1)

Generally, the relaxation times for the water in the body are so that $T_2$is 5−20 times shorter than T_1. It can be concluded that the Gd(III) contrast agent will make a conspicuous effect on T_1 [9]. The relaxivity (r_1) is a measure of efficacy for a contrast agent, i.e. when the more total paramagnetic relaxation rate of free water protons (r_{1p}) per unit concentration of the paramagnet ($mM^{-1}\cdot s^{-1}$) is present, the contrast will be incremented. [Equation (2)]. Smarter, better, and more effectual contrast agents are regarded to those materials which can image lower concentration of targets and/or by lower dosages of contrast agent [14]. The relaxivity enhancement of water protons in the aqueous solutions of paramagnetic complexes arises from time fluctuation of the dipolar coupling between the electron magnetic moment of the metal ion and the nuclear magnetic moment of the solvent nuclei. A chemical point of view considers three contributions to relaxivity:(1) Inner-sphere relaxation: the water is in direct bond with the metal can relax and transmit the relaxation effect to the bulk water by being exchanged with another water molecule. (2) Second-sphere relaxation: the relaxation and exchange are promoted in the second coordination sphere with hydrogen-bonded water molecules or exchangeable hydrogen atoms (such as O−H and N−H bonds). (3) Outer-sphere relaxation: diffused water molecules approach the paramagnetic compound to promote relaxation. In the experiment, second-sphere and outer-sphere water molecules are complicate to distinguish; so these two groups are

often referred to as outer-sphere water molecules. Overall relaxivity can be factored into these two components of inner-sphere r_1^{IS} and outer-sphere r_1^{OS} relaxivity [Equation (3)]. The difference of the inner sphere and the outer sphere mechanisms comprises the interaction of gadolinium with directly bound and closely second-sphere diffused water molecules, respectively.

$r_1=r_{1p}/[Gd]$ (2)

$r_{1p}=r_{1p}^{IS} + r_{1p}^{OS}$ (3)

Inner sphere

In the inner-sphere, relaxivity of water ligands depends on external parameters such as the temperature and strength of the applied magnetic field; as well as some effective internal molecular factors like total water molecules within the inner-coordination sphere, q; the water exchange kinetics, $k_{ex} = 1/\tau_m$, where τ_m stands for the average residence time of the ligand; the rotational correlation time representing as rotational dynamics of a molecule, τ_r; the electron spin of the complex, S; and T_{1e} and T_{2e} electronic relaxation times, sometimes referred to as τ_S (Fig.2) [9]. The exchange rate τ_m and the coordination number can enhance the relaxation rate and both determine the number of water molecules effectively coordinated with Gd(III). As well, τ_r is substantial because of an increase in r_1 due to the lower tumbling rates for macromolecules, as observed in an ordinary field strengths' range [10].

The larger contribution of inner-sphere relaxation can be greatly controlled by Equation (4), with parameters of the molar concentration of a paramagnetic compound, C; the number of bound water molecules; the longitudinal relaxation time for the bound water protons, T_{1m}; and τ_m. The more responsive contrast agent is obtained by modulating and fine-tuning these parameters.

$$r_{Ip}^{IS} = \frac{Cq \quad I}{55.6\, T_{IM}+\tau_m} \quad (4)$$

Rotational Correlation Time: The T_{1m} longitudinal relaxation time for the bound water can be controlled by the τ_r molecular reorientation time (i.e. the rotational correlation) within the range of magnetic field strengths common for MRI scans (0.5–1.5 T, or 20–60 MHz). At higher field strengths, making changes in this parameter would not be influential, while it may sometimes be deleterious to CA performance. The slower tumbling of the Gd(III) complex makes the longer correlation time which causes faster relaxation rates and thus, higher relaxivities. At entire field strengths above 0.1 T, the value of r_1 is limited for simple chelates by the fast rotation. The τ_r is then lengthened based on some approaches. The slow tumbling rate of the Gd(III) complex can be possible by attaching to slowly tumbling macromolecules, such as a protein, polysaccharide, and dendrimer, or by aggregating in amphiphilic complexes. A non-covalent interaction between a slowly tumbling macromolecule with the Gd(III) complex, as a host-guest approach, is a consequence likely to be most impressive [14,15].

Exchange Rate of the Water Molecule. The tunable water exchange rate k_{ex} is another key molecular parameter represented as $1/\tau_m$, where τ_m stands for the water residence time in the coordinated form. As suggested by Solomon-Bloembergen-Morgan (SBM) simulations , this strategy is likely to enhance r_1 significantly just for CAs having near-optimal τ_r values, especially at lower field strengths (e1.5 T). Nanoconjugate CAs intrinsically encompass slow tumbling rates pursuant to their size. Hence, optimization of τ_m in nanoconjugate systems where q is held constant causes r_1 to improve. Relaxivity generally depends on $1/(T_{1m} + \tau_m)$. Considering $T_{1m} \gg \tau_m$ for small Mn(II) and Gd(III) complexes represents no restriction by slow water exchanges for these complexes. The relaxivity may also be limited by the water exchange as rotation gets slowed and causes T_{1m} to decrease. The water exchange rate is also slow for other metal ions relative to T_{1m}. However, the τ_m can mainly influence once optimizing the rotational correlation time. The

τ_r value of nanoconjugate CAs often surpass tens of nanoseconds, so, overall correlation time (τ_c) is controlled by smaller values of T_{1e}, τ_m, or both if of similar length [15,9].

Electronic Relaxation. The correlation time is governed by electronic relaxation for Mn(II) and Gd(III) complexes once exposed to very low fields (<0.1 T). In these paramagnetic complexes, the relaxivity is influenced by the electronic relaxation mostly depending on decay of electron spin magnetization parallelly to the external magnetic field (T_{1e}).

Metal-Water Hydrogen Distance. This metal-proton distance affects the relaxation rate with the inverse sixth power, so, small r_{MH} changes would profoundly affect the relaxivity, particularly if it can be tunable. A direct bond between the water molecule and the metal ion and taking a coordination position, makes the shortest r_{MH} distance in the inner-coordination sphere [9].

The number of Water Molecules. The relaxivity of an inner-sphere system has been directly proportionated to the number of water molecules as the ligand [Equation (4)]. Although an increased amount of hydration (q) enhances the relaxivity of inner-sphere systems, it often leads to decreased kinetic inertness and/or thermodynamic stability [9].

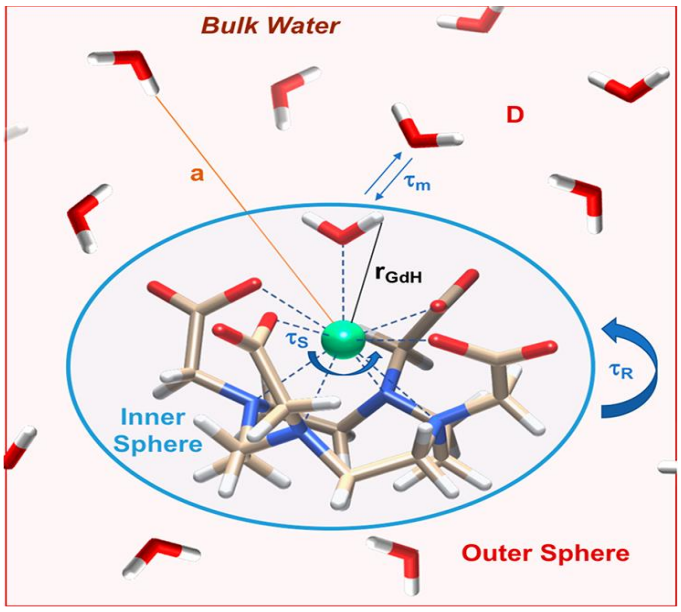

Figure 2 Pictorial description of the parameters that influence the relaxivity of a MRI contrast agent [9].

Outer-Sphere Relaxivity. Both inner-sphere and outer-sphere contribution to relaxivity, are required to be investigated. Regarding the hard-sphere model proposed by Hwang and Freed, the relaxivity deduced from the diffused water molecules close to the gadolinium(III) complex would be predicted; since the relaxation is primarily conditional to the water diffusion coefficient and the closest distance to the metallic center. Complexes with exchangeable protons or water molecules in the second coordination sphere with having longer residence time relative to the diffusion lifetime, are operationally considered by second-sphere relaxivity. Noteworthy, inner-sphere and second-sphere relaxivities are described with the same equations, but with a slight difference that the governing correlation time would be the residence time of protons in the second-sphere. The outer sphere relaxivity is significant in cases of unexpectedly high r_1 values for nanoconjugate systems or conditions that the observed relaxivity cannot be justified by independently determination of molecular parameters [14,15].

1.5 Raman Spectroscopy

Raman spectroscopy collects inelastic light scattering from interrogated samples and separates them spectrally for analysis. The chemical information and sample composition are then obtained by analyzing frequency shifts of the scattered radiation corresponding to differences in the energy of the molecular vibrational levels of the sample, and thus spectra(Fig.3)[16].

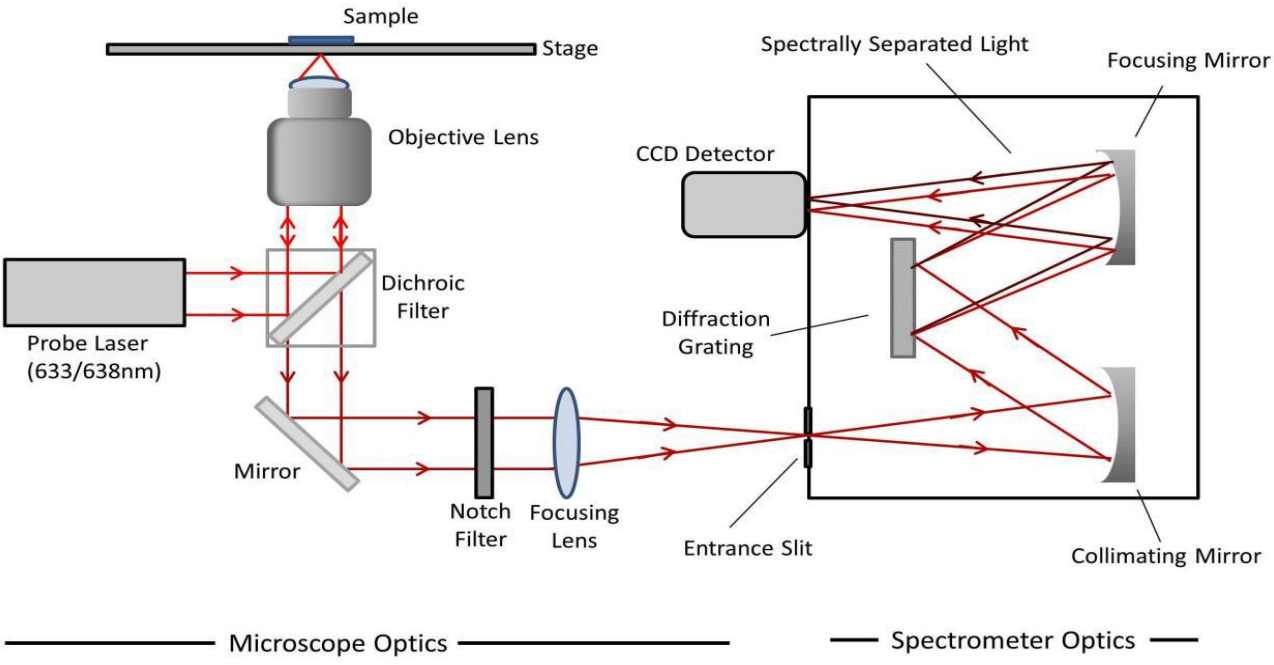

Figure 3 Schematic representation of the Raman microscope [16].

1.6 Surface-Enhanced Raman Spectroscopy(SERS)

The Raman scattering signal has an inherently very weak; Its intensity is approximately 1 in 106 incident photons, causing vibrational transition happened in the scatterer which results in either a Stokes or anti-Stokes Raman shifted photon. The Raman spectroscopy has been modified to cover this shortcoming by introducing several enhanced techniques including resonance Raman scattering (RRS), stimulated Raman scattering (SRS),

coherent anti-Stokes Raman scattering (CARS), and tip-enhanced Raman scattering (TERS). Surface-enhanced Raman scattering, the ultrasensitive vibrational spectroscopy, represents accurate structural information through dramatically molecular enhancement of Raman scattering. SERS is a potent noninvasive spectroscopic technique suitable to detect low abundance analytes, especially in cases of environmental monitoring, food safety inspection, and biomolecular sensing; As well as bioimaging. The advantageous surface-enhanced Raman spectroscopy is easily performed experimentally and has unexplored research areas in the SERS phenomenon, SERS signal quantitation and enhancement factor [16,17]. An essential resurgence of SERS in recent years is mainly stimulated by the developed detector and laser technology as well as by the discernment in “top-down” nanofabrication protocols and “bottom-up” synthetic methods. Several attempts have been devoted to comprehending the basis of the phenomenon by finding fundamental physical laws, as well as developing imaging approaches and sensing platforms. SERS has been of interest to researchers and in a short while, lots of primary works have revealed its usage for *in vivo* medical applications, particularly in the field of oncology. An improvement in the laser technology was one of the proofs so that using near-infrared (NIR) lasers for excitation would be associated with reduced tissue damage; while maximized depths of the light penetration. The concept of “SERS tag” has been introduced as an important factor in primary implementations of the SERS in medical fields. A SERS-active nanoparticle-based system, namely SERS tag, can easily penetrate or bind to cells, due to its size, and label them with bright SERS signals. The role of this system in Raman microscopy is conceptually similar to that of the fluorescent dye in fluorescence microscopy. In other words, diseased tissue can be indirectly identified using a SERS tag by examining the SERS signal of a Raman reporter bound to the tag. Accordingly, there is no need for relying on typical extremely weak

signals of biological tissues for identification. Further, carefully functionalized and synthesized SERS tags, when mixed in suspension, can enable the multiple targets detection simultaneously (i.e., multiplexing) with high selectivity and sensitivity. Very low intensities of the Raman signal is actually due to extremely small Raman cross-sections, about 14 orders of magnitude lower than their fluorescence counterparts [18]; but the Raman signal, exclusively obtained from molecules, can be amplified by several orders of magnitude through the SERS effects. The nanoscale effect SERS signal amplification, is mainly achieved via electromagnetic interaction of the light with metals which largely amplifies the laser field by means of excitations, commonly referred as plasmon resonances. This technique is advantageous for the molecules that are typically absorbed on the metal surface, or at least, are very close to that (typically≈10 nm maximum) [19]. The light scattering intensity amplification is due to the enhanced electromagnetic field near the surface of plasmonic noble metal nanoparticles, as a result of resonances in the visible region of the electromagnetic spectrum. The exploitation of this approach can be eligible for imaging purposes through Raman scattering of molecular species in proximity to the plasmonic surface or Rayleigh scattering of particles; whereby the wavelength shifts in the scattered radiation would form as a result of energy exchange between the incident light and vibrational energy levels of scattering species. The identity, conformation, and also surrounding environment of molecular scatterer(s) can be analyzed and determined by these shifts [16]. The simple electromagnetic model can translate the surface plasmonic excitation into a SERS mechanism. Based on the literature, even if a single isolated metal nanoparticle has not been credibly reported in the SERS approach, but a preliminary analysis of surrounding fields can determine some basic criteria required for intense SERS. The time-varying electric-field vector of the light induces various orders of oscillating multipole surface plasmon which can be sustained

by a small, isolated, illuminated metal sphere. The surface plasmons are defined by collective oscillations set on the conduction electrons adjacent to the ionic metal cores' background. The light can also induce the interband transitions by inducting a host of other excitations into the metal particle. The dipolar plasmon is just signified for a particle size much smaller than exciting light wavelength. Such excitation can be sustained in systems with free or almost free electrons, so that the freer electrons may cause the more intense and sharper dipolar plasmon resonance. The resonance of the exciting laser light with the dipolar plasmon makes the metal particle to radiate light with features of dipolar radiation. This would be a coherent process besides the exciting field which is characterized by the spatial distribution of field magnitudes (reaching the steady-state just a few femtoseconds after turning the light on) with enhanced light intensity on certain portions proximal the metal [20].

SERS would be effective in optical bioimaging technique, under optimal conditions, which enables high-resolution volumetric deep-imaging of biological tissues [21]. Nie et al. first introduced the molecular imaging guided by SERS tags. As an outcome, they confirmed that PEG-capped SERS tags functionalized with single-chain variable fragment (ScVF) antibody for EGFR have targeted and identified this protein in the human cancer cells as well as human tumor xenograft subcutaneously and in deep tissue [18]. The newly emerged “SERS tags” technology combines specific Raman reporter molecules and metallic nanoparticles to design novel nanoprobes. In a bioimaging viewpoint SERS is tempting tool due to: (i) major multiplexing ability; (ii) illustrious photostability; (iii) great spatial resolution; and (iv) lack of intervention by water. As a matter of choice, the bioimaging with a SERS probe must be conducted so that the SERS (i) provides strong, stable and uniform SERS signals coming from NIR excitation resulting in significantly lower absorption of the tissue in comparison with visible region of EM spectrum (optical

therapeutic window) (ii) is susceptible for facile biofunctionalization, and (iii) is bioinert or biocompatible [21,22].

SERS would be conceived as a complementary tool for some medical imaging techniques, like MRI; because SERS tags are not beneficial to all medical procedures. This important diagnostic complimentary feature in the SERS-based medical imaging has potentially incorporated the SERS into MRI, computed tomography, or fluorescence imaging; due to its single-cell sensitivity; which is absent in lots of its diagnostic counterparts. Furthermore, it would likely become the primary imaging tool for early-stage detection of diseases or to determine post-operative outcomes [18].

1.7 Enhancement Factor

Surface-enhanced Raman scattering is a technique that enhances the signal of Raman scattering of molecules at (or near) the surface by the use of a huge local field enhancement on metallic surfaces taking advantage of localized surface plasmon resonance (LSPR) under the right conditions. The amount of signal enhancement in this technique is essential to be known from both fundamental and applied points of view. The molecular average intensity in normal Raman spectroscopy is directly corresponding to the Raman cross-section of molecules and the laser power density. Generalization of this simple fact leads to the SERS. Simply put, the signal intensity of SERS for a specified analyte in a particular vibrational mode has to be in proportion with the normal Raman cross-section and the laser intensity, but under the influence of an enhancement factor (EF). Enhancement factors of SERS should be real; so that characterizing the obtained enhancement with considering that for the specified molecule under non-SERS conditions. The two major multiplicative contributions of the SERS EFs are:

- The electromagnetic (EM) enhancement factor (F_{EM}) seems to be the most important contribution. This might be due to the coupling of Raman electromagnetic fields and the incident with the SERS substrate which make two separates multiplicative EFs; one relating re-emitted (Raman) field and another for incident fields. The EM enhancement generally relies on huge local field enhancements occurred close to metallic surface in the presence of the localized surface plasmon resonances. The mechanism consists of direct adsorption of the molecule on a surface, either via physisorption or chemisorption (once the chemical bond is formed with the metal).
- The chemical enhancement (CE) factor (F_{Chem}) is another (multiplicative) contribution to the EF. The definition of this factor is subject to controversy; however in any case, its contribution is suspected to be actually lower than the EM factor. In some cases, the CE factor modifies the electronic polarizability of a probe inducing resonant-Raman scattering at wavelengths, where the non-adsorbed molecules would not be resonant leading to signal enhancement. This would be explained with charge-transfer (CT) mechanism which operates on the chemically adsorbed molecules on the surface; which is the same chemical enhancement. However, the chemical enhancement factor contributes to increasing signals to a certain extent, it should be considered basically case by case; because it gave rise by the interaction of analyte molecules and nanoparticles' surface to incorporate all the polarizability tensor effects, and thus, relies on the nature of the analyte and the nanoparticle. The Raman signal enhancement in SERS should also be carefully considered once chemical enhancement factor is regarded as a major component [19].

Compared to the Raman cross-section of an isolated molecule, the SERS enhancement factor represents the amount of increment in the Raman cross-section of a scatterer on a plasmonic surface. The SERS enhancement factor can be obtained by the following equation:

$$EF(\lambda)=\frac{|E_{out}\ (\lambda)|^2\ |E_{out'}(\lambda)|^2}{E_o^4}=4|g|^2\ |g'|^2 \quad (5)$$

where $E_{out}(\lambda)$ and $E_{out'}(\lambda)$ are the quantities of the field enhancement at the NP surface for the incident and at Raman-shifted wavelengths, respectively. The enhancement factor of a particular analyte is determined experimentally by comparing the intensities of the normal Raman and SERS spectra:

$$EF=\frac{[I_{SERS}][C_{SERS}]}{[I_{NR}][C_{NR}]} \quad (6)$$

where I_{SERS} and I_{NR} stand for the intensities of the SERS and normal Raman spectra, and C_{SERS} and C_{NR} are also the Raman scatterer concentration in the SERS and normal Raman spectra, respectively. The quantity of concentration in these two types of spectra are evaluated differently: in a SERS spectrum, the concentration refers to the number of adsorbed molecules on the plasmonic surface has been probed, while in the normal Raman spectrum, the intent is the concentration of the solution in the laser interrogation volume [16].

Everything into account, the sufficient range of EF from 1×10^7 to 1×10^8 has been used for single-molecule detection [23].

1.8 SERS Tag

The composition of a SERS tag includes one or more plasmonic NPs bound to Raman reporter molecules, one or more targeting moieties, and a stabilizing layer for preventing coalescence and fouling (e.g. silica or PEG). Such SERS-active nanoprobes apply laser Raman spectrometry or SERS microscopy for sensing the target molecules by producing strong and characteristic Raman signals. Nanoparticle-based SERS probe benefit optical

labeling functions similar to those of external chromophores such as organic dyes and fluorescent quantum dots (QDs). However, this kind of probe consist excellences such as the ultrasensitivity, multiplexing, and quantitative abilities of the SERS technique, perfectly suited for bioanalysis. The SERS tag due to their inherent features, made progress in the spectroscopic analysis of biological samples. Because these tags offer four main advantages over other optical probes, such as organic fluorescence dyes and QDs. First, SERS tags can provide sufficient sensitivity for trace analysis. Several groups reported that the great SERS enhancement factor led to signals at levels similar to or better than those generated from fluorescence. Second, Raman produces vibrational spectral bands with narrow line widths (~1 nm), and fluorescent bands can be as wide as 50 nm; thus, Raman based probes are inherently suitable for advanced multiplex analysis. Third, the extremely short lifetimes of Raman scattering prevent photobleaching, energy transfer, or quenching of reporters in the excited state, rendering high photostability to SERS tags. And fourth, optimal contrast can be achieved by using red to NIR excitation to minimize the disturbing autofluorescence of cells and tissues, enabling SERS tags to be used for noninvasive imaging in living subjects. Targeting moieties will also contribute to the target selectivity required for avoiding false positive results. In the case of cancer detection using SERS tags, it should be specified that the term “target” is referred to several objects, including a metabolite or blood protein biomarker, a membrane protein specific for a cancer cell, or also a protein specific for cancerous tissue. SERS tags need also to be bright, that is, to identify their targets with high sensitivity. In other words, the tags require hot spots, as near the significant field enhanced locations [18,24].

1.9 The Main Components of a SERS Tag

Taking these protocols into account, nanoparticles clearly need not only opsonization resistance, but also being noncytotoxic. Raman reporters must also tightly bond to the nanoparticle surface (through a covalent bond ideally) that should be protected from enzymatic cleavage as well as acidic conditions which leads to typical endosomal cellular uptake. Additionally, the size of nanoparticles must be in the range of 20 - 200 nm to allow tissue extravasation and cellular uptake while reducing toxicity, signal enhancement and brightness are also provided by built-in hot spots. Gathering of all these conditions and requirements in a single nanostructured tag has been ordinarily a nontrivial task [18].

1.9.1 Nanoparticle

The nanoparticle would better be synthesized through the bottom-up synthetic protocols; due to having longer shelf lives, while with retained morphology as well as confined coalescence. SERS has extremely required the shape retention, particularly in nanoparticles like concave cube. The shape feature such as tips in this kind of nanoparticles activate as a hot spot; as well as they are dynamically evolving due to atom migration and facet reorganization. All these conditions can cause the modification of the tips morphology, thus losing the tag activity. Although the SERS tags can benefit the spherical nanoparticles, but only if they are assembled in the form of dimer, dumbbell or core-satellite systems. The isolated nanoparticles have been confirmed to not provide sufficient enhancement. Further, the characterization of spherical gold nanoparticles has been performed by a localized surface plasmon resonance, show the LSPR peak center around 520 nm. Their limited redshifts leading to the size increase of spherical nanoparticles . Consequently, they can not be possibly excited with NIR radiation, and thus provide insufficient near field enhancement. Instead, nanostars, nanocages, and

nanorice are some isolated non-spherical nanoparticles that can be utilized as enhancement centers in order to produce SERS tags, that is mainly due to their built-in hot spots [18].

1.9.2 Raman Reporter

Another essential component of SERS tag is Raman reporter molecules; the SERS response of which indirectly provides identification of the selected target. Raman reporters have has some specific features, including (1) high Raman cross-sections which cause intense signal responses, typically for the case of conjugated or aromatic molecules; (2) limited number of peaks in Raman spectra to improve selectivity and reduce peaks overlap in multiplexing experiments; (3) laser light insensitivity; and (4) ability of binding with the metallic colloid. All in all, traditional Raman reporters have been aromatic molecules chemisorbed or physisorbed to Au that can be fluorescent or not [18]. These small and rigid molecules have a covalent bond with Au; while having high Raman cross-sections as well as poor fluorescence. Moreover, their well-known chemistry has been challenging for a long time leads to make experimental quantitative estimations for the SERS EFs. Small-molecule Raman reporters, e.g. organic dyes, were also found not to be displaced but having stabilizing effect via thiol-modified polyethylene glycols [25]. Raman-active dyes are incorporated in nanoparticle coatings through several strategies, such as using dyes with chemisorption or physisorption to a metal surface, and those dyes which are closely associated with or covalently bound to other coating molecules. The SERS enhancement would be maximized through dye incorporation methods comprising placement of dye molecules as close to the metal surface as possible. This ensures stable attachment of the dye to the coating structure, thus maintained intensity for the SERS particles over extended time periods [16].

Raman dyes, in most experiments described in this thesis, were physisorbed to Au NP surfaces just prior to coating with thiolated. The mixture was provided by combining dispersed nanoparticle in the MilliQ water and malachite green isothiocyanate (MGITC) as a molecular SERS probe. The isothiocyanate-derivatized dye represented nearly 200-fold higher surface enhancement efficiencies (enhancement factors) than the parent dye. The isothiocyanate derivative has an irreversibly stabilized surface structure which "locked" in its pi-conjugated form with no longer sensitivity to pH. Therefore, the strong surface-absorbate electronic coupling is enabled using conjugated anchoring groups, e.g. isothiocyanate, leading to the more efficient chemical enhancement and thus, higher overall enhancement factors. Spectrally encoded SERS nanoparticles are then developed having improved signal stability and brightness taking advantage of these insights. Raman reporters including Nile blue, crystal violet, cresyl violet, and basic fuchsin were not displaced by thiol-PEG, even without an anchoring isothiocyanate (-N=C=S) group. As a matter of fact, SERS signals related to crystal violet and other dyes have been strongly protected by thiol-PEG being stable for >11 months at 25 ^{o}C. These reporter dyes were positively charged and contained delocalized pi-electrons as the common feature. The negatively charged organic dyes, e.g. sodium fluorescein, have had unstable weak SERS signals on the negatively charged citrate-stabilized gold particles. Thus, strong dye adsorption has been dependent upon both delocalized pi-electrons and electrostatic interactions, possibly at the surface of gold nanoparticles with no competition for thiol-PEG adsorption. The thiol-PEG layer may also cause electronic interactions and steric shielding possibly to protect and stabilize the adsorbed reporter dyes [25].

1.10 Direct vs. Indirect Detection

The mechanism of SERS tags can be fully understood through the comprehension of the difference between “direct” and “indirect” SERS detection. Direct, also so-called label-free, SERS detection has used “naked” nanoparticles to identify the SERS typical spectral features for the analyte. In the direct detection, the native molecules in the environment of the study (e.g., a cell) encounter the sensing volume of the nanoparticle either through random diffusion or the use of capture ligands. Analytes with unsaturated bonds and enriched-aromatic rings would be extremely identified by this method; but the absence of these groups gives rise to highly weak signals. Accordingly, a unique and assignable fingerprinting pattern of peaks related a specific analyte, can be recorded by mixing an NP suspension with an aromatic or highly conjugated analyte. In this regard, opsonization, that is a process where nanoparticles suspended in a biological fluid are covered by multilayered proteins, limits SERS direct identification in the medical fields; due to its negative effect on the signal intensity, the selectivity, and circulation times. On the other hand, the Raman scattering of all molecules in contact with the nanoparticles will be enhanced and create complex spectral analysis. Nevertheless, this direct approach has been used for investigating cytoplasm and other intracellular compartments, DNA and RNA sequencing, and intracellular trafficking of NPs in living cells. In contrast, indirect detection is a completely different approach for identification by the use of SERS tags; which is better suited for highly heterogeneous environments examined in medical fields. In this approach, targeting moieties in nanoparticles is bound to the target for recognition; followed by binding of SERS tags to the molecular target which represents some information about identification and localization. A Raman microscope maps the area of interest to record a SERS signal belonging to the Raman reporter and not the target. Thus, the SERS signal of a reporter indirectly proves the

presence of a target. Introducing nanoparticles with a combination of functionalities and/or reporter molecules are also well-suited for multiplexing, due to the unique SERS spectra associated with each SERS reporter. Consequently, reliable targeting molecules is required for indirect SERS detection; as well as almost absence of nonspecific tag bindings to prevent diagnostic fall-outs due to false positive results [18,24].

1.11 Nanoparticles in diagnosis

In comparison to molecular contrast agents, lots of recent studies have highlighted the role of nanoparticles in medical imaging as the contrast agent because of their longer vascular half-life. Monitoring of these particulate contrast agents is possible for longer times after penetrating to the living organism. This also makes it possible to observe the biodistribution of drugs or radiosensitizers for cancer treatment and available responses to therapy in animal models. As another great advantage, nanoparticle contrast agents have had an ability to gather several complementary properties in the same object. In this regard, multifunctional nanoparticles are developed that are identified by *in vivo* detection using several imaging techniques or imaging and therapy [27]. The target specificity is enabled when nanoparticles are conjugated with several organic vehicles in the tumor microenvironment; e.g. single-domain antibodies (sdAbs) specific for overexpressed proteins on the tumor cell surface or by the tumor vasculature. The single-domain antibody agents can be specifically bound to selected targets. Such a probe localizes the disease *in vivo* and giving insight into critical biological processes of tumor development (e.g., angiogenesis and metastasis), and is, therefore, employed for tumor response monitoring to individualized therapy. This way, treatment may be applied at a curable stage and adjusted if needed [2].

Appropriate nanoparticle size is between the range of 10 to 100 nm. Nanoparticles larger than 100 nm have been easily engulfed by the reticuloendothelial system (RES); even though those having smaller sizes <10 nm are excreted from the kidneys rapidly [28].

Nanoparticles can be employed as diagnostic and therapeutic measures under several specific conditions that must be considered; including the short-term and long-term toxicity, the nonspecific uptake, the biodistribution, routes of elimination and delivery, and bioavailability of nanoparticles. The substantial difference in the characteristics of nanoparticles with macro materials is also of importance. Nanoparticles are actually smaller than human cells enabling the interaction with biomolecules inside or on the surface of a cell. Overall, the intravascular application requires nanoparticles which are stable and easily dispersible, also having long circulation times which indicates no uptake by the reticuloendothelial system. However, a safe excretion is guaranteed by programmed clearance mechanisms. Nanoparticles should have high specificity and sensitivity for the target with the difficult occurrence of unspecific binding [29,30].

Application of nanoparticles combined with MRI technique is particularly capable of cancer staging, following up the treatment progress and accurate detection of disease [2]. paramagnetic gadolinium-based contrast agents play an important role in shortening relaxation times of water protons and are used to increase image contrast. However, the use of these Gd(III) CAs in molecular imaging has been limited due to their low sensitivity and high concentrations needed to make a satisfying contrast (10–100 mM). Many biomolecules are remarkably found at concentrations of 0.1–1 mM, just below the Gd(III) CAs' detection limit. To date, some biomarkers have been detected by Gd(III) based molecular imaging having high concentrations *in vivo* [31]. Furthermore, the free Gd(III) ions are highly toxic and the clinically used Gd(III)-chelates, like DTPA and DOTA, endure rapid renal clearance, poor sensitivity ($r_1 \sim 3$ mM−1·s−1 at 4.7 T) and lack of specificity

caused by their small molecular size. The Gd(III) was attemptedly incorporated into or onto nanoparticles in order to improve their sensitivity through enhancing the specificity, reducing the toxicity and prolonging circulation time. Nanostructured Gd(III) contrast agents have, therefore, enhanced relaxivity in comparison to free Gd(III) chelates as a result of two reasons; the enhanced r_1 for the nano-complex due to reduced global tumbling motion and cumulative effect of much more Gd(III) ions per nanocarrier [11].

The SBM theory of paramagnetic relaxation represents the crucial factors affecting the relaxivity of Gd(III)-based agents, including water proton residence lifetime, number of coordinated water molecules, water exchange rate, and molecular diffusional and rotational times [11]. Altering the chelate design causes to optimize τ_m and change of q. Then, decreased molecular diffusional and rotational times lead to increased T_1 relaxation time, especially at weak magnetic fields. Therefore, in the case of Gd(III), the incorporation of it into nanostructures reduces its molecular tumbling rate, and thus, increases its diffusional and rotational correlation time, leading to increase the relaxivity. In addition to the enhanced T_1 relaxation time, carrier accumulation in the target tissue is increased by the nanostructured systems. For instance, nanoparticles achieve the enhanced permeability as well as retention effect in tumors exploited for passive targeting, the local concentration of which would be then increased in the tumor [11]. Therefore, the sensitivity and accuracy of medical diagnosis has been improved by the nanoparticle. Among various metallic based nanoparticles, gold nanoparticles are evidently proximal to Gd(III)-based agents serving as “nano-amplifiers” in order to increase the MR relaxivity [12,20].

Also application of nanoparticles in Raman spectroscopy, known as multifunctional SERS nanoprobes, have been developed to *in vitro* and *in vivo* target specific biomolecules by the combination of metallic nanoparticles and molecular Raman reporters, as it is

describe before, providing Raman-based optical bioimaging with the characteristics of excellent photostability and high spatial resolution [32].

1.12 Gold Nanoparticles

Gold has been subjected to the most ancient scientific investigations, and now, an exponential increment of publications represents its renaissance, especially for the emergence of nanotechnology and nanoscience with nanoparticles as well as self-assembled monolayers [33]. The synthesis of monodisperse nanoparticles using noble metals has significantly advanced in the past decade which have diverse shapes, from simple spheres to branched multipods. The bioimaging applications have employed the gold nanoparticles due to unique optical advantages on the basis of surface plasmons as well as their inertness and excellent stability with diverse molecules by using the well-known chemistry comprising alkanethiol adsorption onto gold [23,24]. In biomedical application, the easily obtained derivatization of gold nanoparticles has been crucial for the development of new tools to meet the clinical needs [27]. The importance of the surface chemistry in such structures is highlighted especially for much higher ratios of surface to bulk atoms relative to that in microscopic or macroscopic systems [7]. Facile surface modification is also available through the reaction and molecular self-assembly of thiolated (-SH) moieties on the gold surface. Additionally, gold has a high affinity to amino (-NH2) and cyano (-CN) groups [36-38]. Other groups on gold NP surfaces are thiolated polyethylene glycol (PEG-SH) as well as alkanethiolates and alkaneamines [38,39]. Having *in vivo* stealth character, PEG is specifically popular due to increased biocirculation time by discouraging protein adsorption to the nanoparticle surface and thus, preventing uptake by the reticuloendothelial system [40-42]. The surface chemistry has also employed dyes or markers to enhance the imaging or sensing properties [39,42].

The structure control and chemical functionalization of NP surface are, indeed, of interest to discover new applications and properties for this substantial class of materials.

On the other hand, the plasmonic is expected to have a particular influence on the life sciences through applications in therapeutics, diagnosis and imaging [21]. At the boundary of two materials, electron density fluctuations are known as surface plasmons, the oscillation of which have been due to the response to an applied field. The localized surface plasmon resonance may occur in cases of matching the light frequency and resonance conditions for the nanoparticle. These resonance conditions depend on the shape and size of the particles, the dielectric function and characteristics of the embedding medium. Regarding the LSPR effect as well as enhanced absorption crosssections, gold nanoparticles exhibit narrow but intense optical absorption bands. Surface plasmons are also often sensitive to boundary changes, such as molecular adsorption onto these nanoparticles. Subsequently, SERS through enhancement of relatively weak Raman scattering is occurred by the Raman field in resonance with the local surface plasmons of gold nanoparticles and the field strength at the laser excitation wavelength [43].

As the optical properties, colloidal gold nanoparticles can amplify the efficiencies of Raman scattering for the adsorbed molecules from 10^{14} to 10^{15} which allows spectroscopic identification and detection of single molecules under ambient conditions [25].

1.13 Size of Nanoparticles

For the efficient diagnosis and treatment of solid tumors, understanding the principles governing the design of nanoparticles for tumor targeting is crucial. The effective tumor-targeting and cellular uptake is largely influenced by nanoparticle size. One of the

advantages of nanoparticles is that their size is tunable. The size of nanoparticles used in a drug delivery system should be large enough to prevent their rapid leakage into blood capillaries but small enough to escape capture by fixed macrophages that are lodged in the reticuloendothelial system, such as the liver and spleen [44]. Consequently, nanoparticles of less than 100 nm are generally appropriate for anticancer drug delivery due to selective and preferential accumulation at tumor sites owing to the effect of enhanced permeability and retention (EPR) concept. The nanoparticles can penetrate the tumor deeply and uniformly by overcoming interstitial transport barriers that is arised by some features of tumor microenvironments, including increased interstitial fluid pressure, the aberrant vasculature and dense extracellular matrices. Sykes et. al. have reported the nanoparticles in the range of 40-60 nm are highly suited to receptor-mediated endocytosis and exhibiting higher tumor accumulation rates relative to smaller nanoparticles with the size of about 15 nm. From the tumor permeability standpoint, nanoparticles smaller than 20 nm pass through tumor tissues rapidly, whereas larger ones primarily accumulate just around vascular tissues [29,30].

1.14 Shape of Nanoparticles

Nanoparticle customization has been established by one of the most useful parameters, the shape, that has the challengeable intentional control [47]. The importance of such controlling is extremely respected to noble metal nanoparticles, structures of which, including the shape and size, prescribe the plasmonic properties; As in the nanometer system, almost all properties are shape- and size-dependent [26,32]. Various nanostructural features highly affect the optical properties and signals of plasmonic nanostructures. Quantifiable and controllable plasmonic signals are then obtained by high-yield deliberate synthesis of these nanostructures [32]. In order to control the growth

and the size in the nanometer scale, common methods employ capping agents, including ligands, surfactants, polymers, or dendrimers, producing spherical particles owing to their low surface energy [48]. The morphology of nanoparticles has been chemically controlled by some synthetic strategies to provide desired optical, electrical, catalytic and magnetic properties [17]. Specifically, Au NP surface curvature may have an influence on the physicochemical properties of conjugated ligands, e.g. the effective acidity constant (pKa). Also the effect of shape on the enhancement of T_2 relaxivity (r_2) been observed previously for superparamagnetic nanoparticles such as iron oxide [31].

Irregular shaped nanoparticles, in addition to the SPR absorbance shift, it has also a larger surface area to volume ratio in comparison with a conventional spherical nanoparticle. These irregular shapes can bind to more drug molecules, present several targeting ligands , act as a sensitive contrast agent and have a various cellular interactions [49].

The two fundamental structural factors to control nanoparticle shape are crystallinity and surface facets. Correspondingly, crystallinity is essentially defined in particle formation, in the early nucleation stages, but surface facets can be uniformly established shortly afterwards when the particle grows.

Nanoparticles can be categorized as single-crystalline or polycrystalline structures, with zero or several defects, respectively, or they may also contain various but confined crystal defects. For instance, metals with the face-centered cubic (FCC) structure, e.g. Au and Ag, have commonly stacking faults and twin defects. Disruption of abcabcabc stacking patterns in atomic layers of the metal in fcc unit cell occurred by an added or missing layer, e.g. abcabacabc, has been stacking faults. A twin plane can also be formed when the disruption causes to mirror the present stacking pattern relative to one of the layers (i.e. abcabacba) (Figure 4). Twin defects are very common in fcc metals with very small

energy barriers; because each layer has the same atomic coordination number whether in the perfect crystal or in the presence of a twin defect. A single nanoparticle can also have multiple twin defects, widely observed in Au nanoparticles as the form of planar-twinned (with one or more parallel twin defects), penta-twinned (five twins radiated from a central point) and multiply twinned (with 20 intersecting twin planes). Considering the impact of nanoparticles' twin structure on the determination of symmetry, the particle exact shape highly depends on the surface structure. The facets are surfaces with a particular atomic arrangement; which is exposed in a polyhedral metal nanocrystal. This atomic arrangement depends on the angle of exposed surfaces respecting the overall atomic lattice structure of the metal unit cell. Thus, facets can be determined by a set of integers, so-called Miller indices, representative for the plane orientation of the facet regarding the unit cell. As an example, {100} surface facets are for cubes with the plane lying along the face of an fcc unit cell (Figure 5). Low-index facets have the Miller index, {111}, {100}, or {110}, with all the integers as being 1 or 0, representing the lowest-energy surfaces in cases of fcc nanoparticles.

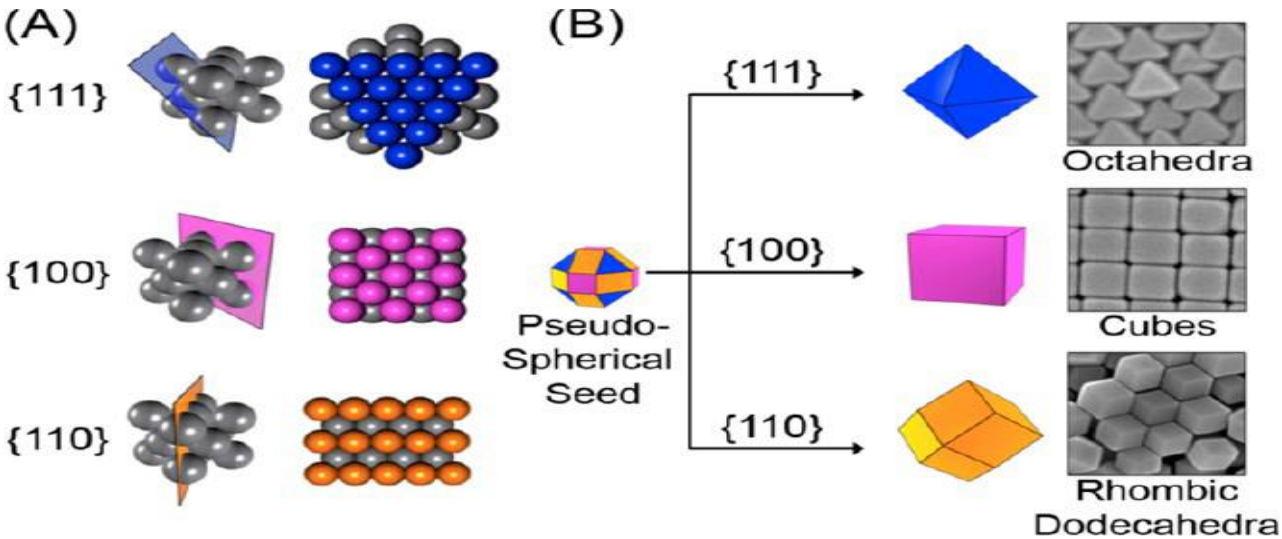

Figure 4 Model of a twin plane in a face-centered cubic metal: (A) fcc lattice; (B) fcc lattice with the repeating abcabcabc stacking pattern annotated; (C) annotated fcc lattice from (B) oriented to the [110] zone axis so that the {111} repeating layers are more easily visible; (D) annotated fcc lattice which contains a twin plane, as viewed down the [110] zone axis [50].

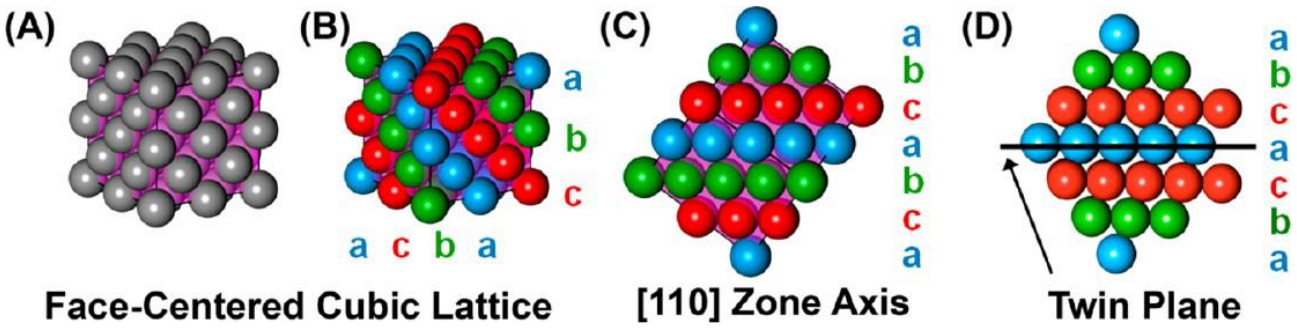

Figure 5 (A) Models of the low-index surface facets of fcc metals, such as Au. (B) Models (left) and scanning electron microscopy (SEM) images (right) of representative polyhedral nanoparticle shapes bound by each of the low-index facets [50].

Anisotropic Au nanoparticles are predominantly formed following the growth pathway of either (1) kinetic control, or (2) selective surface passivation. The shape of nanoparticles, under the kinetic control route, is determined by the overall reduction rate for the metal ion (e.g. reduction of Au^{+} for Au nanoparticles). On the other hand, the selective surface passivation of a particular facet with the bound adsorbate (for example, Ag in the Ag^{-} assisted synthesis of Au nanoparticles) assures the formation of nanoparticles through slowing the growth of one type of facet down than other facets. Due to rapid deposition of Au on un-passivated surfaces, Au NPs grow until developing the same facet structure as the passivated surface resulting in entire particle binding by the passivated facet.

Gold nanoparticles with a desired shape can be fabricated by the thermal seed-mediated synthesis comprising two main synthetic steps: (1) the rapid reduction of metal ions (Au) to form highly monodisperse and small spherical Au nanoparticles, or namely seeds, and (2) further growth of larger nanoparticles through slow reduction of additional Au onto the previously synthesized seeds (which serve as nucleation sites) in the presence of shape-directing additives. Temporally separation of formed nanoparticles ensures the presence of monodispersity in the final colloid of nanoparticles. Control of size is also possible in seeded growth through adjustment of the seed and Au ion concentrations ratio. In a constant concentration of ionic Au, the addition of more seeds leads to more, but smaller, particles; in contrast, fewer seeds generate fewer, but larger, particles [50].

Nanostructures produced by the thermal seed-mediated synthesis, have consisted of Platonic solids, e.g. octahedra and cubes, plates and prisms and more exotic facet structures with high-index facets. The kinetic control of directly synthesizing NPs with a particular shape has been addressed by making a change in the concentration of ascorbic acid (AA), as the reducing agent. More kinetically desirable (or less thermodynamically desirable) particle morphologies are preferentially grown by increasing the reduction rate of gold ions caused by an increase in the quantity of reducing agent within the growth solution. Higher concentrations of the reducing agent make particle binding with higher-energy surface facets. Anisotropic nanostructures grown in this synthetic pathway are essentially fabricated with the use of additives, such as most common halides and silver ions. Silver ions are popular because of incorporating in the stabilization and growth of gold nanostructures with high-index facets, as reported in several studies. Considering the near-monolayer of silver binds the surface of gold nanoparticles through the underpotential deposition (UPD), sensible control of the growth solution in terms of silver ion concentration lets the selective preparation of various gold nanostructures, such as {110}-faceted rhombic dodecahedra and bipyramids, {310}-faceted truncated tetragonal prisms, {720}-faceted concave cubes, and {111}-faceted octahedra with tailorable hollow features [47]. Comprehensive mechanistic studies represented the passivation and stabilization of more open facets through deposition of more Ag onto the growing gold nanoparticles exposing much more surface atoms. The novel nanostructures, such as concave cubes and tetrahexahedra (THH),are prepared by this method having high-index open surface facets. With respect to divergent mechanisms of these two growth routes, the synergistic effects have directed nanoparticle growth in both pathways having basic chemical principles: I) metal ion availability, II) adsorbate binding strength and III) the potential of reduction for the metal complexes. These parameters have impacts on

surface facets and the crystallinity of Au nanoparticles; thus controlling particle shape. The three chemical parameters described for nanoparticle growth, modulate the quantity of Ag reduction onto the surface of gold nanoparticles through underpotential deposition. As a result, underpotential deposition of Ag on Au took place in this system with regards to the potential of reduction for the metal ions respecting the reducing agent strength (i.e. ascorbic acid), which is addressed by the reduction of near-monolayer of silver onto the available gold surface at a potential being positive considering the Nernst potential for Ag. The underpotential deposition of Au nanoparticles is suitable at low-pH conditions ordinarily concerned in these synthetic approaches (pH ~2); because of non-strong enough AA for Ag^+ reduction. Deposition of a near monolayer of silver onto the growing gold nanoparticles is possible which is facilitated by the nanoparticle surface; unregarded to the mismatch between the potential of reduction for Ag^+ and the reducing agent strength. The parameter of metal ion availability has an impact on the UPD process in the presence of halide ions in solution along with growing Au nanoparticles and Ag^+ ions. The solubility order for Ag^- halide complexes is AgCl > AgBr > AgI. Lower amounts of solubility decrease the quantity of Ag^+ to be reduced leading to slower Ag deposition and lower Ag coverage on Au nanoparticle surface, as well as stabilizing fewer open facets. The binding strength of the adsorbed Ag (AgUPD) is also affected by halide ions. The growth processes with controlled Ag UPD depend highly on the Ag-Au surface binding strength. surface chemistry investigations of Ag UPD revealed that Ag preferentially binds to Au facets with more exposed surface atoms as well as kinks and step edges. These sites basically provide a great coordination number, and hence, enhanced stability for deposited Ag atoms. Herein, silver acts as the capping layer to stabilize high-index facets. Consequently, UPD Ag causes selective passivation of facets with lots of exposed surface atoms depending on Ag^+ concentration in solution, the Ag deposition rate on the

surface and the stability of the AgUPD adlayer. Lack of sufficient Ag content on the surface of nanoparticles for complete particular facet passivation makes the facet to grow while Ag is present on the surface leading to full passivation by stabilization of less open facet ultimately. In these growth reactions controlled by Ag UPD, the Ag-Au surface binding influences the total kinetics of Au^{+} reduction and slows the Au^{+} reduction rate down at all concentrations of Ag^{+}. That is because of the limited amount of available Au surface area for the Au^{+} reduction catalysis; due to the presence of Ag on the surface of nanoparticles. The thermodynamically desired {111}-faceted nanoparticles, like octahedra, are even formed simply through a kinetic growth mechanism under insufficient Ag deposition for full stabilization of a particular facet; which might because of the slow Au^{+} reduction rate. Noteworthy, all Ag-assisted growth reactions have associated with relatively slow Au^{+} reduction rates with no significant difference in the rate at different concentrations of Ag^{+} make it irresponsible for shape control. Therefore, the growth based on selective surface passivation is controlled kinetically at higher Ag coverages. Considering the objective of maximizing the Ag-Au binding strength through strong coordination, halide ions have a substantial impact on the AgUPD adsorbate bound with Au nanoparticles representing different binding strengths caused by the interactions of halide ions with Ag as well as Au surfaces. In the case of seed-mediated synthesis, there are some diverse, while conflicting theories to express the role of halides; in both the presence or absence of silver ions. In this regard, the {100}-faceted nanoparticles, i.e. cubes, are fundamentally formed through the stabilization of {100}-faceted surfaces, when bound to bromide anions; causing to slow gold deposition down at that site. Some of other contributions of bromide ions also include the bromide selective binding to {110} or {111}-faceted surfaces or formation of cetyltrimethylammonium bromide (CTAB) micelles, bilayers, or CTA-Au-Br complexes to slow gold deposition rate down.

Association of bromide and silver ions in the solution leads to fabricate silver bromide (or CTA-Ag-Br), that may have selective deposition onto certain surfaces, most probably through adsorption or underpotential deposition. The more complicated case of iodide has only emerged more recently. Iodide has been argued to bind to {111} facets for stabilization; although some literature has reported its role as a reducing agent which increases the $[AuCl_4]^-$ reduction rate. However, contradictory results are reported that iodide can slow down the growth of gold nanoparticles. Association of iodide and silver ions also dominates the efficiency of silver ions in particle growth. Taking everything into account, iodide (1) binds to the surface having silver ion to form a silver iodide layer, (2) acts as a catalyst to reduce gold ions onto {111} surfaces, and (3) observes gold nanoparticle growth being as a nucleation site [47]. Due to a relatively equal strength of chloride binding to Au and Ag surfaces, it does not compete with Ag significantly to bind to Au surface. It can be concluded an AgUPD layer in this case, possesses enhanced stability compared to that accompanied by any other halide ion. Chloride ion makes much more Ag to reduce rapidly onto the surface of Au nanoparticles and stabilizes the surfaces, making the Ag displacement or rearrangement difficult except through slow oxidative dissolution and re-reduction. Consequently, the chloride-containing surfactant provides diverse shapes by stabilizing the growth of Au nanoparticles which cannot be observed in bromide- and iodide-containing surfactants. Concave cubes gold nanoparticles (CCGNPs) are also likely formed as a result of added stability through the establishment of a concave structure from early stages of the growth; providing the concave cube with smaller center portion and preventing its rearrangement to form a convex nanostructure. Additionally, tetrahexahedra are stabilized by only 37−47% of a monolayer of Ag deposition on their surface; because bromide destabilizes the Ag

adlayer; while in CTAC possess, as-synthesized shapes have much higher Ag coverages (~80%) [50].

As well, more silver deposition is obtained onto the gold nanoparticle surface by adding trace amounts of bromide or iodide to growth solutions which contain a silver ion additive in CTA-Cl, both of which destabilize the AgUPD layer, iodide has more significant destabilizing effect than that for bromide. As the hypothesis, destabilization of the AgUPD layer by bromide or iodide provides silver more opportunities with rearrangement on the particle surface, through either an oxidation-redeposition cycle or local surface mobility. The surface mobility provides more energetically desirable surface sites, including atomic steps or also corners, facilitating the silver relocation. More surface atoms are thus exposed by facets allowing the stabilization at lower silver concentrations than those required in the case of using chloride only. Opposite to the case of chloride, in the presence of bromide or iodide the higher mobility imparted to an AgUPD layer and gives rise to the faster Au ion reduction rate onto the particles; since the gold deposition is easily accessible on more dynamic surfaces. The application of halides in the shape control for gold nanoparticles has specially been illustrated in the process of silver assisted syntheses of tetrahexahedra and concave cubes both bound to similar high-index facets. These two types of nanoparticles are produced under nearly identical synthetic conditions, but like the synthesis of {720}-faceted concave cubes in cetyltrimethylammonium chloride (CTAC), the analogous bromide-containing surfactant, CTAB has the same synthesis results in convex {730}-faceted tetrahexahedra (Figure 6). Some closely relevant shapes known as a cube contain either square-pyramidal depressions or square pyramids on each of the six faces being concave cubes or tetrahexahedra, respectively. Concave nanostructures are uncommon in any case of

synthetic methods, which grow desirably under growth conditions controlled by kinetics. Considering the concave cubes proposes the hypothesis that the convex tetrahexahedra have been more thermodynamically desirable structures due to their more isotropic shape. It is believed that the relatively higher AgUPD layer stabilization in the presence of chloride and faster gold ion reduction rate in CTA-Cl, make the concavity of the concave cubes; which can be resulted in less thermodynamically desirable condition. Due to the formation of stable AgUPD layer in chloride, the silver underpotential deposition in the presence of a surfactant having chloride effectively “locks in” a particular surface facet early in the reaction.

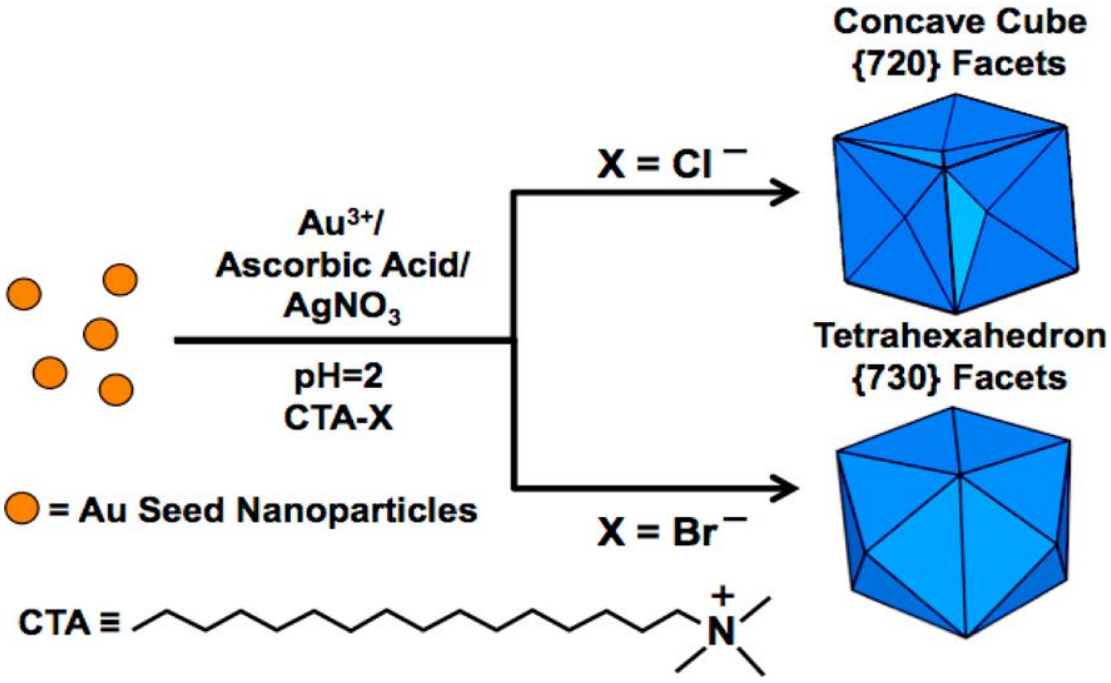

Figure 6 In a seed-mediated synthesis of gold nanoparticles, the use of a silver ion additive in the presence of a chloride containing surfactant (CTAC) results in the growth of {720}-faceted concave cubes (upper growth pathway), while the use of a bromide-containing surfactant (CTAB) under otherwise identical conditions results in the growth of {730}-faceted tetrahexahedra (lower growth pathway) [47].

Transmission electron microscopy images have shown that small growing seed particles have the shape of small concave cubes even at the early stages of the concave cube reaction. These small concave cubes continue to grow during the process by maintaining their shape until reaching the final size. It was found that smaller diameters of seed

particles (~7 nm) are influential for the concave cube's growth; perhaps because of the higher reactivity in smaller seeds. This was confirmed when using seeds with a diameter of ~40 nm, where despite the enough concentration of silver ions to produce the concave cubes (100 μM silver ion), the truncated tetragonal prisms nanoparticle is formed. Thereupon, the large seed does not have enough reactivity to support concave features; due to the lack of enough energy to overcome the high energy barrier for concave growth [47]. High-resolution images of the nanocube have shown the FCC structure for Au correlating the cubic faces of nanoparticles with {100} planes in the FCC structure [51].

1.15 Concave Cube Gold Nanoparticles

Gold nanorods (AuNRs) and nanoprisms are the most common anisotropic gold nanostructures [52]. On the other hand, to date most synthetic methods are generally employed to obtain convex shapes nanostructures with low-index {100}, {110}, and/or {111} facets, while high-index faceted nanostructures are formed by very few methods. The concave nanostructure is unusual. The present concave cubes are nanocubes with the "pushed in" centers on six square faces which make square pyramid-shaped depressions, yielding a nanostructure enclosed by 24 facets. Zhang et al. have examined the synthesis of high-index {720}-faceted Au concave nanocubes by modifying seed-mediated methods with the proper surfactant . They believed that concave cube morphology yields due to the combination of Ag^+ and Cl^-. High-index facets are stabilized through an underpotential deposition mechanism by Ag^+ in other seed-mediated syntheses. Noteworthy, cyclic voltammetry (CV) and correlated scanning tunneling microscopy experiments highlight the significant effect of Cl^- on Ag^+ UPD on the gold; more difficult removal of Ag^+ would be due to that fact that Ag^+ has been deposited specifically onto atomic steps below a Cl^- adlayer. High-index faceted nanostructures are

synthesized using both CTAB and CTAC the latter has shown stellated features for nanoparticles. There is a need for investigating the features of anisotropic nanoparticles, silver physicochemical role in the shape control, and the nature of silver moieties on the surface of nanoparticles. The association of CTAC and silver ions leads to the formation of silver bromide or a CTAC–silver bromide complex. Further, underpotential deposition of Ag(I) has made a monolayer or submonolayer of Ag(0) onto nanoparticles with similar results [53]. The surface structure of the bulk gold is usually studied by CV and surface facets of gold nanostructures are recently characterized by this method. Based on the CV, different sizes of concave cubes exhibit some oxidation peaks around 1.2 - 0.5 V. This value is comparable to the peak related to THH Au nanoparticles enclosed by {730} facets, which was measured to be 1.18 V.22 For instance, the octahedral Au nanoparticles (edge length 80 nm) have an oxidation peak of about 1.43 V. Since the oxidation peak of concave cubes is at a lower potential than the octahedra, the atoms on the surface of concave cubes seem to be oxidized easier. In this regard, {720} facets have a more open atomic arrangement than {111} facets of the more tightly packed octahedra. As a result, higher-indexed concave cubes clearly have higher activity than nanoparticle shapes bound with low-index facets. The concave cubes represent red-shifted plasmon resonance by about 80 nm when compared with cubes having flat surfaces with similar dimensions. In fact, the red-shifted plasmon resonance has been theoretically expected for the concave cubes with sharper tips relative to cubes with flat faces [17]. The Au concave nanocubes, nanostars, and nanotrisoctahedra nanoparticles having tipped surface structures contain intense near-field enhancements that are exploitable for single-particle surface-enhanced Raman spectroscopy (spSERS) under near-infrared excitation [54]. Extremely sharp corners of the concave cubes have enabled the synthesis of highly localized hot spots as well as large electromagnetic-field

enhancements [43]. In cubic gold nanoparticles, there are eight similar sharp corners localizing uniform, high near fields. Furthermore, the concavity of the particle lateral planes increases such field intensities and tunes in the near-infrared region without making a change in the overall size of nanoparticles [51].

1.16 Functionalization (Coating)

The high surface energy of nanoparticles makes them unstable and in many biological fluids, they often aggregate; because of the high ionic strength and non-specific interactions with biomolecules including proteins or DNA. Moreover, large aggregates may also be produced through the adsorption of blood plasma proteins onto the bare AuNPs surface; resulting in different pharmacokinetics and biodistribution for Au nanoparticles. Therefore, the organic capping layer coated nanoparticles have provided a protective and solvent-compatible coating that counteracts the aggregation caused by attracting forces between nanoparticles [32]. This coating also makes them visible to cells in the mononuclear phagocyte system [55].

Tunable self-assembled plasmonic metal nanoparticles are largely considered in the design of new diagnostic and therapeutic devices; as well as in applications of fundamental studies on plasmon-enhanced phenomena including surface-enhanced Raman scattering [53]. Thus, the solubility, stability and retention of optical properties, when exposed to various media, are provided through surface functionalization as an important point during nanoparticle preparation [56]. The three general coatings employed in processes include 1) biomolecules, i.e. bovine serum albumin; 2) polymers, i.e. PEG, and 3) glasses, i.e. silica [18]. In this regard, the assembly of AuNPs and tuning of their surface properties are attractively investigated by the utilization of different biomolecules.

Cetyltrimethylammonium bromide/chloride-coated (CTAX) Au nanoparticles which are synthesized by various methods, are not appropriate surfactants for biological applications owing to the cytotoxicity. Although the crystallinity and shape of nanoparticles can be controlled in the presence of silver ions and CTAX which contribute to prepare non-spherical particles by forming densely packed bilayers on the surface of nanoparticles. To synthesize nanoparticles with irregular shape, the association of CTAX (cetyltrimethyl ammonium chloride/bromide) as a stabilizer with silver ions as a shape director is crucial, while may complicate surface functionalization through conventional gold–thiol chemistry. Regardless of compromising particle stability, the surface chemistry customization for CTAX-capped nanoparticles have difficulties with limited applicability in analytical apparatus. A wide variety of CTAX functionalization approaches, such as physisorption of polymers, have been proposed to stabilize particles and give them biocompatibility and chemical versatility. Mirkin et al. demonstrated the efficient functionalization of gold nanoparticles, by thiolated single-stranded DNA, through after-synthesis growth of a thin gold film onto the CTAB AuNRs. As a hypothesis, they found that the stabilized Au–S bond is prevented to be formed due to the deposited silver at the surface of nanoparticles; which makes it difficult to immobilize DNA before the overgrowth procedure. Nakashima et al. have used Surface Assisted Laser Desorption-Time of Flight Mass Spectroscopy (SALDI-TOF MS) to identify the adsorbed $AgBr_2$ onto the particle surface on account of an important component influencing the shape. The presence of silver on the surface of most particle forms, besides CTAB, is probably in charge of difficulties for surface functionalization. Wang et al. examined the effect of silver concentration on the surface of arrowhead Au NRs with well-defined {111} facets for the particle functionalization. They further demonstrated that an additional gold layer provides particles with homogeneous functionalization by thiol-containing molecules [53].

1.16.1 Polyethylene glycol (PEG)

Several reports have claimed the minimizing role of Polyethylene glycol in nonspecific proteins adsorption onto nanoparticles as well as reducing their uptake by the liver. Based on a recent investigation, PEG-coated gold nanospheres, nanorods and nanoshells exhibit prolonged circulation time *in vivo* by systemic injection; consequently improving pharmaceutical efficacy [57]. The larger hydrodynamic radius for the conjugates and hindering glomerular filtration, makes a less renal clearance. Protective effects may also be due to the hydration and steric repulsions between PEGylated pieces [58]. Using PEG as a biocompatible polymeric coating stabilizes the tag with retained biocompatibility, providing chemical end groups at the same time to make it prone to surface functionalization in order to bind targeting moieties strongly to the tag [18]. Manson et al. Investigate the PEG-coated AuNPs at salt concentrations of 0.15–1 M which represents its stability, while citrate-capped AuNPs aggregate immediately under such conditions [59].

Two different conformations adopted by straight-chain molecules in the self-assembly of polymer monolayers depends on the density of molecules deposited on the metal surface. The distance between non-overlapping polymeric molecules in a good solvent is described by the Flory radius (R_F):

$$R_F = \alpha n^{3/5} \quad (7)$$

where α is the unit length of the monomer (3.5Å for PEG), and n stands for the number of repetitions in the polymer chain (45 units for 2 kDa thiol-PEG). A more diffuse mushroom configuration is adopted by PEG for intermolecular distances greater than R_F. An increment in PEG density and decline the distance between adjacent molecules relative to R_F, lead to a more extended and densely packed brush configuration on the surface to incorporate numerous molecules (Fig.7). This exclusivity insures that

bioconjugation with functional groups at the surface is accessible; while the more diffuse configuration resulting in burying functional groups within the PEG layer [16].

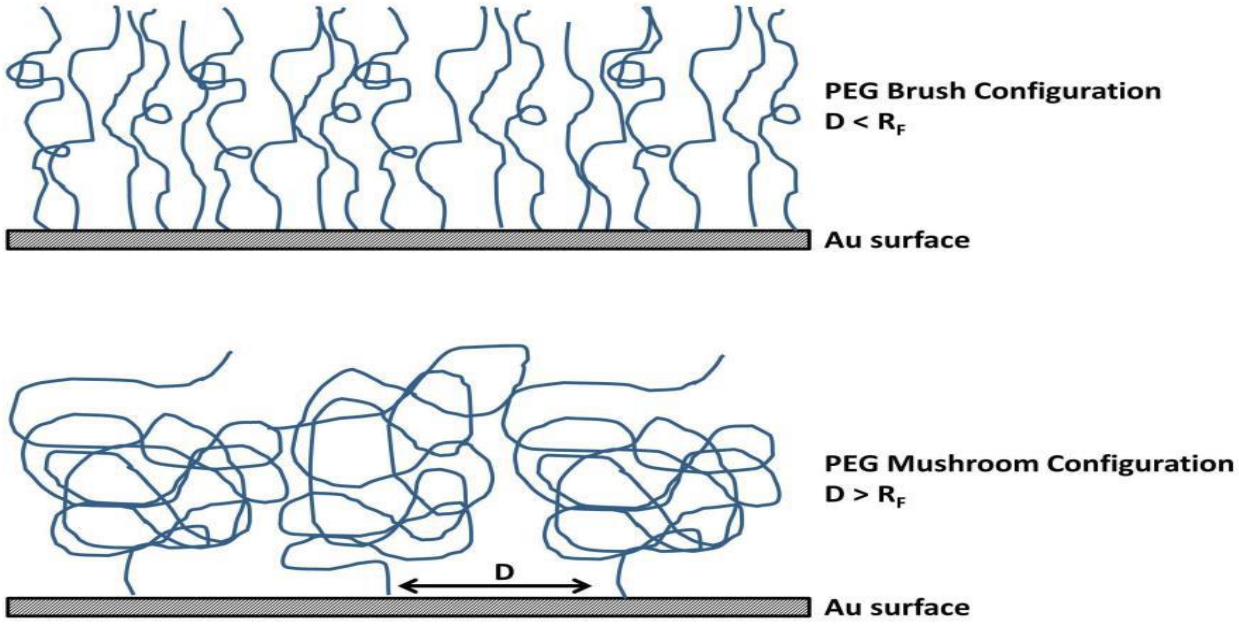

Figure 7 Brush and mushroom configurations for polyethylene glycol molecules attached on the gold surface. The distance between adjacent PEG chains determines the molecular conformation [16].

The relationship between the structure of PEG layers and their bioactivity has been of importance to many research works; so that optimal properties are reported to be obtained at high chain grafting density resulting in the formation of polymeric brushes extending into the solvent phase [60].

1.17 Tumor Targeting

The distribution of conventional chemotherapeutic agents is available non-specifically throughout the body with impacts on normal as well as tumoral cells. Therefore, tissue selectivity has been of importance, regarding the effectiveness of novel pharmacological agents. Controlling the non-specific interactions with diverse biological entities, including proteins and cells, has been also crucial for the successful utilization of functional

nanoparticles in applications such as biosensing, biodiagnostic and therapeutic. For instance, biosensing applications have critically sought to maximize the specific binding events for the purpose of achieving high signal-to-noise ratios, i.e. for antigen/antibody interactions. The biointerfacial properties directly focus on the fate of nanoparticles *in vivo*, and thus, their capability of being molecular contrast agent or therapeutic agent and resistance to non-specific adsorption events [60]. The exploitation of tumor vascular abnormalities is an attractive idea; particularly to avoid penetration into normal tissue interstitium, but an allowance for getting access to tumors. Some of advantages of specific tumor targeting in nanocarriers comprise better pharmacokinetics and pharmacodynamics profiles, controllable and sustained drug release, an improved specificity, an enhanced internalization, intracellular delivery and above all, lower systemic toxicity. Accordingly, the tumor-targeting comprises two approach "active targeting" and "passive targeting" so that the active targeting process occurs in tumors only after passive accumulation. Structural changes made in vascular pathophysiology can also provide opportunities to employ long-circulating particulate carrier systems. Particular abnormalities found in tumor blood vessels that are generally considered for tumor characterization include a high number of proliferating endothelial cells, aberrant basement membrane formation and pericyte deficiency leading to an improved vascular permeability. Nanocarriers, as particles with the size range of 20–200 nm, are capable of being extravasated and accumulated inside the tumor interstitial space. As well, the sizes of endothelial pores vary from 10 to 1000 nm. On the other hand, the absence or non-functionality of lymphatic vessels in tumor associates with inefficient drainage from the tumoral tissue. The metal nanoparticles are accumulated in target tissues, due to non-specific physicochemical characteristics (such as size, hydrophobicity, surface charge) through passive targeting processes. These nanocarriers are retained in the tumor and

cannot be removed efficiently. Matsumura and Maeda discovered this passive phenomenon introduced it as “Enhanced Permeability and Retention effect” (Fig. 8A). Active targeting contains the attachment of targeting ligands to the surface of nanocarriers in order to bind to appropriate receptors; specifically expressed at the target site (Fig. 8B). The elected ligand binds to the overexpress receptor in tumor cell or tumor vasculature which is absent in the normal cell. Moreover, the expressed targeted receptor should be homogeneous on all targeted cells. Ordinarily, targeting ligands are monoclonal antibodies associated with either antibody fragments or non-antibody ligands (peptidic or not). The tumor penetration might be under the influence of the ligands binding affinity, due to the presence of ‘‘binding-site barrier’’. For targets like tumor vasculature with readily accessible cells, high-affinity binding would be preferable, due to the dynamic flow environment of the bloodstream. Antibodies, either monoclonal or fragments, such as bevacizumab (anti- VEGF, Avastin®), trastuzumab (anti-ERBB2, Herceptin®), or etaracizumab, a humanized anti-$\alpha_v\beta_3$ antibody (Abegrin) would target a specific receptor; thus interferes with signal-transduction pathways and regulates proto-oncogenes involved in proliferation of cancer cells. The active molecule of this case is considered both as targeting ligand and as a drug [61]. Antibodies and aptamers are ideal targeting molecules; antibodies are appropriate since they are available for the extended range of targets, while sturdier and cheaper aptamers, such as oligonucleotides with high specificity for folding and binding to targets, have not been much developed for various targets [18]. In addition, conjugation of gold nanoparticles with certain peptides causes cell nuclei to be effectively targeted and providing opportunities in the gene therapy applications [62].

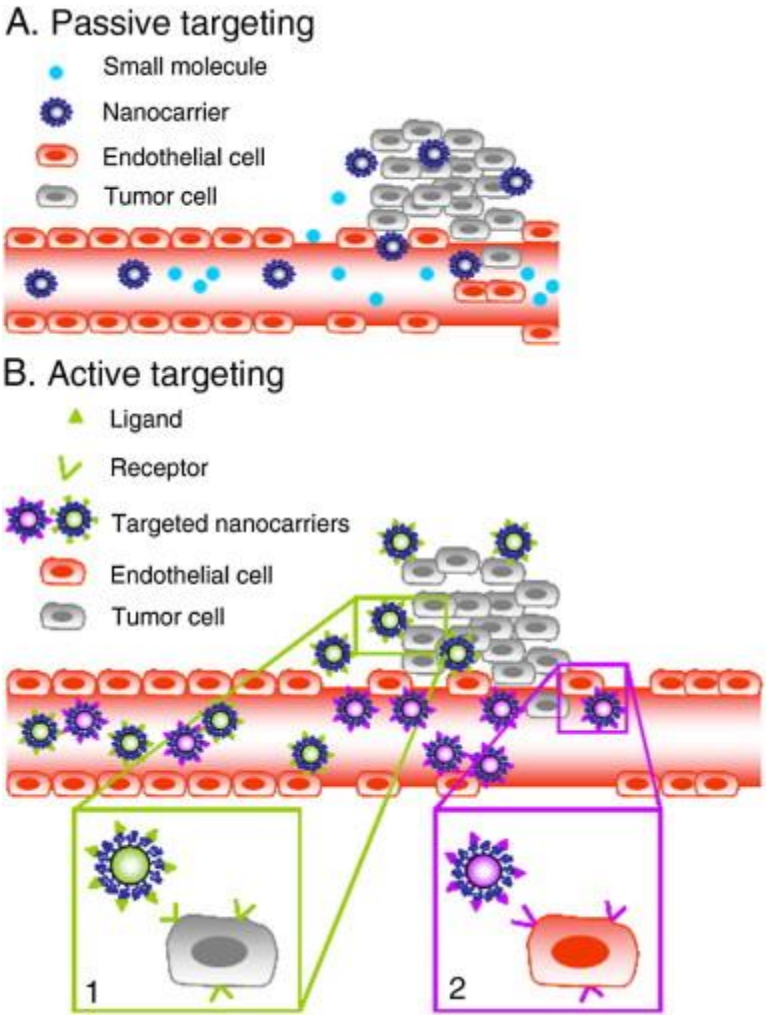

Figure 8 A. Passive targeting of nanocarriers. (1) Nanocarriers reach tumors selectively through the leaky vasculature surrounding the tumors. (2) Schematic representation of the influence of the size for retention in the tumor tissue. Drugs alone diffuse freely in and out the tumor blood vessels because of their small size and thus their effective concentrations in the tumor decrease rapidly. By contrast, drug-loaded nanocarriers cannot diffuse back into the blood stream because of their large size, resulting in progressive accumulation: the EPR effect. B. Active targeting strategies. Ligands grafted at the surface of nanocarriers bind to receptors (over)expressed by (1) cancer cells or (2) angiogenic endothelial cells [61].

As a result, appropriate biochemically targeted agents should be developed by considering some influential issues, such as suitable target affinity, high-specificity for a target, fast clearance of the unbound agent with respect to washout of the target bound agent, and high signal in the target bound form [9].

1.17.1 Trastuzumab

There is an upward trend in utilizing interacting molecular targeted agents with receptor tyrosine kinases on tumor cells in clinical oncology. The agents can be classified in two

categories: monoclonal antibodies and low-molecular-weight tyrosine kinase inhibitors. monoclonal antibodies like Cetuximab (chimeric mouse/human) and trastuzumab (humanized) target the extracellular domain of the receptors ErbB1 and ErbB2 respectively. Preventing receptor phosphorylation and activation of the kinase domain and subsequently inhibiting cell proliferation is done by Binding of trastuzumab to ErbB2. It also decreases shedding of the extracellular domain of ErbB2 together with preventing the production of an active truncated fragment. The therapeutic activity against breast cancer of this agent is proven and has been rewarding in usage in clinical applications [63].

1.17.2 Biotin

A growth promoter of cells can be Biotin, a member of the vitamin family (vitamin H). cancerous tumors have a considerably higher content of Biotin compared to normal tissue [64].

Sodium dependent multivitamin is the compound in which the main transporter for biotin), which has been found to be overexpressed in several aggressive cancer lines such as leukemia (L1210FR), ovarian (OV 2008, ID8), colon (Colo-26), mastocytoma (P815), lung (M109), renal (RENCA, RD0995), and breast (4T1, JC, MMT06056) cancer cell lines.

The overexpression of it was reported to be higher than the folate receptor. This can be explained by considering biotin pertains to a specific class of (exogenous) micronutrients required for cellular functions and , specially for cell growth. For this, in tumors and moreover, in the rapid growing tumors, the biotin demand is higher than normal tissues.[65].

1.18 Toxicity

With respect to the application of nanomaterials in the wide range from electronics to photonics, chemistry, and biomedicine, improving our understanding of the potential human health risks of nanomaterial, is unavoidable and it is important factors in order to develop nanoparticle-mediated therapy. There are various physical and chemical parameters, including nanoparticle morphology, composition, surface functionality and charge, metabolic byproducts, and colloidal stability, as well as clinical factors, including dosage and treatment regimen, profoundly affect the acute toxicity. To assessing the cytotoxicity of nanoparticles, the most frequently used *in vitro* cell-based assays are currently the most commonly used approach. They benefit from relative simplicity, sensitivity, and cost-effectiveness compared to animal testing. There has been a growing number of reports illustrating methods for measuring the cytotoxicity of nanoparticles. An approach for evaluating the cytotoxicity is cell viability assays, which quantify live versus dead cells in a sample and estimate the cellular responses to nanoparticles. Most such cell viability assays involve monitoring and quantifying differential metabolism of added dye molecules, including trypan blue, Coomassie blue, 3-(4,5-cimethylthiazol-2-yl)-2,5-diphenyl tetrazolium bromide (MTT), 3-(4,5-dimethylthiazol-2-yl)-5-(3-carboxymethoxyphenyl)-2-(4-sulfophenyl)-2H-tetrazolium (MTS), or endogenous enzymatic activity, such as lactate dehydrogenase, by living versus dead cells [57, 45].

Contrary to cadmium-based quantum dots and other immunogenic or toxic nanoparticles, gold colloids have had little or no long-term toxicity; as well as other adverse effects *in vivo* proving their usefulness for nanomedicine applications [67]. However, CTAX functionalized gold nanoconjugates were initially seemed to be toxic, washing them to remove excess ligand subsequently demonstrated no cytotoxicity. Additionally, it was also surveyed how to reduce the ligand toxicity, e.g. CTAB, by complexation with an

AuNP. Noteworthy, the substitution of CTAB surface groups with PEG, causes very few particles to be retained in the liver after 72 h clearing most of which [68].

On the other hand, GBCA in MRI, has been approved for human use for 18 years ago as one of the safest pharmaceuticals. Immediate adverse event rates are usually mild and very low (about <1 per thousand injections) with the occurrence of severe adverse events about once per 40000 injections [9].

Thereupon the potential applications of gold nanoparticles in various fields of nanomedicine, it is imperative that we improve our understanding of their toxic effects on mammalian cells.

1.18.1 MTT

A popular tool to assay the metabolic activity of living cells is The MTT (3-(4,5-dimethylthiazol-2-yl)-2,5-diphenyltetrazolium bromide) tetrazolium test, that is based on enzymatic reduction of the lightly colored tetrazolium salt to its formazan of intense purple-blue color. This can be quantified by spectrophotometry methods. The ratio of the obtained absorbance from this test can have a good correlation with the number of living cells if the test conditions are proper and optimized.

There is proportionality between the amount of the formazan crystals and the metabolic activity and the crystals are produced by mitochondrial enzyme succinate dehydrogenase which is produced by live cells.

There's proof that the amount of formazan produced by the cells is independent from whether they are with poisoned mitochondria or with the normal mitochondria.

The advantages are : possibility of decreasing the time of access to the samples and accessing to multiple and large number of samples at the same time. The results could be acquired objectively and in a semi-automatic way using an instrument, the boosted reproducibility, decreased required number of cells, assessing the cells growth rate will

become possible, either using it on several types of the cell cultures (monolayer cells, spheroids, and colonies), and low cost [69].

Chapter 2

Synthesis and Characterization

2.1 Materials and Instruments:

All reagents and solvents were purchased from Sigma-Aldrich unless otherwise noted. Nanoparticle characterization was performed on 120 keV TEM (Jeol 1010, Tokyo, Japan).UV/vis/NIR spectra of colloidal solutions were collected on a UV/VIS spectrophotometer Jenway 6715 (Montepaone, San Mauro Torinese, Italy). The mean diameter and surface charge of the NPs were assessed with a Zetasizer NanoZS (Malvern instruments ltd, Malvern, UK) operating at a light source wavelength of 633 nm. Nanoparticles concentration was provided by NanoSight (NS300,Malvern). ICP-MS was performed on inductively coupled plasma mass spectrometry (ICPMS) (Element-2; Thermo-Finnigan, Rodano (MI), Italy). Sample digestion was performed with 20 ul of sample and 180ul of concentrated HNO3 (70%) plus 200ul MilliQ water, under microwave heating (Milestone MicroSYNTH Microwave Labstation). Analytical high-performance liquid chromatography-mass spectrometry was performed on a Waters Fraction Lynx auto-purification system equipped with micromass ZQ ESI(+) ionization mode and dual-γ detectors, using ACQUITY UPLC BEH C18 column 1.7 um and H_2O/0.1% TFA and CH_3CN/0.1% TFA as eluents. The purification of gadolinium complex was done by preparative HPLC using a Waters Atlantis RPdC18 19/100 column (Waters, Milford, Massachusetts, USA).

2.2 Synthesis of Gadolinium Complex

DOTA (1,4,7,10-tetraaza cyclododecane-1,4,7,10-tetraacetic acid) chelate was chosen for conjugating to PEG; Because high thermodynamic stability and kinetically inert property is appeared when Gd(III) bound to DOTA-like ligands. In this respect, the neutral Gd(III) complex facilitates the cellular uptake [70]. The ligand 2 provides a coordination

environment, including one amide O donor atom, three carboxylate O donor atoms and four macrocyclic N donor atoms, typically by the DOTA- and DO3A bioconjugation.

DOTAMA($tBuO)_3$-C_6-OH which was synthesized according to a previously reported procedure , Hexafluorophosphate Benzotriazole Tetramethyl Uronium (HBTU), 1-Hydroxybenzotriazole hydrate ($HOBt.H_2O$) and N,N-Diisopropylethylamine (DIPEA) were dissolved in CH_3CN the mixture was allowed for 15 min and then react with Boc-PEG2-Amine for 2 h under gentle stirring (Fig. 9-1). The solvent was evaporated to give a yellow solid. The solid was purified with Silica Gel chromatography column and using the eluent 9:1 dichloromethane: methanol. The fractions containing the desired product were collected and combined, and the solvent was evaporeted to give a white solid (0,1 g, yield 78%). For simultaneously removing the tert-butyl ester groups and -Boc, product was reacted with trifluoroacetic acid (TFA) and Triisopropyl silane (TIS) overnight (5 mL, 95:5) (Fig. 9-2). The product was precipitated by adding diethyl ether and kept at 4°C for 2 hours to complete the precipitation. The precipitate was filtered and washed with ether and dried in vacuo. Then, to attach a thiol group on the ligand, SATA reagent (N-succinimidyl S-acetylthioacetate, 1,5 equivalent) was added to deprotected DOTAMA-C6-PEG_2-NH_2 in a mixture of buffer phosphate 50 mM pH 7.4 and acetonitrile (1:1) (Fig. 9-3). The crude product was purified by preparative HPLC. MS by using a Waters Atlantis RPdC18 19/100 column using H_2O-TFA 0,1% (A) and CH_3CN (B) as eluents. elution initial condition 5% B, linear gradient 5−10% B over 6 min, 10−30% B over 12 min, flow rate 20 mL/min, and UV detection at 220 nm. Lyophilization yielded a white powder (0,050g, yield 60%). Analytical UPLC was carried out using an ACQUITY UPLC BEH C18 column and 0.05% TFA in water (solvent A) and 0.01% TFA in acetonitrile (solvent B), elution initial condition 5% B, linear gradient 5−30% B over 6 min, 30−100% B over 12 min, flow rate 0,4 mL/min, and UV detection at 220 nm (t_R = 3.77 min). The UPLC chromatogram (Fig.

10) shows a degree of purity of 96.4% and mass spectrometry of its main peak in ESI (+) (Fig. 11) indicates a molecular mass of 763.5 g.mol^{-1}, in agreement with the theoretical molecular weight for $C_{32}H_{57}N_7O_{12}S$ of 763. 4 g mol^{-1} (m/z: found 764.5 [M + H]+, 786.5 [M + Na]+, 382.8 [M+2H]2+).

Gd(III) complex was synthesized in water by stoichiometric additions of $GdCl_3$ at pH 6.5 (Fig. 9-4). The occurrence of residual Gd^{3+} free ion was assessed by UV-vis spectroscopy using the xylenol orange. Complex was shown to contain less than 0.3% (mol/mol) of residual free Gd3+ ion. The characterization and the purify of complex were evaluated by UPLC-MS(ESI+) and by relaxometric analysis. MS (ESI+): m/z: calcd for $C_{32}H_{54}GdN_7O_{12}S$ [M+H]+: 919.3, found: 919.4; [M+2H]2+: 460.1, found : 460.0 (Fig. 12). At the final step 2 mL of 1.0 M Hydroxylamine and 50 mM EDTA were added to 1 mL of the complex (0,040 g, 40mM) in water to remove the acetyl group (Fig. 9-5). The purification step was carried out through gel filtration using a sephadex G25 column. The recovered Gadolinium complex (Gd-DOTAMA-thiol, compound 6) containing fraction was lyophilized and stored in the freezer before being used for the functionalization of nanoparticles (Fig. 9-6). MS (ESI+): m/z: calcd for $C_{30}H_{52}GdN_7O_{11}S$ [M+H]+: 877.3, found: 877.3; [M+Na]+: 899.3, found: 899.3; [M+2H]2+: 439.1, found : 439.0 (Fig. 13).

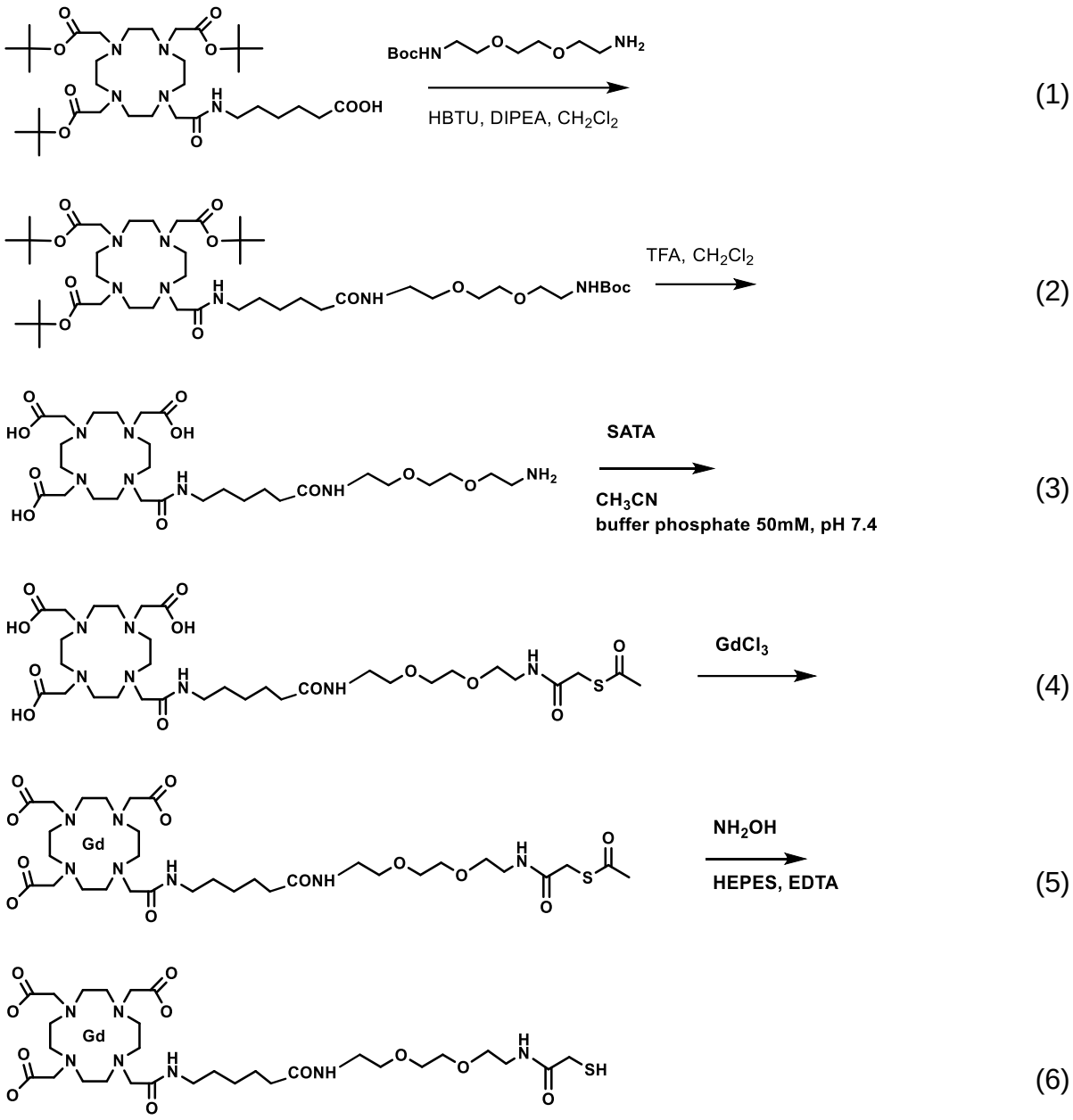

Figure 9 Chemical synthesis of Gd (III) complex 6.

2.2.1 Characterization of Gadolinium Complex

The formation and purity of final product was evaluated by mass spectrometry (Fig.13) and analytical UPLC (estimated at λ = 220 nm) using an Acquity UPLC peptide BEH dC18 column 1.7 μm, 2.1 mm ×100 mm (flow rate: 0.4 mL/min) (Fig. 14). The purity of the gadolinium complex was calculated about 96%.

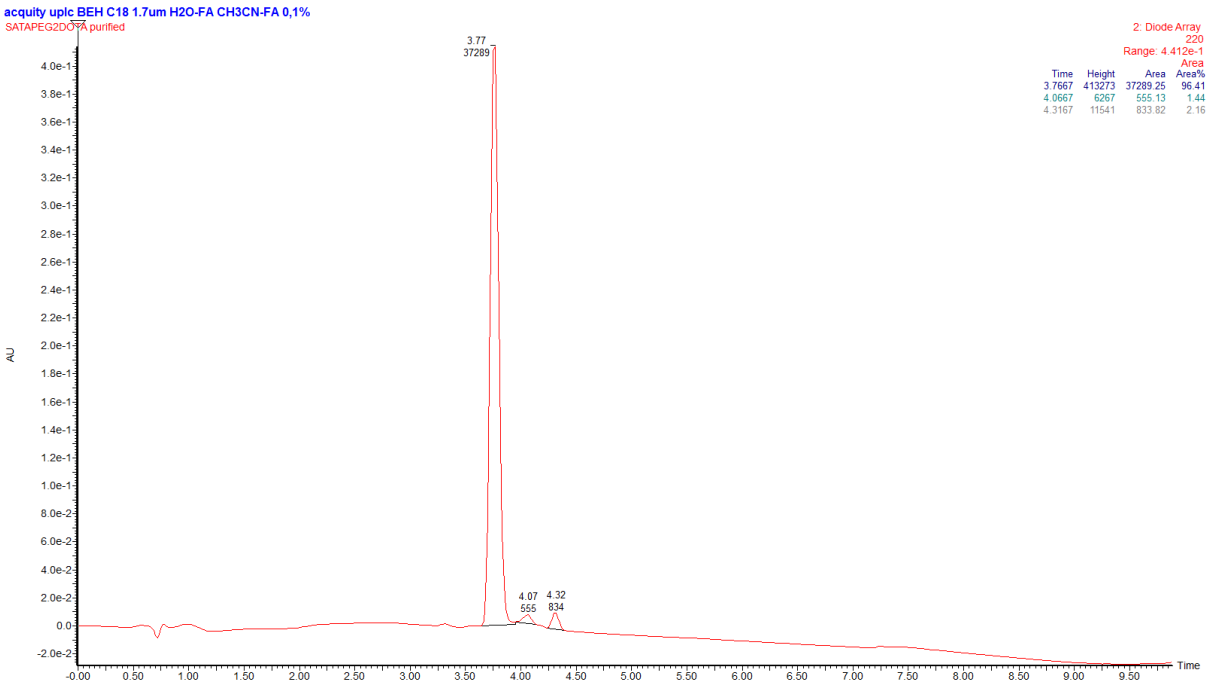

Figure 10 Chromatogram UPLC-UV of compound 4.

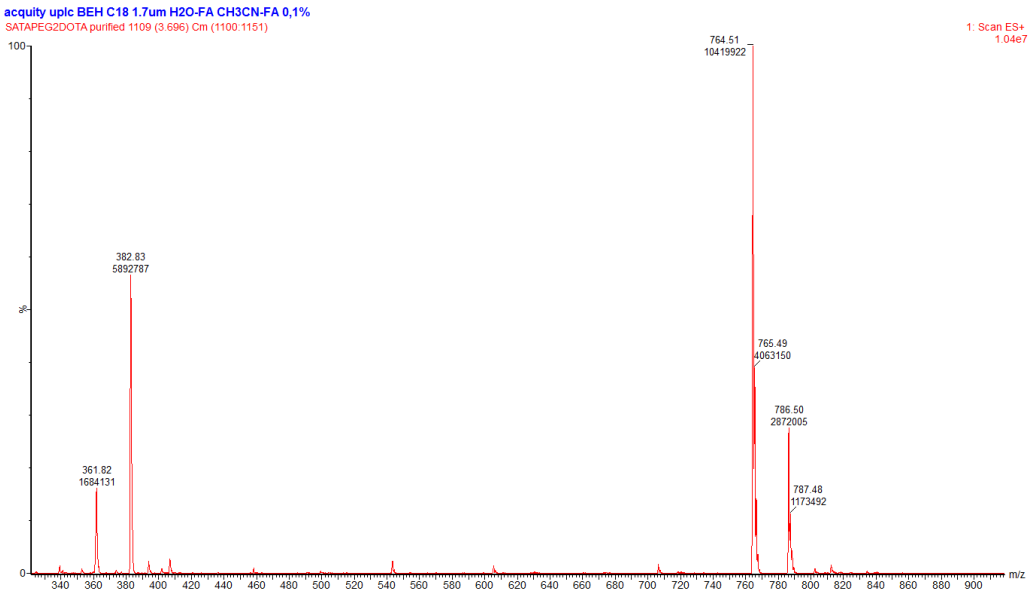

Figure 11 ESI (+) mass spectrum of peak at 3.77 min (compound 4).

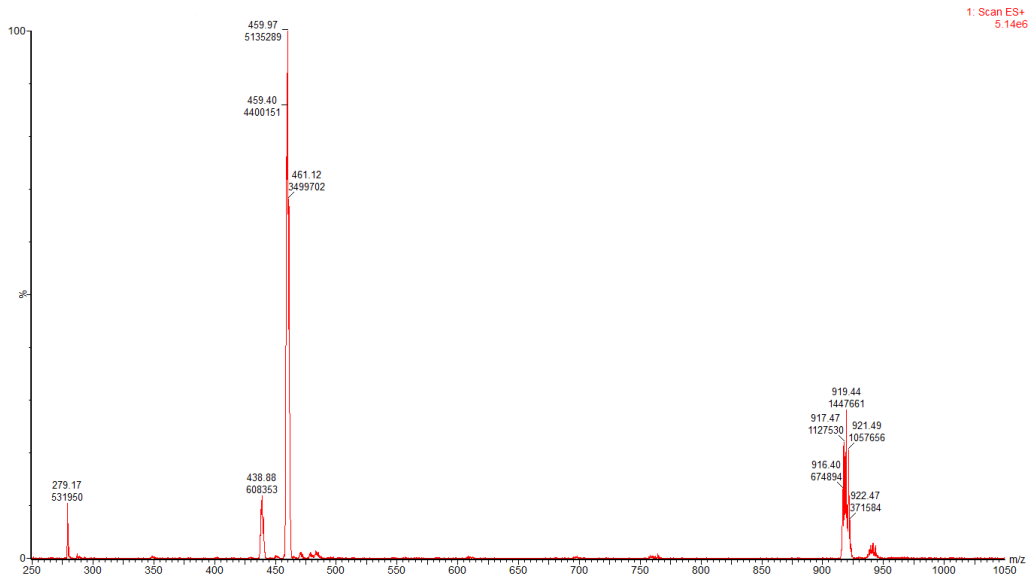

Figure 13 ESI (+) mass spectrum of compound 5.

Figure 12 ESI-Mass spectrum of Gd(III) complex 6. Calculated m/z for $C_{30}H_{52}GdN_7O_{11}S$ =877.3, found m/z for $C_{30}H_{52}GdN_7O_{11}S$ = 877.4 $(M+H)^+$, 439.1 $(M+2H)^{2+}$

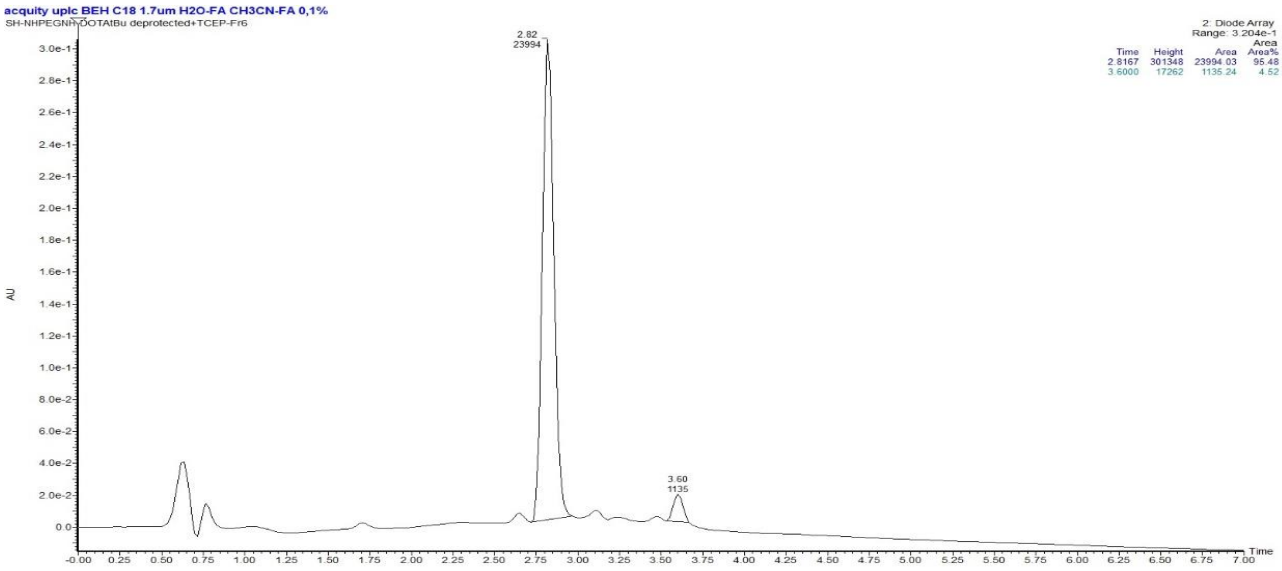

Figure 14 UPLC chromatogram of Gd (III) complex 6.

Time	A%	B%
Initial	95	5
0.56	95	5
6	70	30
12	0	100

Table 1 Ultra performance liquid chromatography (UPLC) conditions of Gd (III) complex 6 With Eluents: A:water+0.05% TFA, B:ACN+0.05% TFA

The relaxivities (the proton relaxation enhancement of water protons in the presence of the paramagnetic complex at 1 mM) of Gd complex was measured at 21.5 MHz and 298 K and it was 5.58mM^{-1} s^{-1}.

2.3 Synthesis of Concave Cube Gold Nanoparticles

The next step dealt with the fabrication of the concave cube gold nanoparticles by following the work of Personick et al [71]. We slightly customized the original procedure to obtain desired size of nanoparticles.

The first step is fabricating the seed particles which is largely unique for all reported seed-mediated syntheses. Tetrachloroauric acid ($HAuCl_4$) is reduced by using a strong reducing agent, often sodium borohydride ($NaBH_4$), to synthesize seed particles; this process is done by using the stabilizing agent, usually the surfactant cetyltrimethylammonium bromide, as well as cetylrimethylammonium chloride and sodium citrate. In this regard, the strong reducing agent ensures the formation of small and monodisperse particles; because of the simultaneous fast nucleation of an abundant of nanoparticles into the solution. The resulting seeds are typically about 3−7 nm. Au nanoparticles seed-mediated syntheses have characteristically high degrees of shape control and appropriation that are primarily achieved during the second growth step. The second step involves the addition of seed particles to the reaction solution, namely the growth solution as reported in the nanoparticle synthesis literature; which contains at least a source of gold ions, a surfactant and a weak reducing agent. Additional nucleation is prevented in the growth step via a weak reducing agent, which also favors the growth onto the preformed seeds and on the other hand, slows particle growth rate which is suitable for shape control through adding shape-directing additives. The reducing agent would be commonly ascorbic acid as being weaker than $NaBH_4$. AA has an easily tunable reducing ability implementing by adjusting the solution pH; which has been decreasing at lower pH values. Generally, ascorbic acid has rapidly reduced Au^{3+} to Au^{+}; but the subsequent reduction of Au^{+} to Au^{0} is very slow at low pH and also is negligible lacking seed particles served to catalyze the reduction step. The use of $NaBH_4$ as the reducing agent forms additional small Au nuclei in this step, rather than performing the favorable growth of larger nanoparticles with anisotropic shapes. The shape-directing additives are also used to achieve versatile shapes in the seed-mediated approach, mostly including Ag ions and halide ions [50].

Briefly, Au seeds were prepared by quickly injecting 0.60 mL of ice-cold, freshly prepared NaBH4 (10 mM) into a rapidly stirring solution containing 0.25 mL of HAuCl4 (10 mM) and 10.00 mL of CTAC (100 mM). The seed solution was stirred for 1 minute and then left undisturbed for 2 hours.

A growth solution was prepared by consecutively adding 0.50 mL of HAuCl4 (10 mM), 100 µL of AgNO3 (10 mM), 0.20 mL of HCl (1.0 M), then 0.10 mL of AA (100 mM) into 10.00 mL of 0.1 M CTAC. The seed particles were serially diluted in 0.1 M CTAC to generate a solution which was 1/80 the concentration of the original seed solution. Particle growth was initiated by adding 0.1 mL of the diluted seeds to the growth solution. The reaction was swirled immediately after the addition of the seeds and then left undisturbed on the bench top until the reaction was complete.

The overgrowth of the bare CCGNPs with thin gold films has done by 15 mM gold salt solution. In this regard, AA reduced the gold in the absence of silver nitrate. The blue-shifted longitudinal plasmon band was also observed for the overgrowth from about 650 nm for the untreated CCGNPs to approximately 630 nm for particles with the thin gold film (8 uM HAuCl4 during the growth) (Fig. 26). The washing step of bare CCGNPs was done by adding 78ml of MilliQ water to the solution by following centrifuge it. After removing the supernant, the particles were suspended in the 132.3ml of CTAC 10mM. the solution was mixed with 219ul of Au and 2.7 ml of AA (100mM) for one hour. When the overgrowthing completed, 7.7 ml of pure CTAC was added to the solution. The final CCGNPs was kept at 4˚C for functionalization step.

Therefore, overgrown gold covers silver species instead of removing them from the particle surface. Indeed, upon adding the thin layer of gold, the average hydrodynamic diameter of nano concave cube increased slightly (Fig. 20).

2.4 Functionalization of Concave Cube Gold Nanoparticles

Functionalization has not been associated with irreversible particle aggregation or surface reorganization effects. The bond strength of an Au-thiol dative bonding has been reported to be within the range of 40-50 kcal/mol close to Au-Au bond strengths. Typically, the ligand exchange occurs on planar surfaces in two steps: firstly, the rapid Langmuir adsorption step dependent upon concentration and diffusion, and the second slower and almost unpredictable step depending on the chain disorder, inter-chain interactions and surface mobility of ligands [16].

The functionalization of Au NPs was conducted with Raman dyes or Gd complex for SERS nanoparticles and MRI contrast agent respectively. The aqueous reporter (MGITC or Gd complex) solutions was added to the Au colloid; while it is undergoing a sturdy stirring. The reporter solutions were necessarily added in droplets to avoid aggregation of particles, caused by imminent variation in their surface charges in the absence of high molecular weight that coats the ligands like PEG or lipids, that could decrease the aggregation via steric repulsion.

In order to avoid non-specific association of particles with surfaces or solution species and their stabilization which prevent the particles aggregation upon subjection to buffer salts, as well as maintaining fidelity of their SERS or MR activity by decreasing any dissociation of reporter molecules from the Au surface, heterobifunctional polyethylene glycol (PEG) was used to coat nanoparticles' surface. Ligand exchange was used by which, CTAC capped particles were suspended in aqueous solutions of PEG-SH present in molar excess to coat the particles with thiolated PEG. Exchanging the weakly associated CTAC with PEG creates a stable gold-thiol dative bonds on the Au surface. The aforementioned dative bonds of Au-thiol have reportedly a strength of 40-50 kcal/mol which is quite close to Au-Au bond strengths [16].

For MR active nanoparticles, after adding Gd complex, two types of 2 kDa molecular weight thiolated PEG molecules were used for NP coating: one with a methoxy group on the distal end of the PEG for making the particle surface passive (1.45 ml,10uM) and the other one with a biotin group to facilate conjugation to target proteins (29.4 ul, 10uM) (Fig.15).

In the SERS nanoparticles preparation, 4ml of nanoparticles were centrifugated and redispersed in 2 ml of MilliQ water. After functionalization the nanoparticles with MGITC (202 ul, 23.64 uM), in next step the NH2-PEG-SH (215 uL, 15.76mM) was added and 10 minutes were allowed for the reaction to proceed further. Poly(ethylene glycol)-thiol (OMe-PEG-SH, MW=2000) was used to backfill the remaining area on the gold nanoparticles surface (1.6 ml,630 uM) (Fig. 15).

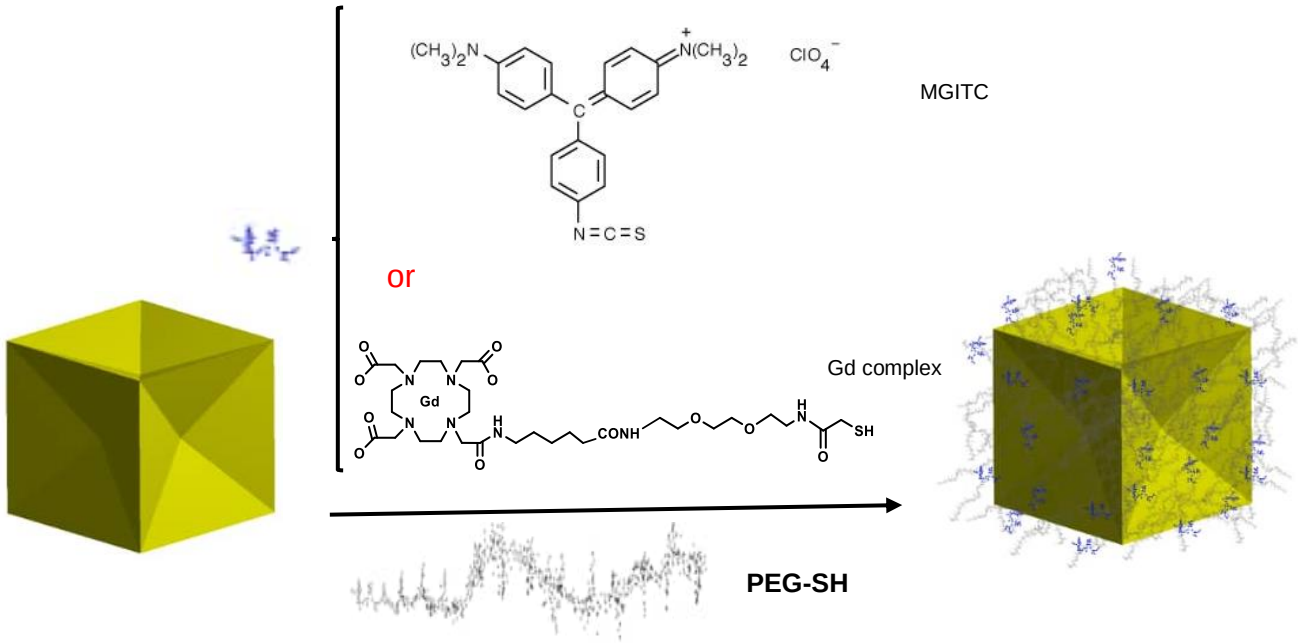

Figure 15 Preparation of PEG-Gd/MGITC @CCGNPs

2.4.1.1Bioconjugation of Targeting Antibodies to SERS Nanoparticles

Conjugation of nanoparticles to targeting proteins can be accomplished by carboxyl to amine conjugation chemistry. In the first step, for tracking the conjugated nanoparticles; also quantify the antibody (Trastuzumab), the labeling antibodies with Alexa Fluor™ 488 5-TFP was done. Tetrafluorophenyl (TFP) esters are an improvement over the succinimidyl ester (SE or NHS-ester) chemistry typically used to attach fluorophores or haptens to the primary amines of biomolecules (Fig. 16-2). In the sodium borate buffer (SBB) with pH=8.3 and 30 mM concentration, 2 ug of fluorophore was added to 3mg of antibody (Ab) which is was dialyzed formerly (Fig.16-1). The reaction was left over night at 4˚C and dark place. The next day, the Zeba spin desalting column primarily was washed with PBS solution (pH=7.2, 20 mM) three times and it was used for purifying the labeled antibodies. The concentration of Ab in the solution was found by using the UV-Vis spectroscopy.

The conjugation of antibodies with nanoparticles was possible through reductive amination. The 5 mg/ml solution of NaIO4 was adding to the 0.5 mg of antibody till reaching the final concentration 0.32mg/ml (1.5mM) (Fig. 17-1). 20 minutes later, the antibody solution was desalted by Zeba column (the Zeba column should be washed as it mentioned earlier). Purified antibodies were mixed with the PEGylated nanoparticles which have amine functional groups. The mixture was kept in room temperature for 2 hours in dark place. Since Sodium cyanoborohydride is unstable during the long time, the fresh solution $NaCNBH_3$ should be prepared in PBS buffer (5 M) just before reaction. It was stirred with nanoparticle mixture with the final concentration of 50 mM (3.14 mg/ml). the reaction was incubated overnight at 4˚C in dark place. The final conjugated SERS nanoparticles was cleaned from unreacted antibodies through precipitation in centrifuge (Fig 17-2).

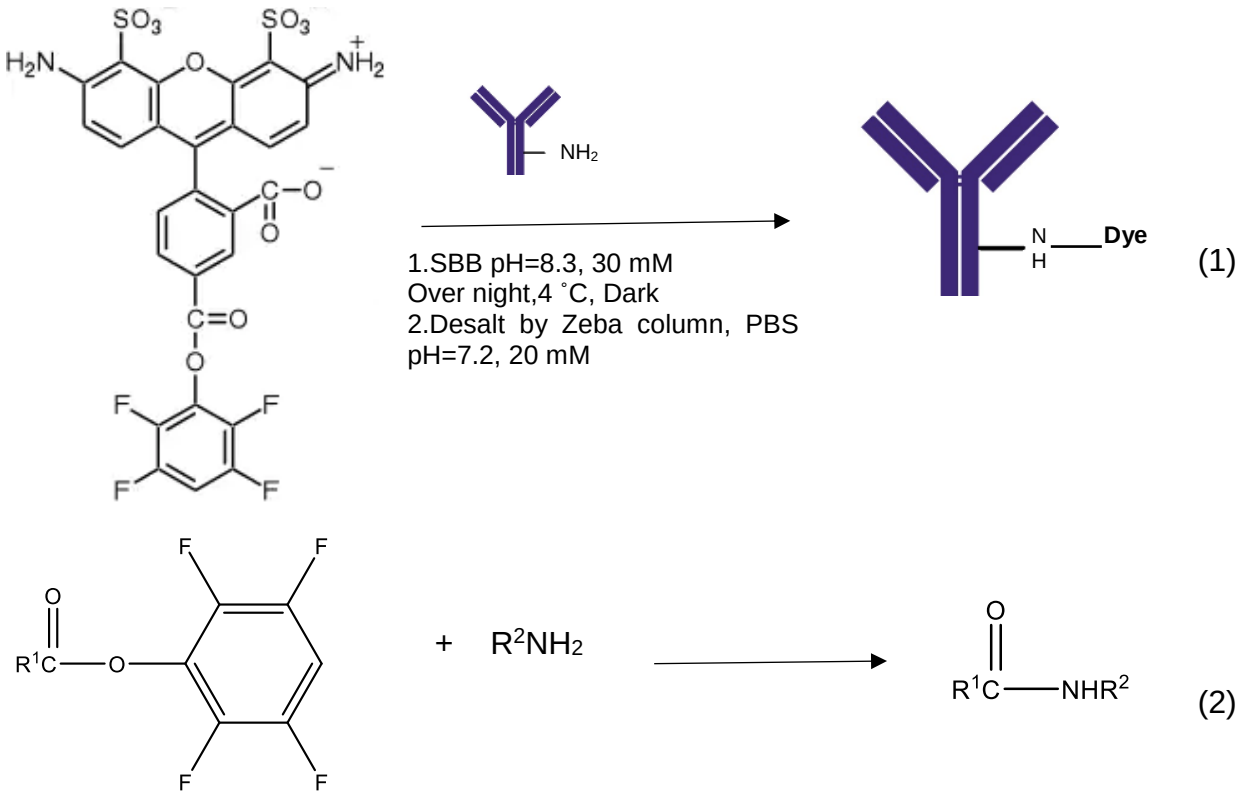

Figure 16 schematic reaction of laballing the antibodies

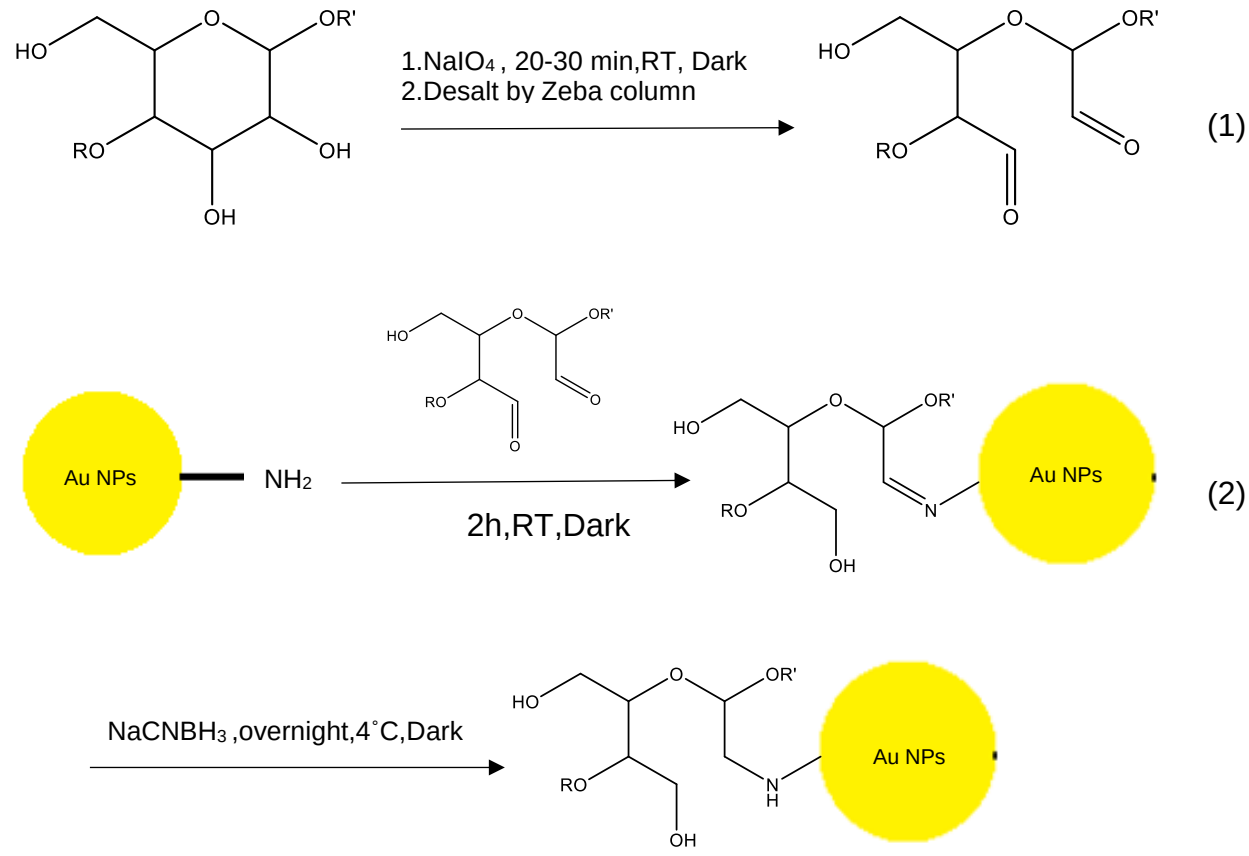

Figure 17 Schematic reaction of 1) internal Mannose oxidation 2) conjugation between nanoparticles and antibody

2.5Synthesis of Spherical Gold Nanoparticles

The spherical gold nanoparticles is synthesized by following the Zheng and colleagues work [72].

This synthesis relies on the use of single-crystal Au spheres as the seeds for successive growth and the use of a slow injection rate for the precursor to enable surface diffusion for the atoms added onto the surface of a seed. The basis of the synthesis is using single-crystal Au sphere to seed the successive growth and also to enable surface diffusion for the added atoms on the surface of the Au spheres a slow injection rate for the precursor is used.

By varying the size and /or number of the seeds, a precise control is possible for the diameters of spherical nano particles.

Preparation of the Initial, CTAB-Capped Au Clusters

Using pipette, a fresh aqueous $NaBH_4$ solution (10×10^{-3} M , 0.6 mL) was added to a completely mixed 10-mL aqueous solution containing $HAuCl_4$ (0.25×10^{-3} M) and CTAB (100×10^{-3} M) in a very short time. After adding $NaBH_4$, a brown solution was imminently formed. An orbital shaker working at the speed of 300 rpm was used to shake the mixture for a duration of 2 minutes and then kept in still conditions at 27°C for 3 hours, therefore the thorough decomposition of any residuals of $NaBH_4$ in the reaction mixture was ensured.

Standard Procedure for the Preparation of 10nm Au Nanospheres

Aqueous solutions of CTAC (200×10^{-3} M , 2 mL), AA (100×10^{-3} M , 1.5 mL), and the initial, CTAB-capped Au clusters (50ul) were mixed in a 20-mL glass vial, followed by one-shot injection of an aqueous HAuCl 4 solution (0.5×10^{-3} M , 2 mL). The reaction was set to run at 27 °C for 15 min. The Au nanospheres with a diameter of 10-nm were

dispersed in 1 mL of aqueous CTAC solution (20 ×10 $^{-3}$ M) after Centrifuging at 14 500 rpm lasting for 1 hour, which was used as seeds in the second round of growth.

Standard Procedure for the Preparation of 46nm Au Nanospheres

Aqueous solutions of CTAC (100 ×10 $^{-3}$ M , 2 mL), AA (10 ×10 $^{-3}$ M , 130 uL), and the 10-nm (10uL) seeds were mixed in a 20-mL glass vial, followed by dropwise addition of aqueous a syringe pump was used to inject HAuCl 4 solution (0.5 ×10 $^{-3}$ M , 2 mL) at a rate of 2 mL h−1. The reaction was allowed to proceed at 27 ˚C for 10 min after the injection had been finished. Centrifugation at 14500 rpm for 10 min was used to collect the final product and was washed with water once for characterization.

Two batches of 46 nm spherical gold nanoparticles were mixed together and the functionalization is done same as the MRI active CCGNPs.

2.5.1 Characterization of Nanoparticles

The determination of nanoparticles morphology and size were conducted by using UV-Visible spectroscopy and transmission electron microscopy (TEM). For CCGNPs and SPhNPs, the hydrodynamic diameter of nanoparticles was evaluated using dynamic light scattering (DLS) both after and before functionalization. Indeed, the concentration of nanoparticles solution was measured by Nanosight.

2.5.1.1 Electron Microscopy

Achievement of high-resolution imaging in electron microscopy requires irradiating samples with the accelerated electrons beam to take advantage of wave-like properties of electrons. The image contrast in bright-field TEM is created by the samples placed in the beam path via differential absorption or obstruction of the electron beam. The current is passed through a tungsten wire which is an electron source. Conduction electrons are also ejected from the gun material through thermionic emission. The electrons are

accelerated through the sample towards the detector by applying a voltage difference across the microscope. The image magnification can be achieved by changing the angle of focused beam possibly through increased voltage difference between the cathode and anode. The solenoids are used as electromagnetic lenses to guide and focus the beam. Operations on the vacuumed microscope and sample chamber have maximized the beam brightness, as well as reducing background scattering of entering TEM images; high energy electrons consequently move with the most possible mean free path. The detector can also be Charge Coupled Device or fluorescent screen [16].

Based on transmission electron micrographs (Figure 18), a mean tip-to-tip diameter of CCGNPs has been ca. 45 nm. Regarding the TEM grid, concave nanocubes having different orientations have exhibited different overall projection profiles and contrast evolution across the particle cross-sections in the TEM images. Au concave nanocubes are demonstrated to be highly monodisperse in terms of both particle size and morphology.

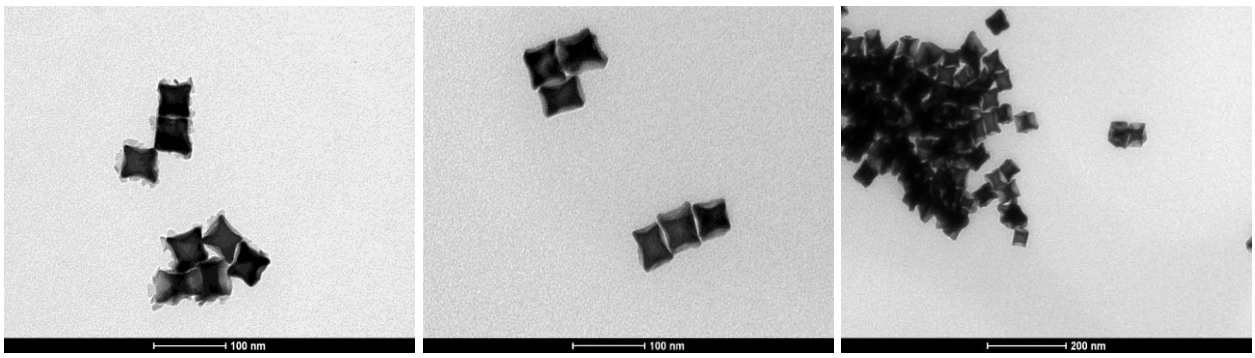

Figure 18 TEM images of concave cube gold nanoparticles

Characterization of hererogeneous materials and surface on a submicrometer scale becomes feasible also by using a powerful instrument called the scanning electron in which the irradiation of the area that is supposed to be examined is conducted by a highly focused electron beam. The primary signal of interest (which is the variation in secondary electron emission taking place as the electron beam) is swepts in a raster across the surface of spacimen thanks to topology variations in the surface. The enclosure of the

secondary electron yield near the beam impact area allows the images be obtained at relatively high resolution. Thanks to the high amount of focus depth in the scanning electron microscope, the images have a 3D appearance [73]; as SEM images of SPhGNPs (Fig. 19) demonstrate finly formed sphere nanoparticles .

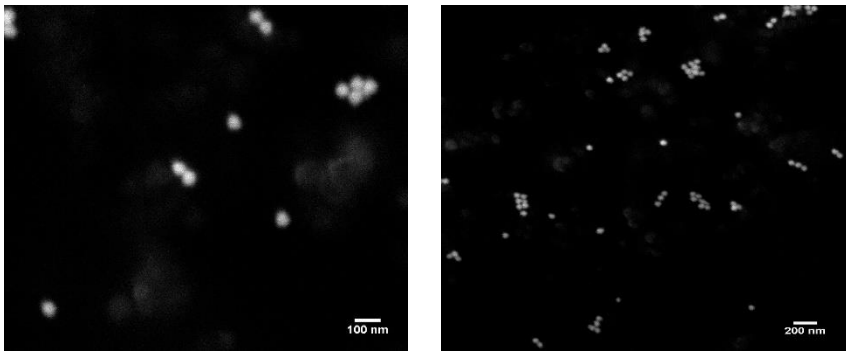

Figure 19 SEM images of spherical gold nanoparticles

2.5.1.2 Dynamic light scattering measurements:

Electron microscopy analysis requires dried nanoparticle specimens of Au nanoparticles since it does not inspect dimensions in the solution environment. Dynamic light scattering, known as quasi-elastic light scattering or photon correlation spectroscopy (PCS), is a sensitive technique suitably characterized dispersions for nanoparticles as well as nanoparticle-polymer hybrids. DLS analyzes changes the light diffraction pattern when a laser light passes through a micro- or nano-scale liquid suspension with particles undergoing Brownian motions. The combinational use of DLS and electron microscopy techniques fully provides a physical characterization of colloidal dispersions for Au nanoparticles used in biomedical applications. DLS evaluate the hydrodynamic diameter of Au NPs when change during functionalization experiments on the NP surfaces [31, 16].

Samples were prepared by dissolving nanoparticles in PBS, loading them in plastic cuvettes with a path length of 1 cm to be analyzed at pH 7.0–7.4 at 25 °C. The mean hydrodynamic diameter were then obtained.

CTAC-capped CCGNPs have specifically two narrow size distribution peaks; one for major particle sizes around 68-78 nm, and the other for small sizes around 13 nm (Fig. 20). The latter may be confusing if there are small particle impurities. Other anisotropic nanoparticles, e.g. AuNRs, have also similar two-peak size distribution. Based on recent studies, the small particle size distribution is not attributed to real particle size; but may represent the rotational diffusion of anisotropic nanoparticles. Thus, the rotational diffusion coefficient of CCGNPs is accordingly equal to the translation diffusion coefficient for spherical nanoparticles having mean diameters of 13 nm. As well, this small peak cause the wide distribution of normalized size for CTAC-capped NPs [28].

Upon functionalization with Gd(III)-PEG, the average hydrodynamic diameter of nano concave cube is slightly bigger than bare one (Fig. 21).

To give a boosted range of concentration and sensitivity to aggregates the zeta potential optics and NIBS (incorporating Non-Invasive Backscatter) are combined in order to provide the back and forward scattering angles for size measurement. Generally speaking , the larger the particles are, the more light in forward angles they scatter. This can be an indicator of presence of larger particles when analyzing the data. In terms of intensity, the average size in scattering forward is larger than the one in backward scattering.Therefore, to check the formation of aggregation after PEGylation step, the forward angle was used (Fig. 22). As it is clear in the particle size distribution graph, there was no evidence for aggregation and the graph just shows the size of the nanoparticles themselves.

As is evident in the figure 23, the funtionalizatin step of spherical nanoparticles was done successfully and the hydrodynamic size of particles shift to larger amount after functionalization.

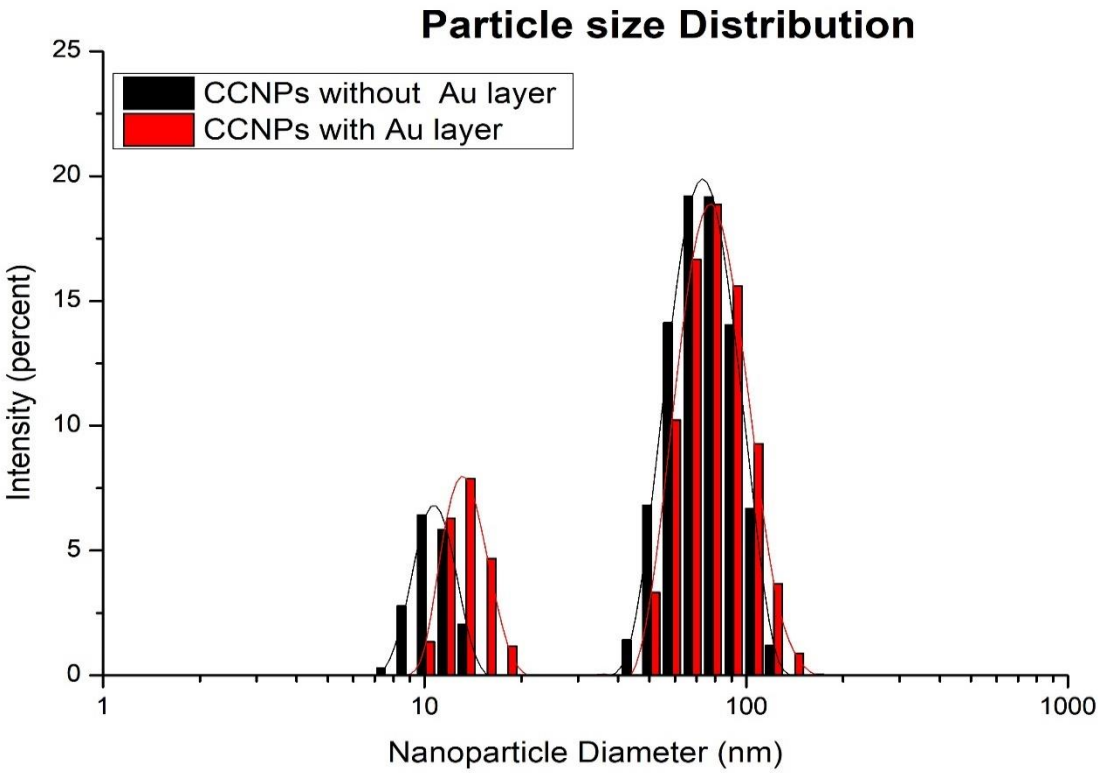

Figure 20 Particles size distribution for concave cube gold nanoparticles before and after Au growing layer

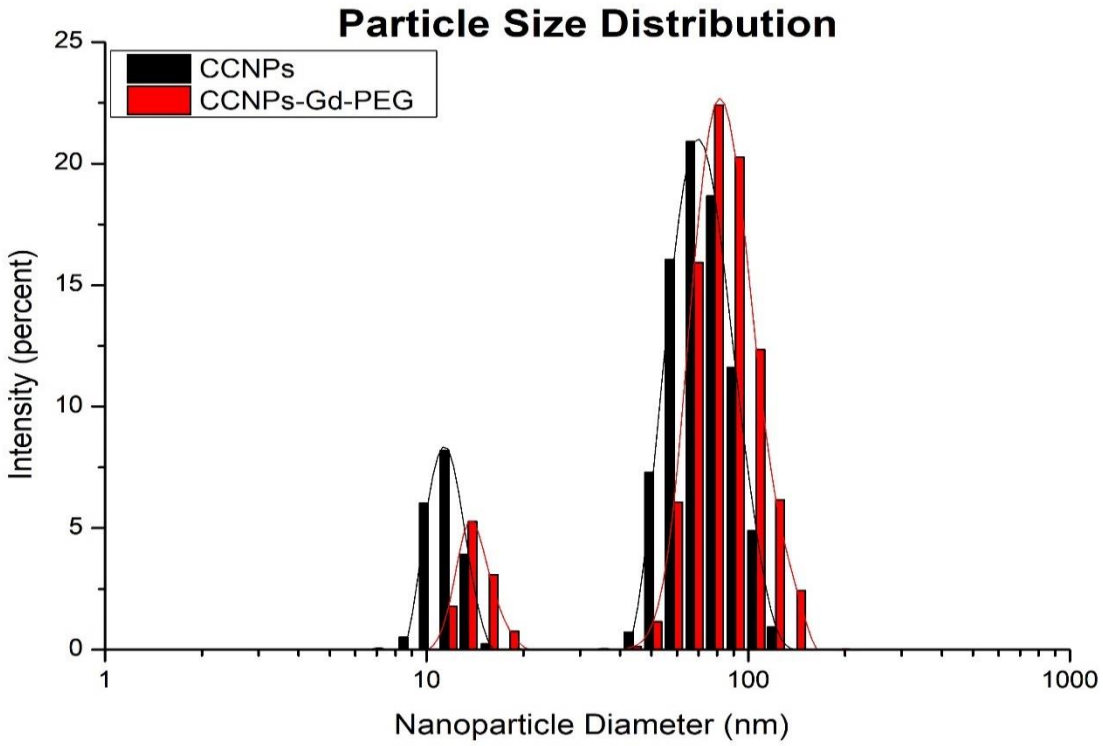

Figure 21 Particles size distribution (backward) for concave cube gold nanoparticles before and after PEGylation

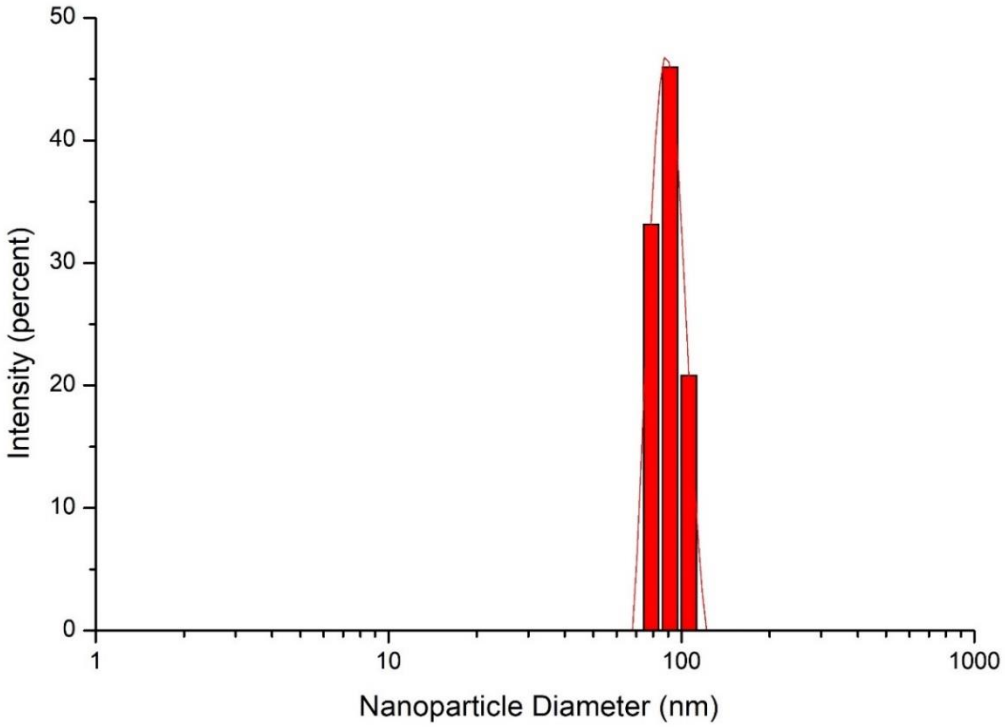

Figure 22 Particles size distribution (Forward) for concave cube gold nanoparticles after PEGylation.

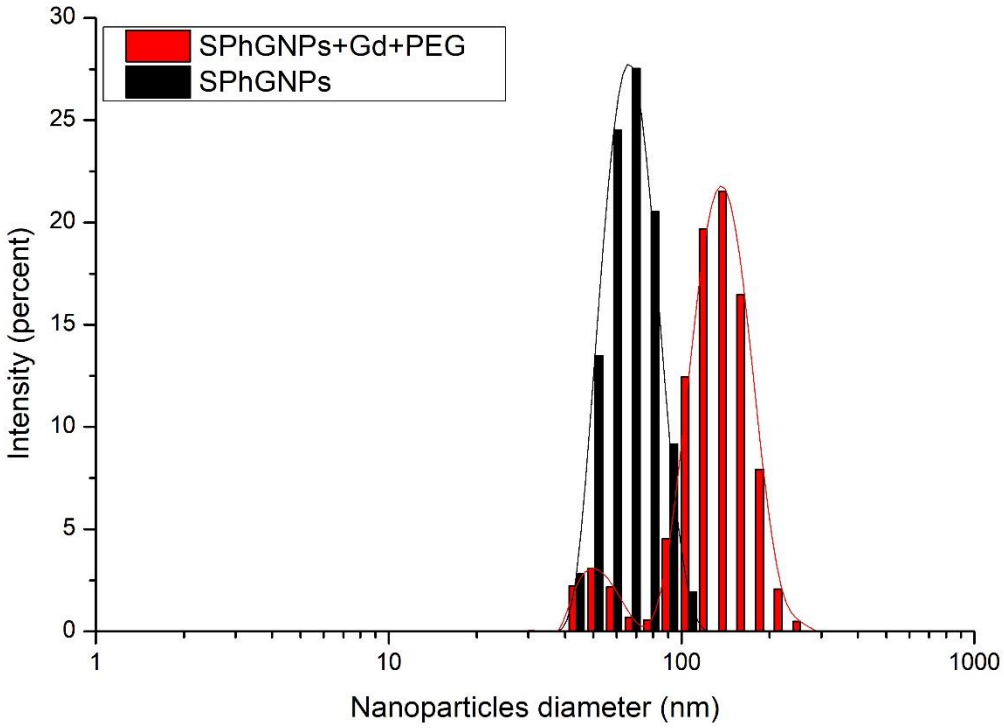

Figure 23 Particles size distribution of SPhGNPs before and after PEGylation

2.5.1.3Electrophoretic Light Scattering – Zeta Potential Measurement

Electrophoretic light scattering examines and analyzes the changes within the light interference pattern caused by travelling the laser light through a micro- or nano-scale liquid suspension with an electric field-induced movement in particles. The zeta potential is calculated for the particles using their velocity. The net charge at the surface of charged particles present in the suspension, determines the ion distribution in the interfacial region. Accordingly, an electrical double layer is formed around the particle with oppositely charged ions relative to the particle surface (Fig. 24). This electric double layer comprises the inner Stern layer consisting of ions that are chemically adsorbed onto the particle, besides the outer diffuse region, where ions are attracted to the surface charge and move along with the particle through the solution. The zeta potential is an electric potential existing across the slipping plane known as a boundary between the ions in the diffusion layer and surrounding suspension. The zeta potential is not evaluated by a direct charge measurement at the particle surface; mainly through considering the solvent and thus, ion concentration, used for measurements, as well as charges applied for the purpose of accelerating the particle [16].

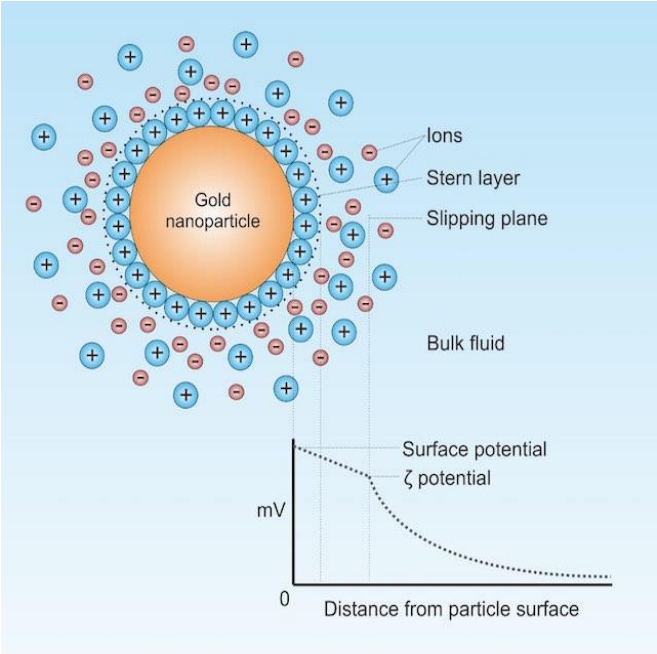

Figure 24 Diagram showing the ionic concentration and potential difference as a function of distance from the charged surface of a particle suspended in a dispersion medium.

The same sample which was used for DLS measurement, was benefited for z-potential measurement too. After functionalization with PEG, Z-potential has changed from +35.2 to -15.6 (Fig. 25-1) and from +17.5 to -17.4 for CCGNPs and SPhGNPs respectively; which is the proof for successful functionalization.

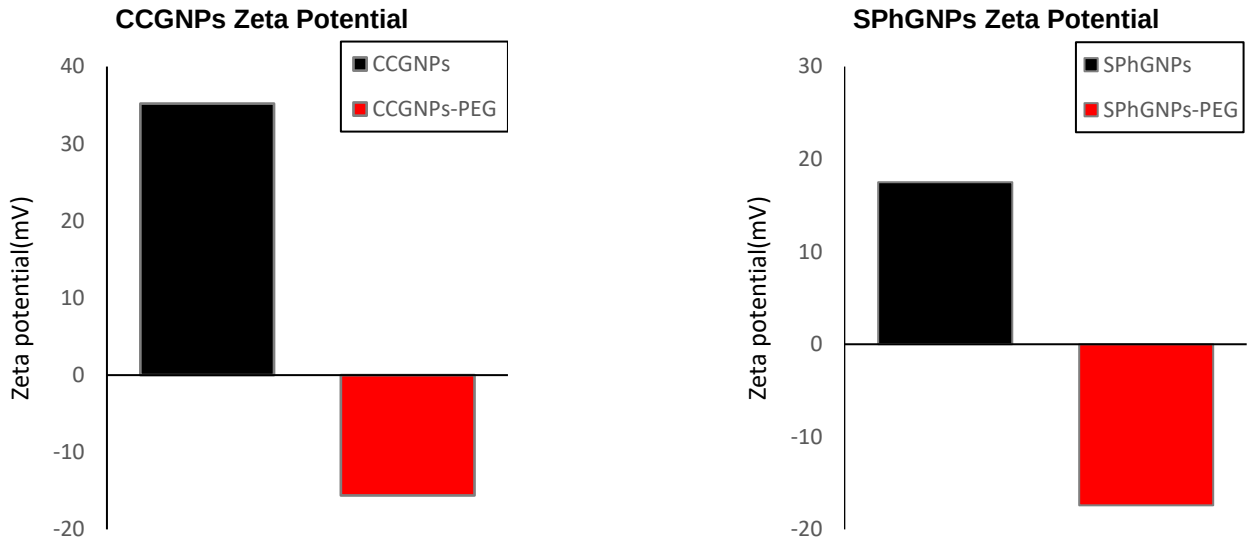

Figure 25 Zeta potential of the 1) Concave cube 2)Spherical gold nanoparticles before and after PEGylation.

2.5.1.4 UV-Vis spectroscopy

localized surface plasmon resonance is an optical attribute that gold nanoparticles manifest that occurs when there is resonance between a collective oscillation of electrons in the conduction bandwidth of gold nanoparticles with a certain wavelength of an incident light. The gold nanoparticles LSPR feature leads to a resilient absorption band in the visible region, that is possible to measure using UV-Vis spectroscopy. The spectrum of LSPR depends on two parameters of size and shape of the nanoparticles. The concentration of nanoparticles in solution can be linearly correlated to the peak optical density (OD), which is known also as absorbance of the sample. A 1 cm-path-length cuvette was used for obtaining absorbance spectra of stock Au particles considering 18.2 MΩ·cm water as a reference. Figure 27 presents the UV-vis extinction spectra of Au nanospheres with 46 nm diameters which proves the complete formation of SPhNPs.

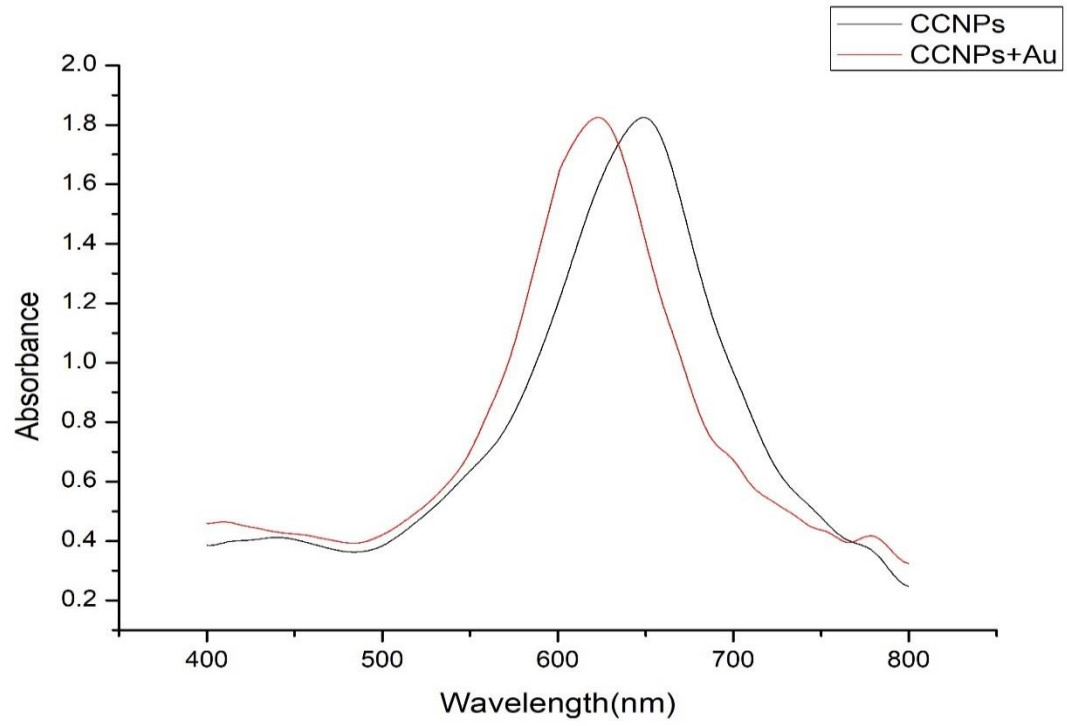

Figure 26 UV-vis spectra of Concave cube gold nanoparticles before and after Au growing layer.

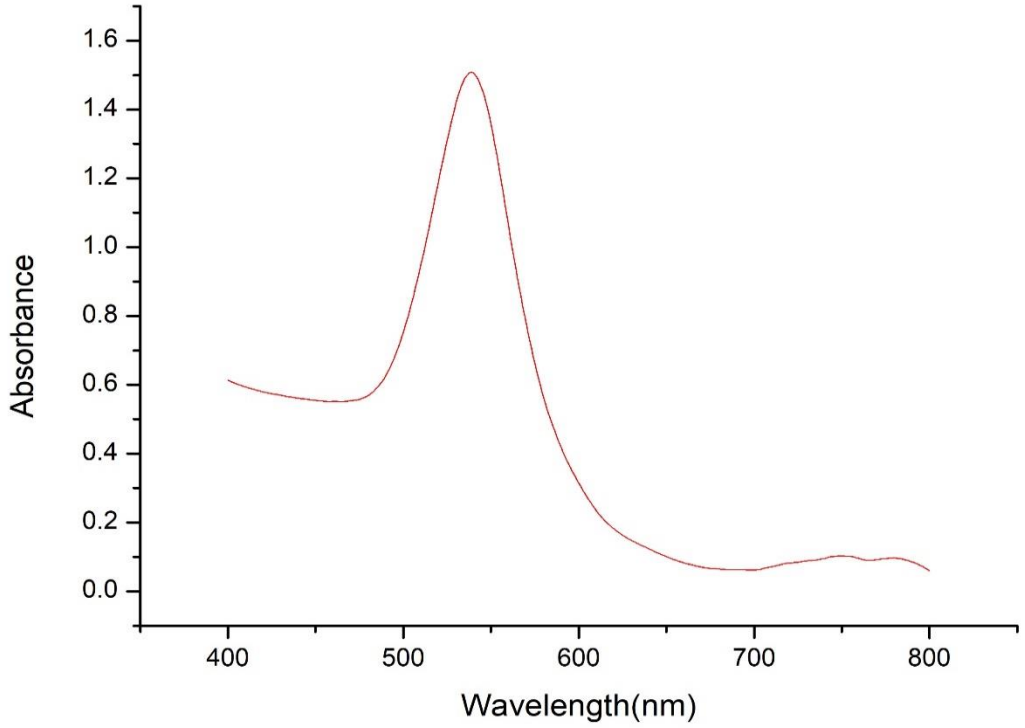

Figure 27 UV-vis spectra of 46-nm Spherical nanoparticles

2.5.1.5 Nanosight

To obtain the nanoparticle size distribution and concentration of samples in a liquid suspension, Nanoparticle Tracking Analysis (NTA) is used that utilizes the properties of both light scattering and Brownian motion. A special laser beam is used to illuminate the loaded liquid suspension in the sample chamber. A 20x microscope collects the light scattered by the particles obstacling the laser beam path and is viewed with a digital camera. The digital camera captures the particle' Brownian movement in a video file. The hydrodynamic diameter of particles is calculated by Stokes Einstein equation done in NTA software by analyzing many particles one by one at the same time. Measuring and counting of nanoparticles becomes feasible by Nano-Sight instruments that give a sufficient resolution in nano scale to view the particles conveniently. Collection of delicate changes of particle characteristics together with visual inspection can confirm and validate the analyses conducted. The concentration of synthesized CCGNPs and SPhNPs in the solution was obtained by NTA which was calculated the $2.77e^{+011}$ +/- $1.59e^{+010}$ and $4.39e^{+011}$ +/- $6.2e^{+09}$ particles per 1 milliliter of solution respectively. (Fig. 28 and 29).

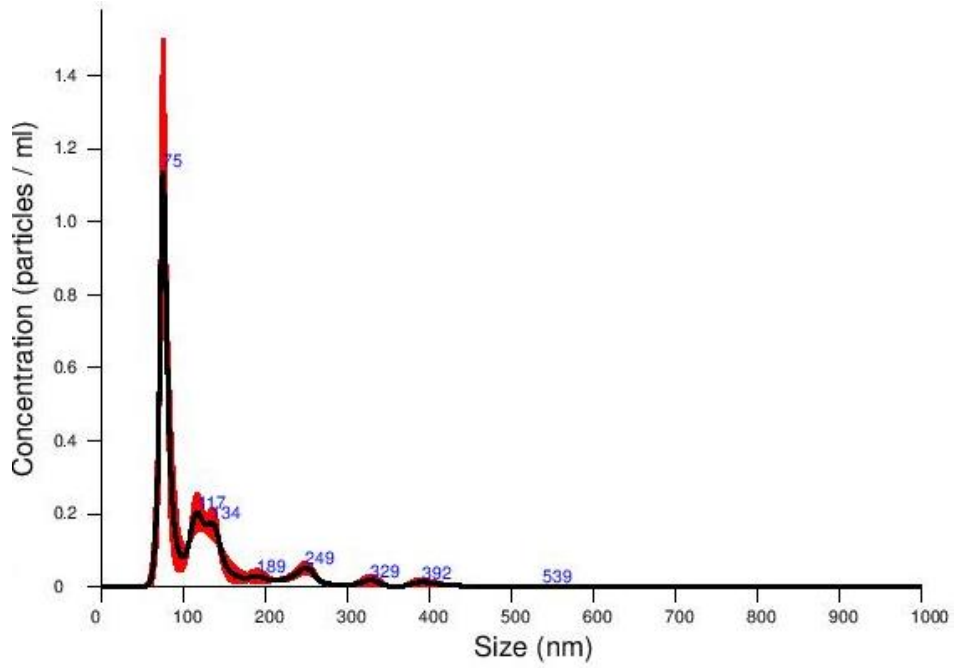

Figure 28 Representative graphs of NanoSight™ particle tracking analysis of concave cube gold nanoparticles.

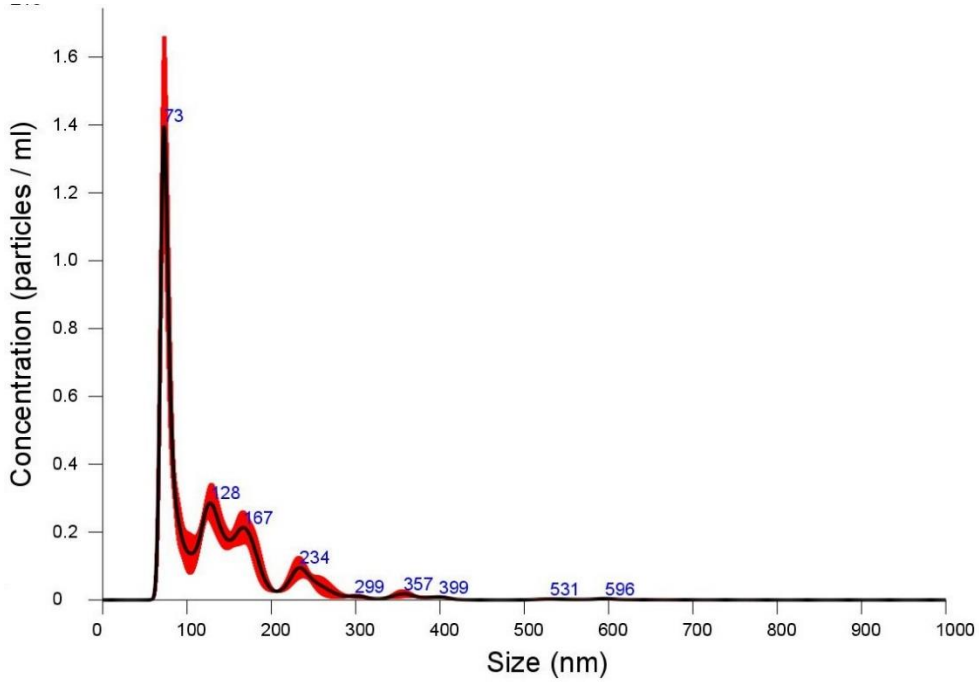

Figure 29 Representative graphs of NanoSight™ particle tracking analysis of Spherical gold nanoparticles.

Chapter 3

Development of Nanoparticles as a contrast agent in MRI

3.1 Aim

A powerful non-invasive medical imaging technique, magnetic resonance imaging requires novel contrast agents for the sensitivity improvement and having higher efficiency than currently used gadolinium chelates, e.g. DTPA:Gd for clinical diagnosis. This objective was achieved using the strategy of serving gold nanoparticles as specific carriers for gadolinium chelates [33]. Herein, a nanoconjugate CA is synthesized by incorporating concave cube gold nanoparticles with Gd(III) complex and then characterization is represented. Taking advantage of good stability, high cellular uptake and remarkable r_1 has been obtained by these conjugates in cellular MR imaging. This behavior was predicted to be affected experimentally through changes in the water diffusion in close proximity to the surface of hydrophilic nanoparticles; leading to a novel design parameter, namely shape engineering, for Gd(III) nanoconjugate CAs with significant r_1. These Gd(III)-functionalized concave cube gold nanoparticles have been promising contrast agents used for magnetic resonance imaging; due to their curved anisotropic shape. Here, the contribution of the concave cube gold nanoparticle shape to the relaxivity of surface bonding Gd(III)-complex has been explicitly examined.

3.2 Instruments and Methods

The longitudinal water proton relaxation rate was measured on a Stelar Spinmaster spectrometer (Stelar, Mede, Italy) operating at 20 MHz, by means of the standard inversion-recovery technique (16 incremented relaxation delay, 2 scans). A typical 90° pulse width was 3.5 us, and the reproducibility of the T_1 data was ±0.5%. The $1/T_1$ nuclear magnetic relaxation dispersion profiles of water protons were measured over a continuum of magnetic field strength from 0.000 24 to 0.5 T (corresponding to 0.01-20

MHz proton Larmor frequency) on the fast field-cycling Stelar Spinmaster FFC 2000 relaxometer equipped with a silver magnet. The relaxometer operates under complete computer control with an absolute uncertainty in the $1/T_1$ values of ±1%. The typical field sequences used were the NP sequence between 40 and 8 MHz and PP sequence between 8 and 0.01 MHz. The observation field was set at 14.5 MHz. Sixteen incremented relaxation delay and two scans were used for the T_1 determination at each field stength.

3.2.1 ^{17}O NMR Measurements

Variable temperature ^{17}O-NMR measurements were registered at 14.09T (600 MHz for ^{1}H) on a BRUKER Avance 600 spectrometer, equipped with a 5mm probe and using a capillary containing D_2O as external lock. Experimental settings were: spectral width 9000 Hz, 90° pulse 14 μs, acquisition time 10 ms, 1024 scans, without sample spinning.

Aqueous solutions containing 2.6% of the ^{17}O isotope were used. The observed transverse relaxation rate (r_2^{obs}) were calculated from the signal width at half-height ($\Delta\nu_{1/2}$):

$$r_2^{obs} = \pi.(\Delta\nu_{1/2}) \quad (8)$$

Paramagnetic contributions to the observed transversal relaxation rate (r_{2p}) were calculated by subtracting from r_2^{obs} the diamagnetic contribution measured at each temperature value on pure water enriched with 2.6% ^{17}O isotope.

3.2.2 Cytotoxicity assays

The cytotoxic effect of the gold nanoparticles was evaluated by using MTT test. HeLa cells were seeded into 96-well tissue culture plate (10^4 cells for plate) 24h before the experiment.

Then, they were incubated with fresh EMEM (Eagle's Minimum Essential Medium) medium supplemented with 10% heat-inactivated fetal bovine serum (FBS), 2 mM glutamine, 100 U/ml penicillin and 100 µg/ml streptomycin; in presence of the nanoparticles in a humidified 5% CO_2 incubator at 37 °C. Incubation time of 3 h was tested for all preparations.

After the incubation time, medium was removed, cells washed and re-incubated in presence of fresh EMEM medium supplemented with 0.5mg/mL MTT for 4h in a humidified 5% CO_2 incubator at 37 °C. The MTT-medium is prepared from 5 mg/1cc MTT in phosphate-buffered saline which is filtered and kept in the dark at 4 °C.

After that, MTT solution was removed and plates were filled with DMSO (0.1 mL for plate) for 30 min at room temperature, under gentle agitation, for allowing solubilization of formazan crystals. All cell media and supplements were purchased from Lonza Sales AG-EuroClone SpA, Milano (IT).

The absorbance of the resulting colored solutions was quantified using a 96-multiwell iMark Bio-Rad microplate Reader (λ= 570nm). The percentage of viable cells was calculated on the basis of control blank cells by using the following formula:

$$\text{Viable cells } \% = (Abs_T/Abs_{cnt}) \times 100 \quad (9)$$

Where Abs_T is the mean absorbance of treated cells and Abs_{cnt} is the mean absorbance of control untreated cells (after subtraction of absorption of empty plates as background). Cells experiments were repeated in triplicate and data reported as mean ± standard deviation. Blank was repeated 10 times.

3.3 Result

3.3.1 Determination of water exchange rate

One of the important factor to know the characteristic of designed contrast agent is the water exchange rate k_{ex}. The residence life time of protons τ_m, plays a dual role in determining proton relaxivity: It modulates the efficiency of chemical exchange from the inner sphere of the metal to the balk, and it also contributes to the overall correlation time, τ_c, that governs the dipole-dipole interaction between the electron and nuclear spin. The exchange of coordinated water protons can occur in two ways, i.e. independently of the exchange of the entire water molecule on which it resides, or via the exchange of the water molecule itself.

Measuring the ^{17}O transverse relaxation rate of variable temperature, would directly determine the water exchange rate for Gd(lll) complex. Enhancement of relaxation rate, $1/T_{2r,}$ for the paramagnetic transverse ^{17}O, is associated with the water residence time, as well as the bound water relaxation rate, $1/T_{2m}$. For a paramagnetic transverse ^{17}O, the typical plot relaxation rate enhancement versus the inverse temperature, represents the increase in slow transverse relaxation rates by increasing the temperature. So, the exchange rate, K_{ex}, determines $1/T_{2r}$ in the current slow kinetic region. Within the fast exchange rates region at high temperatures, the reduced transverse relaxation rates reduce with temperature which are determined the transverse rate value for the coordinated water oxygen, $1/T_{2m}$ [74].

^{17}O relaxation and chemical shift are usually conducted at a magnetic field intensity of 5T or above and for that reason the modified SBM equations could be assumed valid [75].

The inner-sphere water exchange rate of complex 6 was elicited by the variable temperature ^{17}O NMR study (Fig. 30) and the value of τ_m was found 770 nanosecond by fitting the graph.

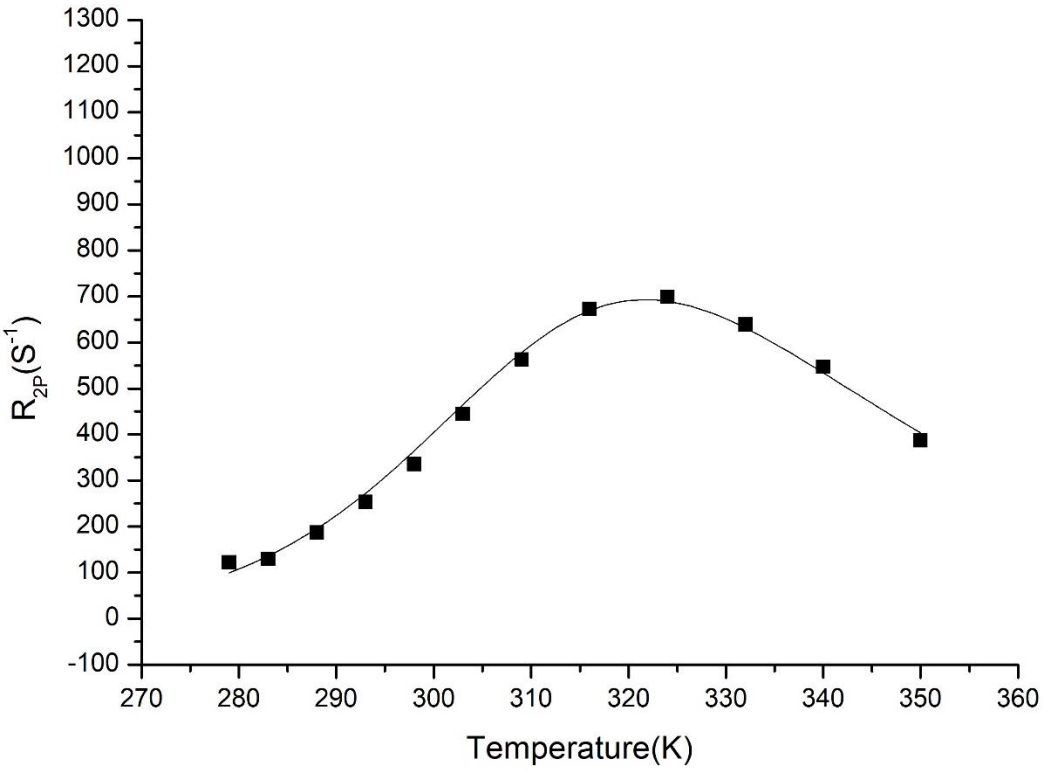

Figure 30 ^{17}O NMR measurement of the Gd complex 6.

3.3.2 NMRD Profiles of free Gadolinium complex

One optimization approach for MRI contrast agents is to accompany the relaxivity, as the observed relaxation enhancement, to dynamical and structural parameters, such as correlation times and distances. The “simple” SBM theory comprises several parameters entering the equation to have an influence on r_i . The independent measurement gives some information about these parameters, e.g. the number of inner-sphere water molecules, or τ_m obtained from ^{17}O measurement. As a method of obtaining information, the relaxivity can be measured as a function of an available physical variable, including temperature or applied magnetic field, B_0. Nuclear magnetic relaxation dispersion (NMRD) is the nuclear spin relaxation measurement as a function of the applied static

magnetic field, proportionating to the Larmor frequency, n_1. The mechanism of relaxation can also be determined through r_i measurement over an extended range of magnetic fields from 0.01-70 MHz. Normally, a logarithmic plot has been observed; due to the field variation over five orders of magnitude. The magnetic field is then generally separated into two regions: (i) low field from the 0.01-20MHz; and (ii) high field from 20 to 70 MHz. Because of the low signal-to-noise ratio of NMR signals in the low field region, either the rapid change of the magnetic field or mechanical shuttling of the sample between different magnetic fields leads to the fast field cycling. The signal detection in both systems enables automatical relaxation measurement over a wide range of magnetic fields with no need for retuning the probes. Generally, to obtain the longitudinal relaxation rate, NP/PP sequence is used. The low-field instruments have low-resolution relaxation measurements; so that do not to differentiate between ^{1}H spin resonances associated with different chemical shifts. The detected NMR signal of Gd(III) complexes in an aqueous solution is >99% due to the water protons, hence lacking spectral resolution would not be a problem, and the relaxation is measured with respect to water proton [76]. The spectra of relaxation measurement versus magnetic field, were then normalized to the concentration of Gd(III) complex to analyze resulting relaxivity respect to the fixed parameter for τ_m and q values. In addition, to quantify gadolinium loading, inductively coupled plasma mass spectrometry (ICP-MS) was used to determine the concentration of Gd(III). PEG_Gd@CCGNPs contained 5180 Gd(III) complexes per nano concave cube.

NMRD profile for free complex 6 was acquired (Fig. 31) and fitted to the relevant equations obtained by SBM theory [75]. An excellent fitting between the experimental and calculated values for the profiles at 298K and 310K was achieved. Table 2 report the structural and dynamic. These values were studies in comparison with the parameters obtained from the NMRD profiles for nanoparticles.

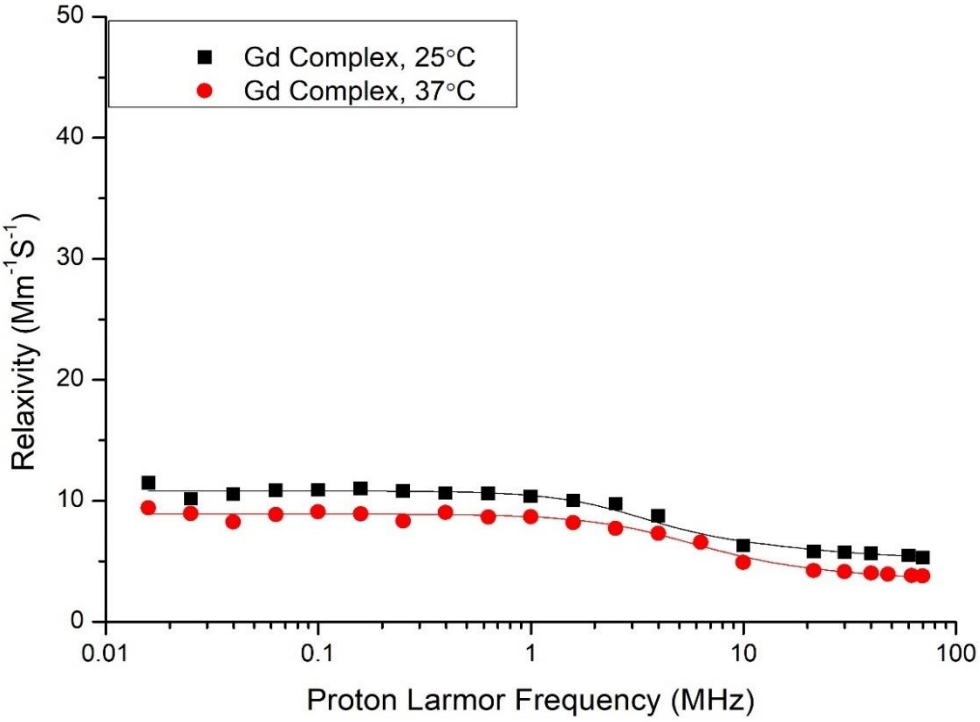

Figure 31 NMRD profile of Gadolinium complex 6 at 25˚C and 37˚C.

	Complex 6, 298K	Complex 6, 310K
S	3.5	3.5
Δ^2 (S^{-2})	$1e^{19}$	$1e^{19}$
tv (ps)	37	31
tr (ps)	126	57
tm (ns)	770	690
r (Å)	3.1	3.1
n	1	1
a (Å)	3.8	3.8
D (cm^2S^{-1})	$2.24e^{-5}$	$2.24e^{-5}$
acc	0	0
n1	0	0
rsf (Å)	3.5	3.5
trsf (ps)	154	140

Table 2 NMRD best fit parameters Gd complex 6 at 298K and 310K.

3.3.3 NMRD Analysis of PEG_Gd@CCGNPs and PEG-Gd@SPhGNPs

The high relaxivities attributed to the CCGNPs have been verified by their irregular shape and this fact was evaluated by synthesizing the PEG_Gd@ spheres of 46 nm using the same Gd(III) complex and PEG. The NMRD profile of these two different shapes of gold nanoparticles was studied (Fig.32) and extracted parameters was compared (Table 3).

First we tried to fit the NMRD graphs without any second sphere contribution, but the NMRD profile related to CCGNPs could not be fitted. Once again, the analysis was constrained to require q = 1, the parameter relevant to second sphere contribution was leave free. For the PEG_Gd@CCGNPs, the NMRD profile represents a maximum relaxivity peak at 34 $mM^{-1}s^{-1}$ at 25 ^{o}C, centered at approximately 25 MHz. The significant contributions were included from water molecules in the second coordination sphere. Accordingly, the data fitting is performed successfully with six second-sphere water molecules at a distance of 3.5 Å for Gd(III)-proton. In most Gd(III) complexes, the contribution of r_1 in the second-sphere water molecules is <10% of total r_1, being also unusual in large contribution required for this interpretation. The covariance value between q_{ss} and the distance of Gd(III)-proton cause even larger values of q_{ss} for achievable for larger proton distances.

Spherical particles generally exhibit similar behavior in relation to the temperature, although representing a remarkably lower r_1. The NMRD profile has been fitted at q = 1 for the spherical system of nanoparticles, most of r_1 at this point can be ascribed to the inner-sphere relaxation. less optimal reorientation times would be due to increased local mobility as determined by the temperature-dependent difference in r_1.

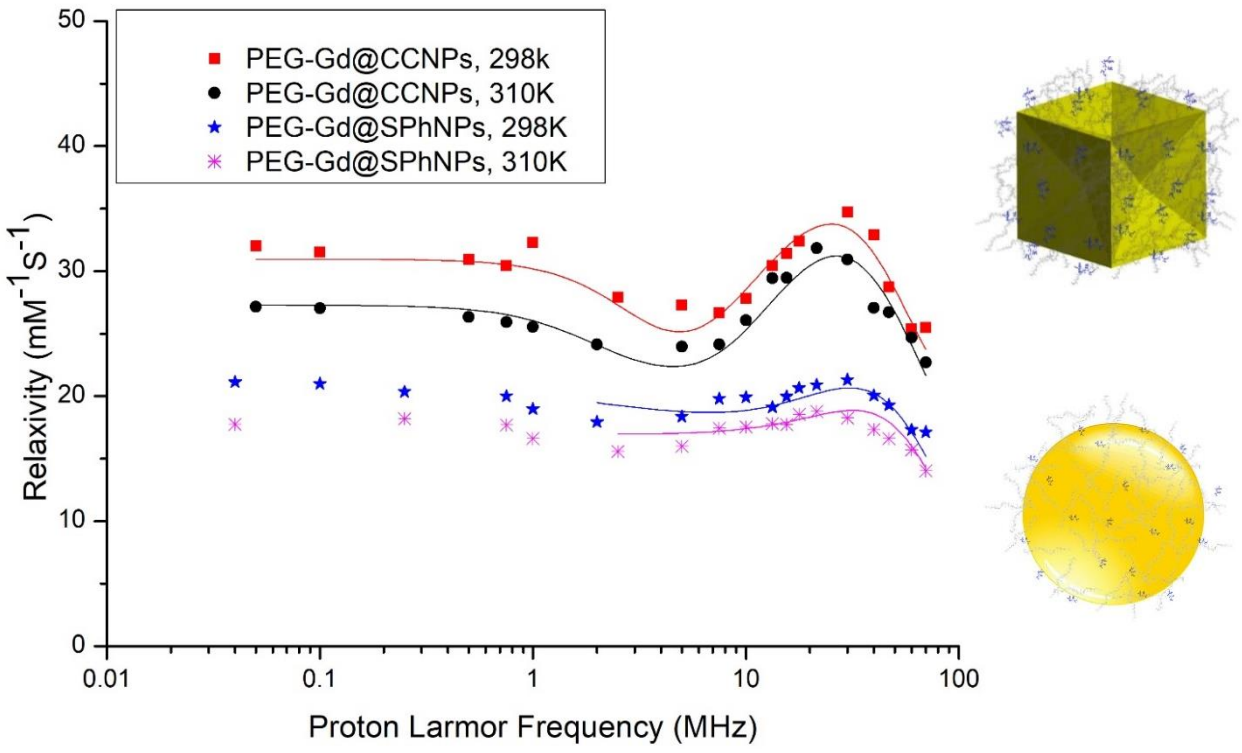

Figure 32 NMRD profile of concave cube and spherical gold nanoparticles at 25 °C and 37°C.

	CCGNPs,298K	CCGNPs,310K	SPhGNPs,298K	SPhGNPs,310K
S	3.5	3.5	3.5	3.5
Δ^2 (S^{-2})	1.8e19	1.6e19	1e19	1e19
tv (ps)	40.6	36	6.8	4.6
tr (ns)	15	6.65	7.8	7
tm (ns)	760	540	710	670
r (Å)	3.1	3.1	3.1	3.1
n	1	1	1	1
a (Å)	3.8	3.8	3.8	3.8
D (cm^2 S^{-1})	2.24e-5	2.24e-5	2.24e-5	2.24e-5
acc	0	0	0	0
n1	6	6	0	0
rsf (Å)	3.5	3.5	3.5	3.5
trsf (ps)	140	59.8	60	54

Table 3 NMRD best fit parameters for PEG-Gd@CCGNPs and PEG-Gd@SPhNPs at 25˚C and 37˚C

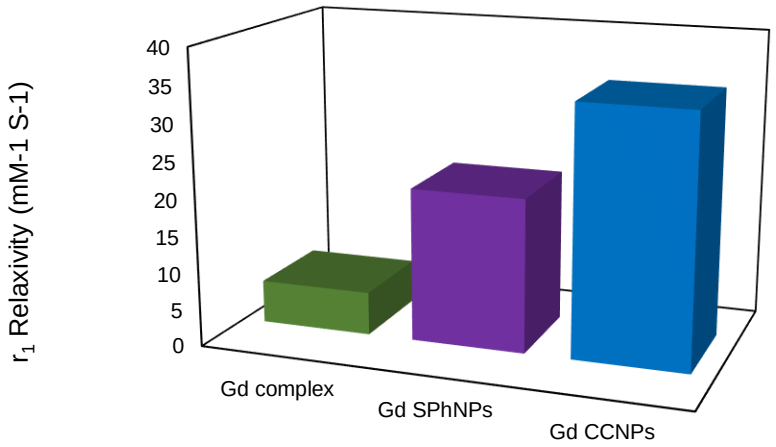

Figure 33 Molar relaxivity of Gd complex, PEG-Gd@SPhNPs and PEG-Gd@CCGNPs.

3.3.4 Cytotoxicity assays of nanoparticles

Cell toxicity of gold nanoparticles has been tested by applying MTT assay and by using HeLa cells. In the experiment, 3 hours of incubation time has been tested for all preparation. In particular, cubic and spherical gold nanoparticles have been compared, with or without the addition of biotin targeting moiety. Nanoparticles have been tested in a 0.02-1.6 uM Gd-range.

As it is reported in Fig.34, for all tested preparation and concentration, the cell viability is generally higher than 60%.

At low concentration, no significant difference among the different preparation can be reported. For the higher tested concentrations (*i.e* 0.5 and 1 uM), a slight higher viability is generally reported for cubic gold nanoparticles in comparison to spherical ones (72-80% *vs*. 60%).

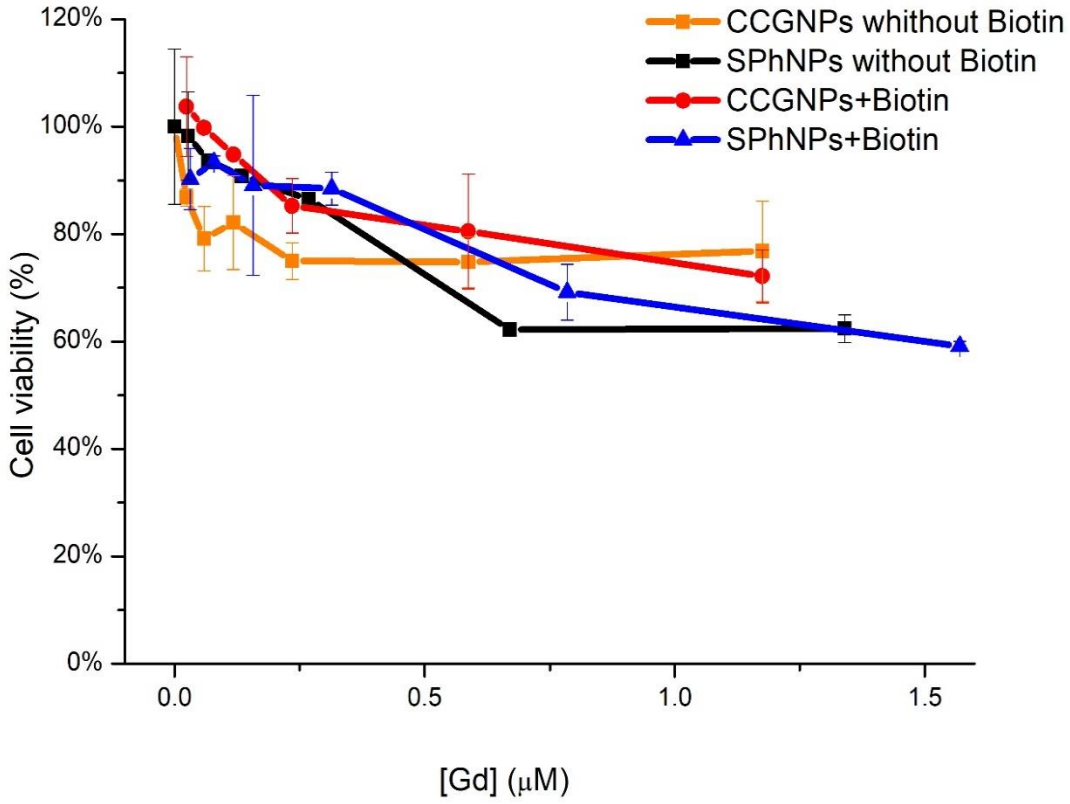

Figure 34 MTT assay results for short incubation time (3h).

3.4 Discussion

Herein, the magnetic properties have been evaluated for concave gold nanoparticles synthesized through thermal decomposition technique and functionalized by Gd complex. By precise study of key factor which contribute to relaxivity, it was found that beside coordinated water molecular, there is important contribution of water protons placed in the second sphere.

3.4.1 Relaxometric Characterization of the Gd Complexes

The paramagnetic effect has been propagated from the paramagnetic center towards the bulk solution in the inner-sphere mechanism. This has been performed on the basis of the chemical exchange between water molecules in the first coordination sphere of the Gd ion and in the bulk. The inner-sphere contribution has been described as the

molecular water exchange between two sites by Salomon-Bloembergen theory. Characterization of MRI contrast agents has been typically conducted by determining the r_{1p} value for T_1 proton relaxivity. Based on the SBM theory, the relaxivity r_{1p}^{IS} depends on several parameters, such as the number of inner-sphere water molecules , the longitudinal relaxation time of the water protons in the inner coordination sphere (T_{1M}), the residence time of the inner-sphere water molecule(s), and the tumbling rate of the paramagnetic complex in solution (Fig. 35). The relaxivity has been largely determined via τ_m and τ_r at clinical field strengths (1.5 – 3 T), which are obtained through fitting variable temperature ^{17}O NMR and ^{1}H nuclear magnetic relaxation dispersion data, respectively [77]. The Gd complex with low molecular weight has had rapid water exchange kinetics and its relaxivity is controlled by the inner-sphere contribution (r_{1p}^{IS}). The macromolecular contrast agent exhibits the NMRD profile with a typical high-frequency peak mainly due to the increased rotational correlation times in comparison with low-molecular weight Gd(III) chelates. The tumbling rate of Gd chelates in lipid-based contrast agents as macromolecular contrast agents has been strongly decreased. Liposomes and nanoparticles have also demonstrated the NMRD profiles with typical high-frequency peaks. Accordingly, these contrast agents have the greatest ionic relaxivity at clinical field strengths [10].

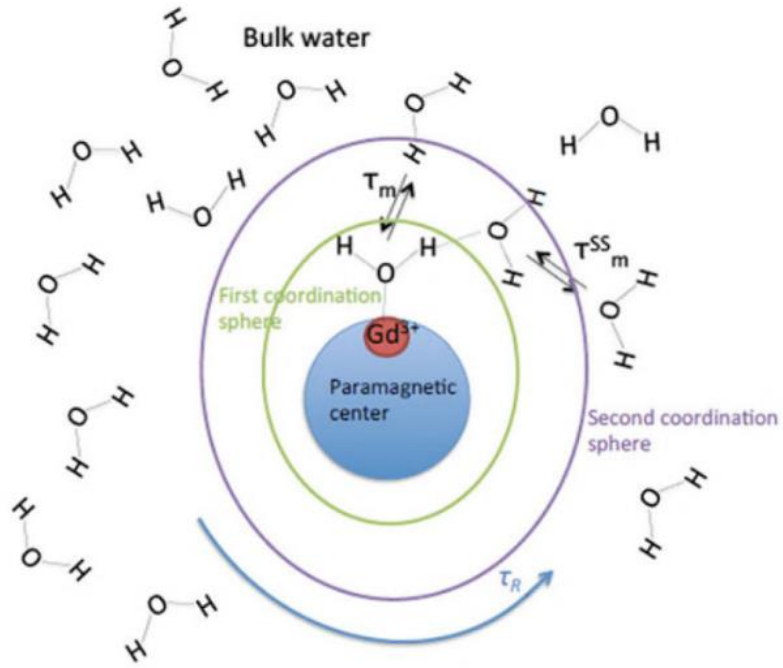

Figure 35 Schematization of a paramagnetic complex with one innersphere molecule, one second-sphere molecule and several outersphere water molecules (bulk water molecules) [78].

Freed has explained the outer-sphere relaxation with respect to the dipolar interaction between the Gd ion and diffusing water molecules proximal to Gd ion. This mechanism is governed only with the relative motion of two entities as well as their closest approach distance. The interaction of water protons which have not direct coordinated bond with the paramagnetic centers, but they are connect to the coordinated protons are expressed by the second-sphere mechanism. The protons constitutes the second coordination sphere could interact with inner sphere protons through the hydrogen bonding [78].

The molecular water lifetime plays a major role in r_1 contributions from both second- and outer-sphere relaxivity in these coordinations. The second-sphere effects of Gd(III) contrast agents bound with proteins or NPs having large r_1 have been identified by molecular confinement as well as the hydrophilic microenvironment [79]. The unusual high r_1 has been due to the large contribution of second-sphere relaxivity with respect to elongated residence times of water molecules present in the second coordination sphere.

The PEG-Gd@spheres and PEG-Gd@CCGNPs are different only in shapes, while spherical conjugates have had no second-sphere enhancement. These results represent the formation of a unique and hydrophilic environment through restricting Gd(III) complex in negative curvature regions between the nano concave cube leading to the promotion of second-sphere effects. Very few mechanical investigations have represented that nanoconjugate CAs do not often exhibit high r_1 relaxivities even in the proper chemical environment of Gd(III). Particularly CAs with protein or hydrophilic polymer extended surfaces, have had slower water diffusion within the chemical environment adjacent to the lanthanide center, namely the second-sphere for the Gd(III) complexes. This environment is sterically crowded by hydrogen bonding mainly associated with slowing down the diffusion of transient water molecules adjacent to Gd(III) [15]. This resulting hydrogen-bonding-rich environment represents increasing longer contact of each metal center with second-sphere water molecules. Walker and colleagues demonstrate that the chemical properties of non-spherical nanoparticles bound to organic molecules have been dependent upon the shape and local curvature of the particles. This phenomenon has been most pronounced for the nanoscale material; due to the correspondence of the radius of curvatures on the support and the common self-assembly (as in self-assembled monolayers, SAMs) thickness (1–2 nm) (Fig 36); as well as the proximity of charged groups with on-particle SAMs. This approach has conceptually advanced not only considering nanoscale self-assembly, but also controlling molecular environments by the shape through SAMs and, eventually, surface chemistries. Correspondingly, the same molecule with different location of underlying curvature can represent different chemical properties [80].

The surface curvature makes the functional groups, e.g. PEG and DNA strands to get closer together leading to intensifying interstrand repulsion. The variation of particle shape can influence nanoconjugate CA surface dynamics and improve the r_1 value through enhancing second-sphere contributions to the CA performance [15]. The results of NMRD analysis revealed that the surface curvature and shape of nanoparticles can affect the formation of conjugated PEGs on the surface of particles and might significantly sequestrate water molecules proximal to the Gd(III) complexes.

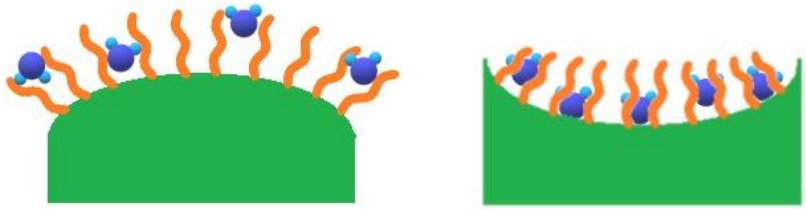

Figure 36 Nano-objects with varying curvatures.

3.5 Conclusion

The present study has confirmed this argument that irregularly shaped nanoparticles are significantly able to influence the chemical reactivity of surface ligands; due to the surface curvature. To achieve high relaxivity CA, a Gd(III)_PEG gold nanoconjugate platform was associated with concave cube irregular shape to obtain PEG_Gd@CCGNPS used for magnetic resonance imaging.

Chapter 4

Development of nanoparticles as a SERS probe

4.1 Aim:

The present study has investigated same concave cube gold nanoparticles of first project to assess their morphological aspects and potential application for highly efficient SERS substrates. In the single-particle surface-enhanced Raman spectroscopy (spSERS), the use of tunable plasmonic nanoparticles, having tipped surface structures, as being substrates revealed a highly feasible and promising approach to optimize SERS-based imaging and sensing applications [54]. Romo-Herrera et al. show that the highest increment of the near-field is located at the eight sharp tips and, interestingly, a medium nearfield increment is also activated over the volume next to the concave surface. The concave cubic morphology has shown a remarkable plasmonic response, representing high sensitivity to the concavity degree [51]. The SERS nanoprobe applications in biological molecules and cells investigations have provided vital information that was not available before their advent. Plasmonic nanoparticles are capable of enhancing endogenous Raman spectra both for biological organelles, structures, and molecules in their immediate vicinity, as well as for reporter molecules that are physisorbed or embedded in their coating structure with the purpose of constructing optical probes to be used for identification of interested biomarkers; due to their detectable SERS spectra [16].

4.2 Instruments and Methods:

Raman spectra were acquired using an InVia Reflex confocal Raman Microscope (Renishaw plc, Wotton-under-Edge, UK), equipped with a He-Ne laser light source, at a working wavelength of 632.8 nm. The Raman spectrophotometer is calibrated daily using the 520.7 cm^{-1} band of a silicon wafer as a reference.

SERS measurements carried out on solutions are carried out with 633 nm wavelength lasers, directly on 250µL of 5x concentrated colloid placed in an eppendorf cap, with 5x

objective, grating of 1200 l / mm and focus depth -200 μm. The spectrophotometer set-up involves centering at 1300 cm^{-1} and recording 10 accumulations of 10 seconds each. Once the spectrum has been recorded, an absorption correction is performed due to the optical glass itself using baseline correction, based on a polynomial of order 11 with tolerance 1.5.

For the measurements on the surfaces used in the SPRi experiment, instead, a map of the colloid drop is recorded according to the following set-up: 633 nm laser at 10% of power, centering at 1350 cm-1, 100x objective, grating 1200 l / mm, 2secx1acc.

Once the spectra are recorded on the drop, the Raman peak of interest is isolated and an image of the relative intensity distribution of the signal is obtained. Raman spectra are represented as the average of 30 measurements chosen randomly from the data set.

4.2.1 Culturing cells for Raman experiment

For this experiment we have used a murine breast cancer cell line stably transfected with human HER2 (named D2F2/E2), received by Prof. Wei Zen Wei (Wayne University). As a negative control of cell line that doesn't express human HER2 receptor, we have used untrasfected cell line (D2F2). A total of 0.8×10^6 D2F2 (HER2-negative) and D2F2/E2 (HER2 positive) cells was seeded on cover glass slides precoated with polysin in a 12-well plate.

After 6h, cells were washed three times with PBS. Then, cells were fixed 25 min with 2% paraformaldehyde and washed three times with PBS.

The D2F2/E2 cells were incubated overnight with a suspension of nanoparticles which are diluted 1 to 4 in PBS at room temperature. The next day, the nanoparticles were washed twice with PBS. Raman measurements were performed to observe the localization of the nanoparticles conjugated with the Raman reporter (MGITC) and the antibody.

4.2.2 Raman imaging

The Raman images of the cells were acquired using an He-Ne laser operating at 632.8 nm. The light was then focused on the cells by an immersion objective (60×/1.0 NA, Olimpus). The excitation power measured at the level of the sample was 7.5 mW and each spectrum was obtained with an acquisition time of 2 sec. Each cell was scanned acquiring a spectra every 1.8 um.

In order to detect the presence of the nanoparticles we used a Direct Classical Least Squares analysis (DCLS) using as reference spectrum the one obtained using the same set up on a suspension of nanoparticles. The presence of the nanoparticles on cell surface is shown in red by the software. Spectra acquisition and data manipulations were performed using Wire 5.2 from Renishaw (Wotton-under-Edge, UK)

4.3 Result

4.3.1 Assessment of Raman activity of concave cube gold nanoparticles

UV-Vis spectrum of nanoparticles (Fig. 37-1) reveals the maximum of the adsorption peak is exactly at 633 nm which provide the effective enhancement of the SERS signals of the MGITC observed using a red laser (633 nm). Over a broad spectral, the LSPR of CCGNPs was fine-tuned respect to the wavelength of excitation laser. This coordination is achievable through tight control over particle sizes which makes possible quantitatively evaluate the performance of individual nanoparticles as SERS substrates. In this wavelength the resonance of the laser with the plasmonic absorption peak of the nanoparticles were matched. In this condition the particles are able to produce the most intense SERS spectra and they be effectively used as a SERS tag. Figure 37-2 shows SERS spectra of concave cube gold nanoparticles obtained with 633 laser line. This

spectra verify SERS activity of the particles. These nanoparticles were already conjugated with the isothiocyanate green malachite. This dye has a simple and very intense characteristic SERS spectrum, which allows it to be uniquely identified even within a complex biofluid. SERS spectra of CCGNPs is obtained from a suspension of nanoparticles coated with a mixture of HS-PEG and Malachite green isothiocyanate, which confirms the effective presence of the Raman reporter and the Enhancement factor of about 105, as expected. The SERS spectra of the labeled nanoparticle were sufficiently intense to be detected. The spectrum is dominated by three main peaks: one very evident at around 1610 cm-1, relative to breathing vibrations of the aromatic rings which are also the cause of the peak at 1370 cm-1. The peak at 1172 cm-1 is instead related to vibrations of the aromatic C-H bonds.

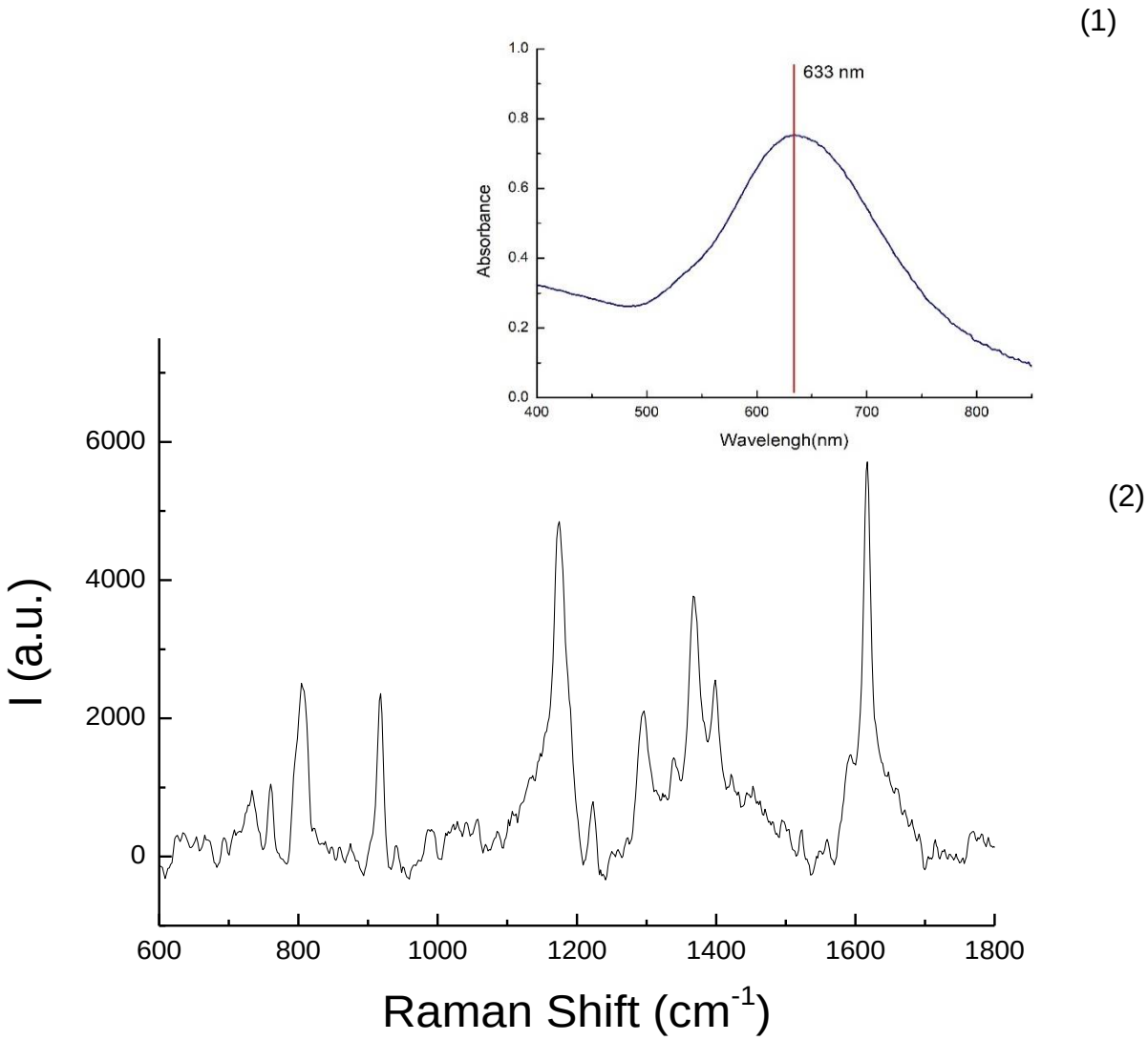

Figure 37 (1) UV-Vis spectra and (2) Raman spectra of SERS concave cube gold nanoparticles.

4.3.2 *In Vitro* experiment

After washing the SERS nanoparticles which have already incubated by D2F2/E2 cells, the Raman measurement was conducted. The results reveal the presence of nanoparticles on the cells expressing HER2 (D2F2/E2) (Fig. 38). An analogous experiment had been carried out on equivalent cells but not expressing human HER2 on the membrane (D2F2). In this case no Raman signal was observed in the sample and the nanoparticles are almost absent.

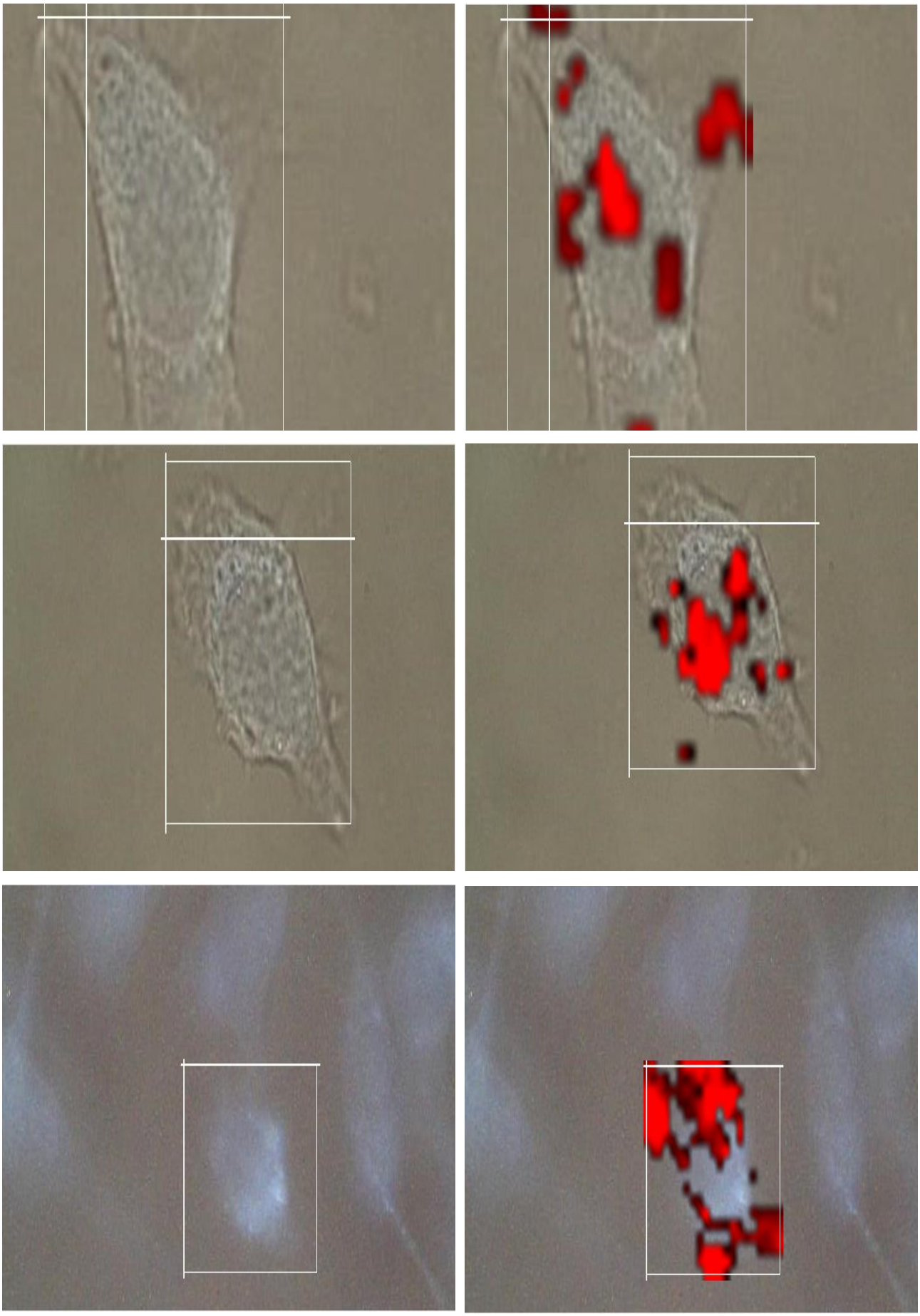

Figure 38 Internalization of CCGNPs in D2F2/E2 cells

4.4 Discussion

The SERS signal interpretations can be mainly expressed based on (1) the shape- and size-dependent plasmonic responses of individual nanoparticles; and (2) the distribution of morphology within each set of colloids [51]. Large EFs were obtained by certain structures having “hot spots” [43]. For the concave nanocubes, the highest field enhancements were observed in the vicinities of tips, and significantly enhanced electric fields were also at the particle edges. They also represent larger field enhancements with higher degrees of indentation. Plasmonic field enhancements of Au nanoparticles with nanoengineered surface tips were sufficiently high for spSERS without involving the strongly coupling plasmons confined in nanoscale interparticle or intraparticle junctions [54]. As a result, Au concave nanocubes demonstrate greatly improved SERS performance as compared with same sized Au nanocubes and nanospheres; mainly because of intense local-field enhancements at sharp tips. SERS enhancements can also be efficiently determined by the particle geometries, as well as the excitation laser and LSPRs coupling. Since concave nanocubes have size-dependent LSPRs, it can be fine-tuned considering the excitation laser wavelength, as well, the spSERS enhancements can be quantified as a function of particle size [54]. Respect to the specific fingerprint SERS spectra of probe, unambiguous identification was provide for detection and localization of target in the biologically significant near infrared window [16].

4.5 Conclusion

We have developed an AuNP-based SERS prob to obtain strong signal thanks to sharped tips structure of nanoparticles. The CCGNPs provide the pretty stable, greatly quantitative and controllable SERS signals. Furthermore, the main component of CCGNPs structure is gold which is known as a not cytotoxic substance [23] and could be easily functionalized

with biomolecules such as thiolated PEG and antibodies for biosensing and imaging applications. These exotic nanoparticles present reliable SERS active conjugation which can be applied in *in vitro* bioassay, *in situ* probe tracking in cells and *in vivo/ex vivo* Raman imaging.

Expected achievement

Given that one can not obtain a full perspective on all the aspects of a structure using only one imaging modality, it's always better to have multiple imaging modalities to have a clear image of the structure [81]. Since there are both shortcomings and advantages in each modality, the idea of integrating two modal molecular imaging into a single platform could be very beneficial [4]. Magnetic resonance and optical imaging can be used complementary techniques. The first one has a very high resolution and deep penetration capability but low sensitivity. Nanoparticles combining SERS imaging and magnetic resonance imaging are getting trendy in the research since they can combine the high brightness of signals in SERS phenomenon with high spatial resolution in MRI application leading to low dosage application. Therefor, a useful contrast agent for tumor identification and ablation could be multimodalCAs [79,80].

In this work we present a plasmonic nanosystem as a MRI and SERS multimodal contrast agent that they can mixed physically, or this would consider of accomplisher prospective of this project that puting all reporter in one agent.

Bibliography

1 Perfézou, M. *et al.* (2012) Cancer detection using nanoparticle-based sensors. *Chem. Soc. Rev.* 41, 2606–2622

2 Blasiak, B. *et al.* (2013) Applications of Nanoparticles for MRI Cancer Diagnosis and Therapy. *J. Nanomater.* 2013, 1–12

3 Zhou, B. *et al.* (2016) PEGylated polyethylenimine-entrapped gold nanoparticles loaded with gadolinium for dual-mode CT/MR imaging applications. *Nanomedicine* 11, 1639–1652

4 Song, Y. *et al.* (2009) Multimodal Gadolinium-Enriched DNA Gold Nanoparticle Conjugates for Cellular Imaging. *Angew Chem Int Ed Engl.* 48, 9143–9147

5 Bloch, F. (1951) Nuclear induction. *Physica* 17, 272–281

6 CARLYLE BUSHONG, S. and Clarke, G. (2013) *Magnetic Resonance Imaging: Physical and Biological Principles*, Elsevier Health Sciences.

7 Millstone, J.E. *et al.* (2008) DNA-Gold Triangular Nanoprism Conjugates. *Small* 4, 2176–2180

8 Bjørnerud, A. (2008) *The Physics of Magnetic Resonance Imaging*,

9 Wahsner, J. *et al.* (2019) Chemistry of MRI contrast agents: Current challenges and new frontiers. *Chem. Rev.* 119, 957–1057

10 Mulder, W.J.M. *et al.* (2006) Lipid-based nanoparticles for contrast-enhanced MRI and molecular imaging. *NMR Biomed.* 19, 142–164

11 Marangoni, V.S. *et al.* (2017) Enhancing T_1 magnetic resonance imaging contrast with internalized gadolinium(III) in a multilayer nanoparticle. *Proc. Natl. Acad. Sci.* 114, 6960–6965

12 Nicholls, F.J. *et al.* (2016) DNA-gadolinium-gold nanoparticles for in vivo T1 MR imaging of transplanted human neural stem cells. *Biomaterials* 77, 291–306

13 Zhang, L. *et al.* (2016) The evolution of gadolinium based contrast agents: From single-modality to multi-modality. *Nanoscale* 8, 10491–10510

14 Lowe, M.P. (2002) MRI contrast agents: The next generation. *Aust. J. Chem.* 55, 551–556

15 Rotz, M.W. *et al.* (2015) High relaxivity Gd(III)-DNA gold nanostars: Investigation of shape effects on proton relaxation. *ACS Nano* 9, 3385–3396

16 Maclaughlin, C.M. (2014) , Surface-Enhanced Raman Scattering Nanoparticles as Optical Labels for Imaging Cell Surface Proteins.

17 Zhang, J. *et al.* (2010) Concave cubic gold nanocrystals with high-index facets. *J. Am. Chem. Soc.* 132, 14012–14014

18 Fabris, L. (2016) SERS Tags: The Next Promising Tool for Personalized Cancer Detection? *ChemNanoMat* 2, 249–258

19 Gabriel Etchegoin, P. and Le Ru, E. (2008) *Principles of Surface-Enhanced Raman Spectroscopy: And Related Plasmonic Effects*,

20 Kneipp, K. *et al.*, eds. (2006) *Surface-Enhanced Raman Scattering: Physics and Applications*, Springer Science & Business Media.

21 Gandra, N. and Singamaneni, S. (2013) Bilayered raman-intense gold nanostructures with hidden tags (BRIGHTs) for high-resolution bioimaging. *Adv. Mater.* 25, 1022–1027

22 Zhao, B. *et al.* (2014) Gold nanostructures encoded by non-fluorescent small molecules in polyA-mediated nanogaps as universal SERS nanotags for recognizing various bioactive molecules. *Chem. Sci.* 5, 4460–4466

23 Lim, D.K. *et al.* (2011) Highly uniform and reproducible surface-enhanced Raman scattering from DNA-tailorable nanoparticles with 1-nm interior gap. *Nat. Nanotechnol.* 6, 452–460

24 Wang, Y. *et al.* (2013) SERS Tags: Novel optical nanoprobes for bioanalysis. *Chem. Rev.* 113, 1391–1428

25 Qian, X. *et al.* (2008) In vivo tumor targeting and spectroscopic detection with surface-enhanced Raman nanoparticle tags. *Nat. Biotechnol.* 26, 83–90

26 Wilson, A.J. and Willets, K.A. (2013) Surface-enhanced Raman scattering imaging using noble metal nanoparticles. *Wiley Interdiscip. Rev. Nanomedicine Nanobiotechnology* 5, 180–189

27 Alric, C. *et al.* (2008) Gadolinium chelate coated gold nanoparticles as contrast agents for both X-ray computed tomography and magnetic resonance imaging. *J. Am. Chem. Soc.* 130, 5908–5915

28 Wang, S. (2015) PEGylated Gold Nanoprisms for Photothermal Therapy at Low Laser Power Density RSC Advances therapy at low laser power density. *RSC Adv.* 5, 81682–81688

29 Hahn, M.A. *et al.* (2011) Nanoparticles as contrast agents for in-vivo bioimaging: Current status and future perspectives. *Anal. Bioanal. Chem.* 399, 3–27

30 Balakrishnan, S. *et al.* (2017) Applications of gold nanoparticles in cancer. *Biomed. Eng. Concepts, Methodol. Tools, Appl.* 1, 780–808

31 Culver, K.S.B. *et al.* (2016) Shape-Dependent Relaxivity of Nanoparticle-Based T1 Magnetic Resonance Imaging Contrast Agents. *J. Phys. Chem. C* 120, 22103–22109

32 Kim, M. *et al.* (2018) Dealloyed Intra-Nanogap Particles with Highly Robust, Quantifiable Surface-Enhanced Raman Scattering Signals for Biosensing and Bioimaging Applications. *ACS Cent. Sci.* 4, 277–287

33 Debouttière, P.J. *et al.* (2006) Design of gold nanoparticles for magnetic resonance imaging. *Adv. Funct. Mater.* 16, 2330–2339

34 Hartsuiker, L. *et al.* (2011) , Gold nanoparticles for tumour detection and treatment. , in *Optics InfoBase Conference Papers*, 8087, pp. 1–10

35 Hurst, S.J. *et al.* (2006) Maximizing DNA loading on a range of gold nanoparticle sizes. *Anal. Chem.* 78, 8313–8318

36 Daniel, M.C. and Astruc, D. (2004) Gold Nanoparticles: Assembly, Supramolecular Chemistry, Quantum-Size-Related Properties, and Applications Toward Biology, Catalysis, and Nanotechnology. *Chem. Rev.* 104, 293–346

37 Grabar, K.C. *et al.* (1995) Preparation and Characterization of Au Colloid Monolayers. *Anal. Chem.* 67, 735–743

38 Bergen, J.M. *et al.* (2006) Gold Nanoparticles as a Versatile Platform for Optimizing Physicochemical Parameters for Targeted Drug Delivery. *Macromol. Biosci.* 6, 506–516

39 De La Fuente, J.M. *et al.* (2006) Nanoparticle targeting at cells. *Langmuir* 22, 3286–3293

40 Niidome, T. *et al.* (2006) PEG-modified gold nanorods with a stealth character for in vivo applications. *J. Control. Release* 114, 343–347

41 Liu, Z. *et al.* (2007) In vivo biodistribution and highly efficient tumour targeting of carbon nanotubes in mice. *Nat. Nanotechnol.* 2, 47–52

42 Lee, S. *et al.* (2007) Biological imaging of HEK293 cells expressing PLCγ1 using surface-enhanced raman microscopy. *Anal. Chem.* 79, 916–922

43 Rycenga, M. *et al.* (2012) Chemically isolating hot spots on concave nanocubes. *Nano Lett.* 12, 6218–6222

44 Cho, K. *et al.* (2008) Therapeutic nanoparticles for drug delivery in cancer. *Clin. Cancer Res.* 14, 1310–1316

45 Feng, Q. *et al.* (2017) Self-Assembly of Gold Nanoparticles Shows Microenvironment-Mediated Dynamic Switching and Enhanced Brain Tumor Targeting. *Theranostics* 7, 1875–1889

46 Sykes, E.A. *et al.* (2014) Investigating the impact of nanoparticle size on active and passive tumor targeting efficiency. *ACS Nano* 8, 5696–5706

47 Langille, M.R. *et al.* (2012) Defining rules for the shape evolution of gold nanoparticles. *J. Am. Chem. Soc.* 134, 14542–14554

48 Jana, N.R. *et al.* (2001) Seed-Mediated Growth Approach for Shape-Controlled Synthesis of Spheroidal and Rod-like Gold Nanoparticles Using a Surfactant Template. *Adv. Mater.* 13, 1389–1393

49 Schwartz-Duval, A.S. *et al.* (2016) An anisotropic propagation technique for synthesizing hyperbranched polyvillic gold nanoparticles. *Nano Res.* 9, 2889–2903

50 Personick, M.L. and Mirkin, C.A. (2013) Making sense of the mayhem behind shape control in the synthesis of gold nanoparticles. *J. Am. Chem. Soc.* 135, 18238–18247

51 Romo-Herrera, J.M. *et al.* (2016) A study of the depth and size of concave cube Au nanoparticles as highly sensitive SERS probes. *Nanoscale* 8, 7326–7333

52 Bhattarai, S.R. *et al.* (2017) Gold nanotriangles: Scale up and X-ray radiosensitization

effects in mice. *Nanoscale* 9, 5085–5093

53 Wang, Y. *et al.* (2012) Specific functionalization of CTAB stabilized anisotropic gold nanoparticles with polypeptides for folding-mediated self-assembly. *J. Mater. Chem.* 22, 20368–20373

54 Zhang, Q. *et al.* (2014) Gold nanoparticles with tipped surface structures as substrates for single-particle surface-enhanced raman spectroscopy: Concave nanocubes, nanotrisoctahedra, and nanostars. *ACS Appl. Mater. Interfaces* 6, 17255–17267

55 Zhou, H. *et al.* (2018) Dense and Dynamic Polyethylene Glycol Shells Cloak Nanoparticles from Uptake by Liver Endothelial Cells for Long Blood Circulation. *ACS Nano* 12, 10130–10141

56 Bogliotti, N. *et al.* (2011) Optimizing the formation of biocompatible gold nanorods for cancer research: Functionalization, stabilization and purification. *J. Colloid Interface Sci.* 357, 75–81

57 Zhang, G. *et al.* (2009) Influence of anchoring ligands and particle size on the colloidal stability and in vivo biodistribution of polyethylene glycol-coated gold nanoparticles in tumor-xenografted mice. *Biomaterials* 30, 1928–1936

58 Pai, S.S. *et al.* (2011) The conformation of the poly(ethylene glycol) chain in mono-PEGylated Lysozyme and mono-PEGylated human growth hormone. *Bioconjug. Chem.* 22, 2317–2323

59 Manson, J. *et al.* (2011) Polyethylene glycol functionalized gold nanoparticles: The influence of capping density on stability in various media. *Gold Bull.* 44, 99–105

60 Thierry, B. and Griesser, H.J. (2012) Dense PEG layers for efficient immunotargeting of nanoparticles to cancer cells. *J. Mater. Chem.* 22, 8810–8819

61 Danhier, F. *et al.* (2010) To exploit the tumor microenvironment: Passive and active tumor targeting of nanocarriers for anti-cancer drug delivery. *J. Control. Release* 148, 135–146

62 Oyelere, A.K. *et al.* (2007) Peptide-conjugated gold nanorods for nuclear targeting. *Bioconjug. Chem.* 18, 1490–1497

63 Lee, C.M. and Tannock, I.F. (2010) The distribution of the therapeutic monoclonal

antibodies cetuximab and trastuzumab within solid tumors. *BMC Cancer* 10,

64 Yang, W. *et al.* (2009) Targeting cancer cells with biotin-dendrimer conjugates. *Eur. J. Med. Chem.* 44, 862–868

65 Collina, S. (2014) New Perspectives in Cancer Therapy: The Biotin-Antitumor Molecule Conjugates. *Med. Chem. (Los. Angeles).* S,

66 Chuang, S.M. *et al.* (2013) Extensive evaluations of the cytotoxic effects of gold nanoparticles. *Biochim. Biophys. Acta - Gen. Subj.* 1830, 4960–4973

67 Singhal, S. *et al.* (2010) Nanotechnology Applications in Surgical Oncology. *Annu. Rev. Med.* 61, 359–373

68 Giljohann, D.A. *et al.* (2010) Gold nanoparticles for biology and medicine. *Angew. Chemie - Int. Ed.* 49, 3280–3294

69 Nikzad, S. and Hashemi, B. (2014) MTT assay instead of the clonogenic assay in measuring the response of cells to ionizing radiation. *J. Radiobiol.* 1, 3–8

70 Calagua, A. *et al.* (2015) Synthesis and Characterization of Bimetallic Gold-Silver Core-Shell Nanoparticles: A Green Approach. *Adv. Nanoparticles* 04, 116–121

71 Personick, M.L. *et al.* (2011) Shape control of gold nanoparticles by silver underpotential deposition. *Nano Lett.* 11, 3394–3398

72 Zheng, Y. *et al.* (2014) Successive, Seed-Mediated Growth for the Synthesis of Single-Crystal Gold Nanospheres with Uniform Diameters Controlled in the Range of 5-150 nm. *Part. Part. Syst. Charact.* 31, 266–273

73 Goldstein, J. and Yakovitz, H. (1975) *Practical Scanning Electron Microscopy*, Springer US.

74 Krause, W., ed. (2002) *Contrast Agents I: Magnetic Resonance Imaging*,

75 Lauffer, R.B. (1987) Paramagnetic Metal Complexes as Water Proton Relaxation Agents for NMR Imaging: Theory and Design. *Chem. Rev.* 87, 901–927

76 C. Pierre, V. and J. Allen, M., eds. (2018) *Contrast Agents for MRI - Experimental Methods*, Cambridge : Royal Society of Chemistry.

77 Rojas-Quijano, F.A. *et al.* (2012) Synthesis and Characterization of a Hypoxia-Sensitive

MRI Probe. *Chem. - A Eur. J.* 18, 9669–9676

78 Laurent, S. *et al.* (2016) *MRI Contrast Agents From Molecules to Particles*,

79 Nehl, C.L. and Hafner, J.H. Shape-dependent plasmon resonances of gold nanoparticles. , *Journal of Materials Chemistry*, 18. (2008) , 2415–2419

80 Walker, D.A. *et al.* (2013) Geometric curvature controls the chemical patchiness and self-assembly of nanoparticles. *Nat. Nanotechnol.* 8, 676–681

81 Jennings, L.E. and Long, N.J. (2009) 'Two is better than one'—probes for dual-modality molecular imaging. *Chem. Commun.* DOI: 10.1039/b821903f

82 Litti, L. *et al.* (2018) A SERRS/MRI multimodal contrast agent based on naked Au nanoparticles functionalized with a Gd(III) loaded PEG polymer for tumor imaging and localized hyperthermia. *Nanoscale* 10, 1272–1278

Acknowledgements

Firstly, I would like to express my sincere gratitude to my supervisors Dr. *Miriam Colombo* and *Dr. Daniela Delli Castelli* for the continuous support of my Ph.D. study.

A special thank goes to *Prof. Silvio Aime* who provided me an opportunity to join his team, and who gave access to the laboratory and research facilities. Without his precious support it would not be possible to conduct this research.

Besides my advisor, I would like to thank *Prof. Davide Prosperi*. His guidance helped me in all the time of research and writing of this thesis.

I am grateful to Dr. *Carlo Francesco Morasso* for contributing valuable insight and guidance of my thesis project.

I would like to thank my friends for accepting nothing less than excellence from me in MBC.

Finally, I must express my very profound gratitude to my husband, *Farzad*, for providing me with unfailing support and continuous encouragement throughout my years of study and through the process of researching and writing this thesis.